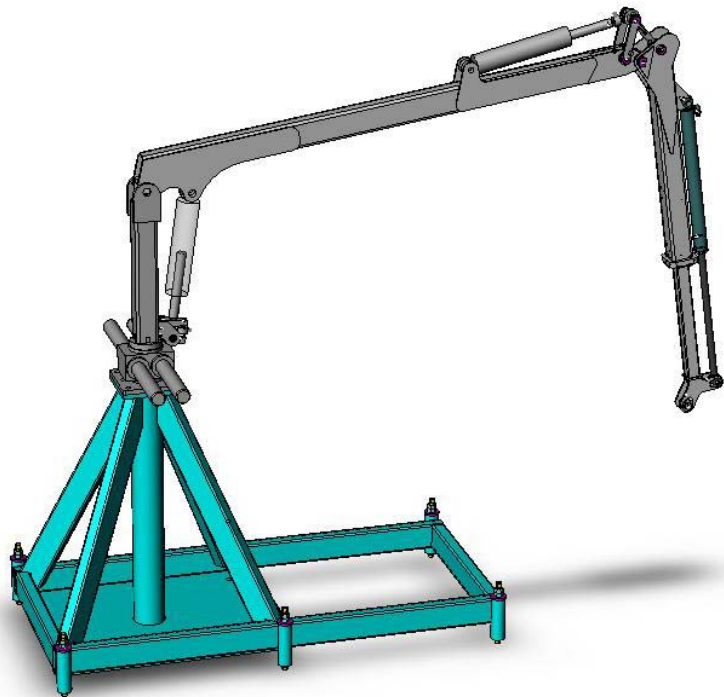


Modelling, simulation and control of a hydraulic crane

Modellierung, Simulation und Steuerung eines hydraulischen Krans
Modellera, simulera och styra av en hydraulisk kran



Submitted for the Degree of *Master of Science* in *Automotive Mechatronics*
at Munich University of Applied Sciences

Växjö, September 2007
Examensarbete nr: TD 002/2008
Författare: Alexander Heinze (780228-P191)

Avdelningen för Maskinteknik

Organisation/ Organization/ Institution VÄXJÖ UNIVERSITET Institutionen för teknik och design School of Technology and Design		Författare/ Author/ Autor Alexander Heinze	
Dokumenttyp/ Type of document/ Dokumententyp MS Word	Handledare/ Supervisor/ Aufsichtsperson Torbjörn Ekevid (Växjö University)	Examinator/ Examiner/ Prüfer Prof. Dr. Peter Wolfsteiner (Munich University of Applied Sciences)	
Titel/ Title/ Titel Modelling, Simulation And Control Of A Hydraulic Crane			
Nyckelord/ Keywords/ Schlüsselwörter crane dynamics, friction maps, evaluation of dynamic cylinder friction, LuGre model, crane-tip control			
Utgivningsår/ Year of issue/ Jahr der Veröffentlichung 2007	Språk/ Language/ Sprache English	Antal sidor/ Number of pages/ Seitenanzahl 137	
Internet		http://www.vxu.se/td	

Abstract

The objective of this thesis is to develop a model that represents the dynamics of a hydraulically operated forestry crane. The model was derived with the traditional Euler-Lagrange formalism and considered the crane mechanics, three double-acting hydraulic cylinders and the valve control unit. On the basis of the derived model we reproduced the entire crane model in *MATLAB* in order to run simulations herewith. This gave us the possibility to do parameter changes for further studies of the crane in motion.

Another major goal within the thesis work was to estimate cylinder friction of the hydraulic actuators. We build up a test rig and used a double-acting cylinder for determining its frictional behaviour. For this, we ran open-loop experiments in order to create velocity-friction maps that represented the static friction force of the cylinder. In this concern, we varied system pressure and cylinder load to study their influence on the friction force. By means of the derived static friction maps we approached the cylinder's dynamic friction behaviour and applied both step and ramp control inputs to examine the spring-damping characteristics of the microspic bristles in the contacting area. The dynamic friction experiments have been exerted in the fashion of the LuGre model. As a result we acquired different nominal friction parameters that we necessarily used to develop adequate friction models.

A third objective of this thesis was to establish a crane-tip control. Instead of a traditional control, providing a direct relationship between joystick input and cylinder extension, the focus was to build up a control for the end-effector's trajectory in a two-dimensional frame. This was achieved by using inverse kinematics in order to determine the required joint angles that corresponded to the desired position of the crane-tip.

The work also contains a CD including all developed *MATLAB* models that have been written within this project.

Summary

Hydraulic cranes are very popular for carrying out hauling operations of forestry machines. In **chapter 1** we will give an overview of such vehicles followed by the problem definition and a description of the tools that have been used during the project work.

A small hydraulic crane was provided by Rottne Industri AB to do experimental work in the laboratory hall of Växjö University. In **chapter 2**, the laboratory crane and its constituent parts are described in detail. This involves the mechanical structure, the connected hydraulic system, sensors and peripheral equipment. Sketches of the crane elements are also presented in this chapter.

The mechanical model will be derived in **chapter 3**, beginning with the definition of rotation matrices followed by a set-up of necessary kinematic chains. Finally the derivation of the Euler-Lagrange equations allows us for examining the dynamical behaviour of the crane.

In **chapter 4** the hydraulic model will be described. It is divided into two major parts, namely the mathematical model of the spool valve and the mathematical model of the hydraulic cylinders. In both cases we will foremost present a static model which will be followed by the dynamic model in order to derive the corresponding equations of motion.

Friction modeling is done in **chapter 5**. At the beginning of this chapter we will describe the main friction phenomenon including the traditional static friction model and the dynamic bristle interpretation in the fashion of the LuGre model. Open-loop experiments at the laboratory crane will be carried out to examine the frictional behaviour of the used hydraulic cylinders. The results provide us the cylinder's nominal friction parameters which, in turn allows us to build up adequate friction models.

The main control principle is described in **chapter 6**. The traditional control task of a hydraulic crane is accomplished via two joysticks that control each cylinder separately. We will present a more convenient method using a sophisticated crane-tip control. In this concern, we will focus on inverse joint determination combined with traditional PID control.

We used MATLAB for all kind of modeling and simulation during the thesis work. The main program files are represented in **chapter 7** but can also be found on the attached CD in the appendix.

Acknowledgements

This thesis work was carried out in the department of technology and design (TD) at Växjö University, Sweden. It was initiated within the research group *Heavy Vehicles* in collaboration with Växjö University and Rottne Industri AB.

The author would like to express his gratitude to all those who confirmed the permission and thus made it possible to complete the thesis work at Växjö University.

Most notably, I would like to convey my thanks to the project supervisor Torbjörn Ekevid at Växjö University for providing advisory support and professional advice of any kind. I also want to thank Matz Lennels at Växjö University for giving me advisable help regarding control principles of Euler-Lagrange systems. Furthermore I am deeply indebted to Anders Hultgren at Kalmar University for his stimulating suggestions and outstanding encouragement from the very beginning of this thesis work, especially for the intense and valuable discussions about cylinder friction on many nights in the laboratory hall. I would also like to thank Rottne Industri AB whose courtesy of the hydraulic crane enabled us to experience the real-crane behaviour along friction experiments that have been directly carried out at the labcrane. Finally I would like to give my special thanks to my professor at Munich University of Applied Sciences for encouraging me working abroad but also for his help and feedback on numerous issues of this thesis work

Alexander Heinze

Växjö, 29th September 2007

Symbols

General notation:

${}_X \vec{r}_y$	Position vector of length y referred to the X -frame
${}_X \vec{r}_{YZ}$	Position vector of distance between part Y and part Z referred to the X -frame
${}_X A_Y$	Rotation matrix from frame Y to frame X
$\vec{r}(x)$	Value of x -direction of vector r

Frames:

${}_I e$	Inertial frame
${}_1 e / {}_2 e / {}_3 e / {}_4 e$	Joint frames (origin in the center of 1 st , 2 nd , 3 rd and 4 th joint)
${}_{c1} e / {}_{c2} e / {}_{c3} e$	Cylinder frames (origin in the center of the opening joint of 1 st , 2 nd and 3 rd cylinder)

Indices:

x_1, x_2, x_3	Piston extension from cylinder center of 1 st , 2 nd and 3 rd cylinder
c_{1s}, c_{2s}, c_{3s}	Center of opening joint of 1 st , 2 nd and 3 rd cylinder
c_{1e}, c_{2e}, c_{3e}	Center of closing joint of 1 st , 2 nd and 3 rd cylinder
j_1, j_2, j_3	Center of 1 st , 2 nd and 3 rd joint
cg_1, cg_2, cg_3	Center of gravity of 1 st , 2 nd and 3 rd link
cg_{t1}, cg_{t2}	Center of gravity of 1 st and 2 nd torque link
t_1	Joint center of torque link 1 (opening)
t_2	Joint center of torque link 2 (opening)
t_3	Joint center of torque link 3 (closing)
ct	Crane-tip
ct_d, α_d, β_d	Desired crane-tip position and corresponding joint angles

Symbols:

q	Vector of generalized coordinates
α	1 st joint variable
β	2 nd joint variable
x_3	3 rd joint variable
T	Kinetic energy
T_{trans}	Translational kinetic energy

T_{rot}	Rotational kinetic energy
V	Potential energy
Q	Generalized forces
ω	Angular velocity
m	Mass
I	Inertia tensor
J	Jacobian matrix
g	Gravity acceleration vector
f	Force vector
M	Mass matrix
h	Vector of gyroscopic and active forces
y	State vector
l_c	Length of cylinder frame
l_{os}	Offset start (opening joint – start of cylinder frame)
l_{oe}	Offset end (end of cylinder frame – closing joint)
l_p	Length of cylinder piston
l_r	Length of cylinder rod
l_c	Offset end (end of cylinder frame – closing joint)
φ_1	Slope angle of 1 st cylinder referred to ${}_1e$ -frame
φ_2	Slope angle of 2 nd cylinder referred to ${}_2e$ -frame
$\varepsilon_1, \varepsilon_2$	Slope angles of 1 st and 2 nd torque link referred to ${}_2e$ -frame
ψ_i	Auxillary angles in 1 st cylinder frame
θ_i	Auxillary angles in 2 nd cylinder frame
r_2	Swivel radius of 3 rd joint about 2 nd joint
r_3	Swivel radius of crane-tip about 3 rd joint
r_{diag}	Distance between 2 nd joint and crane-tip
x_s	Spool stroke
u	Control input
p_0	Tank pressure
p_s	Supply pressure
p_N	Nominal pressure
C_0	Constant discharge coefficient
Q_N	Nominal flow
Re	Reynolds number
ν	Kinematic fluid viscosity
p_{tr}	Transition pressure
p_A, p_B	Cylinder chamber pressures

ω_n	Natural frequency
ω_d	Ringling frequency
ζ	Damping ratio
k	Spring stiffness
c	Damping factor
τ	Time constant
A_1, A_2	Cross-sectional area of upper and lower cylinder chamber ($A_1 > A_2$)
F_{fr}	Friction force
F_g	Gravitational force
$V_{0,1}, V_{0,2}$	Initial cylinder volumes
V_1, V_2	Dynamic cylinder volumes
d_c	Diameter of cylinder frame
d_r	Diameter of cylinder rod
ρ	Density of hydraulic fluid
q_{int} / q_{ext}	Internal / External leakage flow
E_{oil}	Bulk modulus of oil elasticity
C_1, C_2	Oil constants
k_{int} / k_{ext}	Leakage coefficients
μ	Static friction coefficient
z	Average bristle deflection
F_C	Couloumb friction force
F_N	Nominal force
F_v	Viscous friction force
k_v	Viscous friction coefficient
δ_v	Viscous friction gradient
F_S	Static friction
F_{St}	Stribeck friction
v_σ	Stribeck velocity
δ_σ	Stribeck gradient
$\alpha_0, \alpha_1, \alpha_2$	Static friction parameters
σ_0, σ_1	Dynamic friction parameters
k_p, k_i, k_d	PID control gains
e	Control error

Table of contents

1	BACKGROUND.....	11
1.1	A TYPICAL FORWARDER IN USE	11
1.2	VEHICLE CONSTRUCTION OF A FORWARDER	12
1.3	THE MAIN WORKING PRINCIPLE	13
1.4	PROBLEM DEFINITION.....	15
1.5	GOAL	15
1.6	RECENT APPROACHES AND PREVIOUS WORK.....	16
1.7	TOOLS	17
2	THE LABORATORY CRANE.....	18
2.1	SYSTEM DESCRIPTION.....	18
2.2	DESCRIPTION OF THE CRANE COMPONENTS AND ASSEMBLIES [7]	19
2.2.1	<i>Rigid Beams</i>	19
2.2.2	<i>Hydraulic system</i>	19
2.2.2.1	Hydraulic cylinders.....	20
2.2.2.2	Valve package	20
2.2.2.3	Hydraulic power unit	21
2.2.3	<i>Sensors</i>	22
2.2.3.1	Pressure sensors.....	22
2.2.3.2	Load sensors	23
2.2.3.3	Angular sensors.....	23
2.2.3.4	Position sensor	24
2.2.4	<i>Peripheral equipment</i>	25
2.2.4.1	<i>dSpace</i> system	25
2.2.4.2	Amplifier box.....	25
2.2.4.3	Interface box.....	26
2.3	SKETCHES OF THE CRANE ELEMENTS.....	26
2.3.1	<i>Link sketches</i>	27
2.3.1.1	Sketch of the 1 st link	27
2.3.1.2	Sketch of the 2 nd link.....	27
2.3.1.3	Sketch of the torque link	28
2.3.1.4	Sketch of the 3 rd link	28
2.3.1.5	Sketch of the 4 th link	29
2.3.2	<i>Cylinder sketches</i>	29
3	MECHANICAL MODEL.....	31
3.1	KINEMATICS OF THE CRANE	31
3.1.1	<i>Rotation matrices</i>	33
3.1.1.1	Rotation matrices of link frames	33
3.1.1.2	Rotation matrices of cylinder frames.....	34
3.1.2	<i>Kinematic chains</i>	40
3.1.2.1	Determination of forward kinematics.....	40
3.1.2.2	Determination of inverse kinematics	41
3.1.2.2.1	Joint variable α	44
3.1.2.2.2	Joint variable β	45

3.1.2.2.3	Joint variable x_3	46
3.1.3	Workspace	46
3.2	DYNAMICS OF THE CRANE	47
3.2.1	Euler-Lagrange formulation	48
3.2.2	Kinetic energy	48
3.2.3	Potential energy	50
3.2.4	Generalized forces	51
3.2.5	Equations of motion	52
4	HYDRAULIC MODEL	54
4.1	MATHEMATICAL MODEL OF THE SPOOL VALVE	54
4.1.1	Static model of the spool valve	54
4.1.1.1	Valve configuration	54
4.1.1.2	Working principle	56
4.1.1.3	Flow equations	58
4.1.2	Dynamics of the spool valve	61
4.2	MATHEMATICAL MODEL OF THE CYLINDER	64
4.2.1	Static model of the cylinder	64
4.2.2	Dynamics of the cylinder	66
5	MODELLING OF HYDRAULIC FRICTION	70
5.1	FRICTION PHENOMENA	70
5.1.1	Static friction model	71
5.1.1.1	Coulomb friction	71
5.1.1.2	Viscous friction	72
5.1.1.3	Static friction (Stiction)	73
5.1.1.4	Stribeck friction	74
5.1.2	Dynamic friction model	76
5.1.2.1	Dynamic properties of friction	76
5.1.2.2	The LuGre Model	77
5.2	ESTIMATION OF NOMINAL FRICTION PARAMETER	80
5.2.1	Experimental set-up	80
5.2.2	Static parameter estimation	83
5.2.3	Dynamic parameter estimation	89
5.2.3.1	Estimation of dynamic parameter σ_0	89
5.2.3.2	Estimation of dynamic parameter σ_1	92
5.2.4	Influence on friction due to variations in load and pressure	94
6	CONTROL OF THE CRANE	96
6.1	CONTROL TASK	96
6.2	INVERSE JOINT CONTROL	97
6.2.1	PID control	98
6.2.2	Control algorithm	99
6.2.3	Optimization	100
6.3	PERFORMANCE OF CRANE MODEL WITH PID-CONTROL	101
7	CRANE MODELLING IN MATLAB	106
7.1	COMPLETE SET OF STATE SPACE EQUATIONS	106

7.2	MATLAB-CODE 'CRANE_MAIN'	107
7.3	MATLAB-CODE 'DIMENSION'.....	117
7.4	MATLAB-CODE 'PLOT_CHARTS'.....	120
8	CONCLUSIONS AND OUTLOOK.....	127
9	APPENDIX.....	128
9.1	DATA SHEETS	128
9.2	CD-ROM.....	133
9.2.1	Content.....	133
9.2.2	CD-Rom attachment	133
10	BIBLIOGRAPHY	134

1 Background

1.1 A typical forwarder in use

Swedish economy is characterized by a market heavily orientated towards foreign trade in which the agricultural sector is of great importance. Within this branch, timber products account for an essential part of the export market. This emanates from a highly forested land utilization in Sweden (see Figure 1), recently not least because of improved transportation and distribution systems. Consequently agricultural technology plays an important role in the forest-based industry. In the middle part of southern Sweden there exist numerous manufacturers for forestry machines, all of them offer products to facilitate and speed-up the machining in wood proceedings. Some of the companies are joining, together with the Universities of Växjö and Kalmar, a research group named *Heavy Vehicles* (swed. *Tunga Fordon*), whose ambition is to develop know-how and advancement in technology in order to make the forestry vehicles become more efficient.

One of the members within this research group is Rottne Industri AB, a leading manufacturer in logging machinery that has his headquarters located in Rottne, nearby the town of Växjö. In Sweden, Rottne Industri covers approximately 15% of the market for forestry machines with a production capacity of up to 200 machines per year. The company develops and manufactures a wide range of forwarders and harvester machineries covering everything from first thinning to clear felling. All of the machines are equipped with a hydraulic crane for handling the timber logs. It is a major objective within the sector to continually improve the efficiency and reliability of the forestry machines, predominantly by introducing more automated steering control. For research purposes Rottne Industri has provided one of their forwarders that is now located in the laboratory of the technology department at Växjö University. On the basis of this prototype of a forwarder, practicable research activities like sensor feedback and programmable control could be done in the laboratory hall of Växjö University.

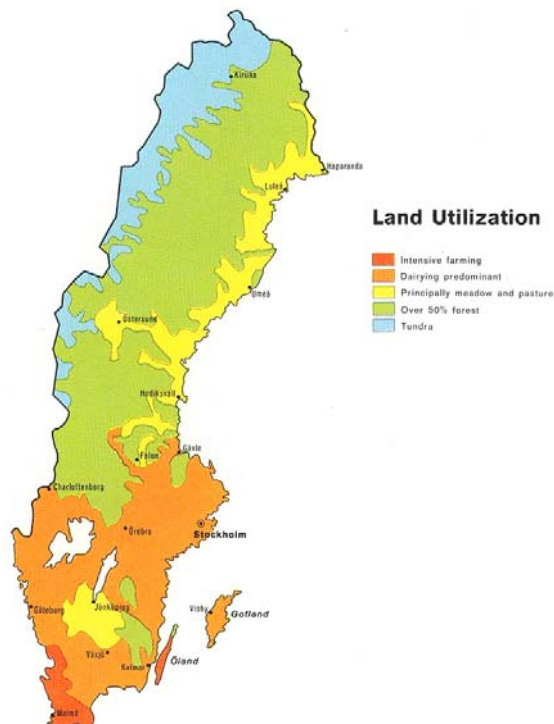


Figure 1: Land utilization in Sweden

Forestry work often consists of monotonous work steps that could be performed automatically facilitating the human work and thus save time and energy. A main limitation but also an essential way to enhance the efficiency of forwarders is the control interface of the crane. Nowadays the crane is manoeuvred manually by well-trained and experienced operators. They undertake the task of controlling each cylinder separately in order to move the crane-tip to its desired position. Consequently the operator has to use several levers and buttons simultaneously which complicates a precise and effective realization of the handling operation. In respect of this, the forestry industry is particularly interested in a more direct and easier way of controlling the crane in order to relief the driver from parallel operations. The answer to this problem is a control mechanism which allows controlling the crane-tip in a plane Cartesian frame, namely the up-down motion with one lever and the forward-backward motion using a second lever.

In comparison to harvester machines that are additionally utilized in operations for felling, delimiting and cutting trees, a typical forwarder is used to haul the log from the stump to a roadside landing. Beside stability and flexibility, good tracking is one of the major conditions in order to carry out good log-hauling in a densely wooded working environment. Primarily forwarders are equipped with a powerful hydraulic system that has made them extremely popular within the class of heavy articulated vehicles. Since most of the forwarders consist of many moving parts, they are regarded as high maintenance wheelers. In the following sections a short description of the constructive aspects and the control principle are given.

1.2 Vehicle construction of a forwarder

Depending on performance and load carrying capabilities, forwarders nowadays exist in several versions that not only vary in dimension and size but also in power transmission, hydraulic equipment and steering. Whereas light weight built machines are employed in logging operations with load capacities of eight metric tonnes, Rottne's *Solid Rapid* forwarder for example can carry payloads of up to 16 tonnes.



Figure 2: Rottne forwarder *SMV Rapid* [15]

The machines are characterized by a robust frame design with powerful articulated joints, wide wheels and a load area with a low center of gravity for providing a good ground clearance. Hence forwarders have an excellent stability which makes them use the full reach and lifting capacity of the loader. Commonly they have a high ground pressure which allows climbing over rocks and stumps as well as travelling through deep snow or wet lands. Forwarders are basically equipped with a 24 volt electrical system for control and monitoring operations. The motion of each crane link is quick and easy actuated by hydraulic cylinders that are connected to a powerful hydraulic system. The system together with its working principle is specified in chapter 1.3. Generally the manipulator is a forward linkage of three beams with an additional telescopic extension arm. With this configuration the forwarder has a broad reach and a flexible operating mode which makes it a particularly suitable vehicle under exceedingly difficult conditions in the forest.

1.3 The main working principle

There exist several classifications of robot manipulators with variations in power source (hydraulic, electric, pneumatic), control method (servo / non-servo, closed loop / open loop) and application area (assembly / non-assembly). Depending on its field of application, a robotic system is also defined by its geometry. Several ways of linked motions are possible, e.g.:

- articulated manipulators (three revolute joints)
- spherical or SCARA manipulators (two revolute and one prismatic joint)
- cylindrical manipulator (one revolute and two prismatic joints)
- cartesian manipulator (3 prismatic joints)

The laboratory forwarder from Rottne Industri is of the type of an articulated manipulator. It is also termed anthropomorphic manipulator because its joints are placed in a human specific linkage. The system design is shown in Figure 3 but it should be annotated that the Rottne forwarder is additionally equipped with an extractable telescopic forearm on which the gripper is mounted.

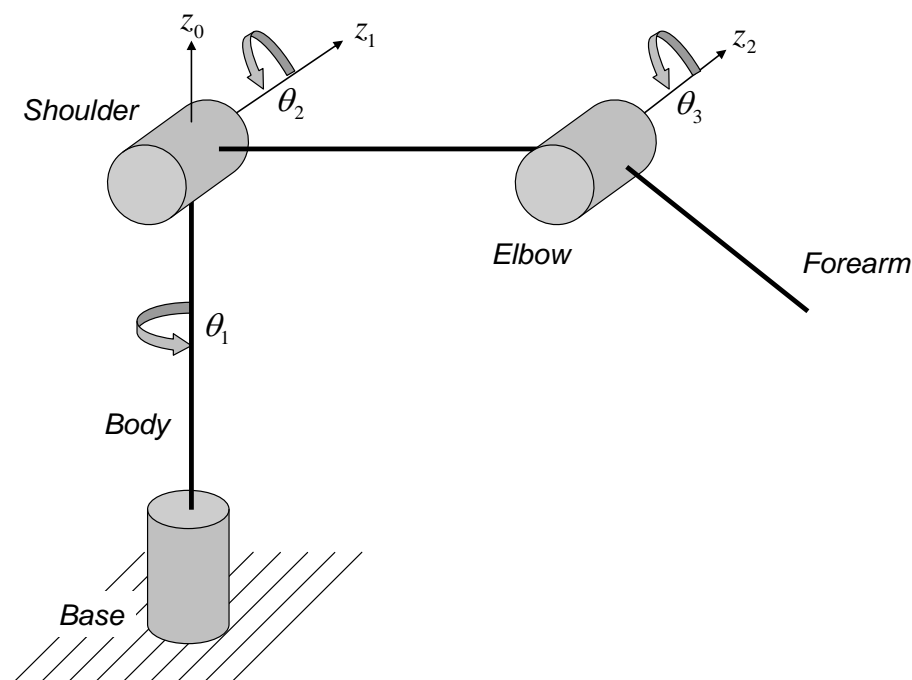


Figure 3: Anthropomorphic manipulator

The configuration in Figure 3 allows the gripper for reaching a wide working area, still being most flexible and accessible. Often robotic systems are also valued in accuracy (attribute of how close the end-effector can come to a given point) and repeatability (attribute of how close the end-effector can return to a previously taught point), that are both highly dependent on the resolution of the signals, the backlash in the joints, the control algorithm and several outer influences.

The control of a robotic system involves several tasks, beginning from signal perception and data processing to the actuating operations of the cylinder. A typical robotic paradigm of the anthropomorphic manipulator is given in Figure 4:

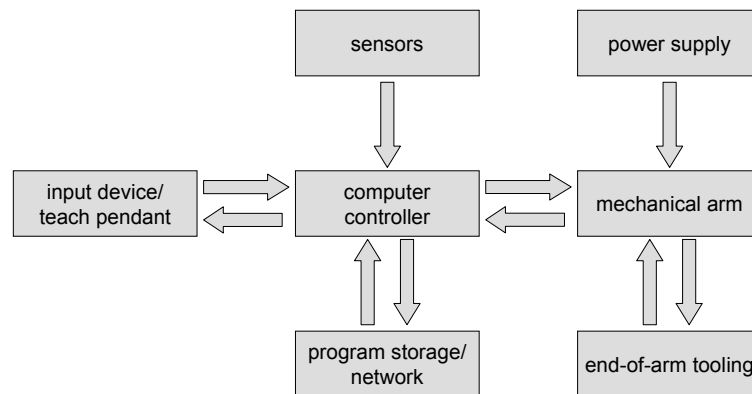


Figure 4: Robotic paradigm

By using an input device, e.g. a teach pendant, the desired operation is commanded to the CPU. Sensors provide the necessary feedback information about the environment, the joint angles or the position of the end-effector. The adaptive control algorithm is implemented in the computer network and is responsible for calculating and generating a suitable output signal to the actuators that will move the mechanical structure.

Forwarders are heavy machines that use a powerful hydraulic system to do work. The control principle is based upon articulated steering joint with double acting cylinders. A crane operator easily controls the valves from within a cabin and consequently distributes the fluid directly through the circulated load-sensing hydraulic system. Hydraulic fluid is transmitted under high pressure throughout the hydraulic hoses into the cylinder chambers. Thus, the cylinder force acts on the linkage and manoeuvres the coupled arms of the crane. By use of different cylinder dimensions, the resulting force of each cylinder can be specified according to its requirements. This phenomenon is demonstrated in Figure 5:

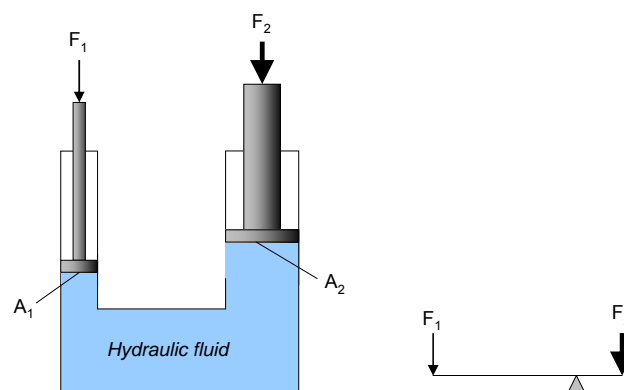


Figure 5: Mechanical analogy of hydraulic cylinders

Under equal chamber pressure for example, a hydraulic cylinder with two times the diameter of another cylinder ($d_2 = 2d_1$) can exert a force that is four times higher since

$$F_2 \sim A_2 = \frac{d_2^2 \pi}{4} = \frac{4d_1^2 \pi}{4}$$

By making use of this phenomenon, a hydraulically operated crane is able to carry extremely high payloads, which makes it perfectly cut out for log hauling operations in the forest.

1.4 Problem definition

Human operators of forestry machines are confronted with several multi-tasks at the same time, e.g. controlling of up to four crane actuators, cutting and thinning operations as well as steering and manoeuvring of the actual vehicle. The simultaneous work inevitably burdens the operator extremely which might lead to losses in efficiency and performance. As a result of this, several projects have been initiated within the mentioned project groups in order to come up with new strategies and methods to disburden the human operator and to increase the benefit of forestry machines.

One of the problems to tackle is the control of the crane actuators. Nowadays they have to be controlled by at least two joysticks that are independently connected to the hydraulic system. With this kind of joystick configuration each hydraulic cylinder is addressed separately which might counteract the intended motion of adjacent links. Hence, in order to control the crane-tip to a desired position, the different joystick functions have to be balanced repetitively as the operator controls the joint angles and not really the position of the gripper.

The cylinders used for actuating the laboratory crane offer complicated and dynamical friction behaviour. When using control algorithms for the manoeuvring of the crane links, friction may become a major problem, causing the performance of robotic systems to deteriorate. Friction occurs in all kind of mechanical systems that are in motion, in our case it is most notably as cylinder friction inside the hydraulic actuators. This implicates losses in the accuracy of our model, typically due to steady-state errors in position regulation and tracking lags. For an effective control method it is therefore of great importance to involve friction compensation schemes that capture the friction effect and thus counteract the arising frictional force.

1.5 Goal

One of the major goals of this work is to build up a complete model of the crane dynamics, including the hydraulic system and real body dimensions. This will be phased in different steps, beginning with a detailed investigation of the crane parameters, a derivation of the kinematics and dynamics of the crane links, the cylinders and the valve block. Furthermore the developed model has to be consolidated afterwards allowing the performance of crane simulations in *MATLAB/Simulink*.

Another goal of this work is to simplify the operating control steps and consequently increase the performance of the crane by using a more advanced control principle. This should be done via control algorithm that uses the joystick command input for a direct control of the end-effector. A basic PID control will be implemented that combines the inverse crane kinematics with optimization methods.

A major aim of this work is to capture the friction phenomenon that occurs during the motion of the hydraulic cylinders. In order to provide friction compensation schemes it is most essential to estimate the individual friction force to an accurate extent. Therefore we have to set-up a cylinder test rig for friction evaluation and run several experiments that enhance the dynamical aspects of the friction force. The evaluated friction maps and nominal friction

parameters can then be used for further compensation schemes. It should be pointed out that the friction maps will be used to create a reference friction model. However, this work does not offer adaptive friction compensation schemes but this should be a major topic of the forthcoming works within the project at Växjö University.

1.6 Recent approaches and previous work

In recent years technical advancement within the field of forestry machines has been a major interest in Northern Europe. There are several ongoing works that deal with the topic of enhanced control algorithms for harvesting machines, mainly in order to introduce a certain degree of automatization to these machineries. Automatic performance will sooner or later speed up the working steps and at the same time ease the workload of the human operators. At present time, new control strategies for the hydraulic crane are one of the major subjects when it comes to employ automatized processes to forestry machines. Within this scope, trajectory-controlling of the crane's end-effector is the preferential research issue and hence numerous papers have been published on this topic, most notably *Crane-Tip Control of a Hydraulic Crane* by Kalle Prorok.

There have been several approaches in modelling of the crane dynamics. Numerous different crane types can be found today, but the main basic philosophies are the same no matter what the intended application is. One of the models is presented in [2]. This work has addressed the crane characteristics with some simplifications, e.g. simplified joint connection without torque link, linear illustration of the bodies, frictionless cylinder motion, etc. Furthermore the dynamics have been modelled in *Dymola* whereas this paper involves models that are coded in MATLAB.

The forestry research Institute of Sweden *Skogforsk* is the central research body for the Swedish forestry sector and pursue demand-driven applied researches in the forest technology. Several projects including optimization in control strategies have been terminated and can be reviewed in numerous papers. One of the world pioneers in the field of crane control was Björn Löfgren, who has written articles over a couple of decades [2]. The author's motivation is the work on crane-tip control from several different points of view. His examinations of the difference between new control algorithms and traditional human control concluded, as expected, in a more efficient work in the forest while reducing the work burden on the human operators.

There is an on-going work within the project *Intelligent Vehicles Off-Road (IFOR)* at Umeå University, whose long-term focus is an autonomous off-road vehicle. This work describes the simplification in handling of a crane by unloading the driver from complicated geometric transforms. In [9], Kalle Prorok has described a better algorithm compared to previous work and thus tried to make the human control operations more attractive and less prone to muscular disorders. This work is still persisting and in the future navigation issues including advanced sensors will be studied.

Uwe Mettin and Pedro Xavier Miranda La Hera have derived a control system for a hydraulic crane in [1] that is based upon an empirical tuned PID controller with additional feed-forward term for friction compensation. Here, two exemplary simulation models of an autonomous motion are presented and subsequently a comparison with the behaviour of the real machine is shown.

Hydraulic friction is a topic that has been studied considerably for a long time. Consequently there is a wide range of friction models available nowadays. Static friction models for example are extensively discussed in [17]. When it comes to evaluate dynamic cylinder friction, this work will basically focus on the LuGre model that is addressed in several works of Carols Canudas de Wit. In [16] particular emphasis is given to the LuGre model and its behaviour in different situations. There are also methods presented that illustrate friction compensation

and its results from practical experiments. Canudas de Wit also applied model-based adaptive friction compensation on a DC motor in [14]. Here, a proposal of nominal static and dynamic parameter estimation is given. Its principle method is used in this work later on when we will evaluate dynamic friction on the hydraulic cylinders of the laboratory crane.

1.7 Tools

During the project work we have used several computer-aided tools which are described in the following section.

The *part*-model of the laboratory crane has been created and provided by Rottne Industri. Dimensions of the bodies and the crane parameters could be read out in *Solid Works*. The *Solid* environment was also utilized to generate the screenshots that are used in this work for depicting the correlation of the crane linkage.

We used *Simulink* for modelling the hydraulic system, beginning with *Simulink* blocks to capture the cylinder's flow dynamics. Later on we added the valve block including sundry control algorithms. *Simulink* is an object-oriented tool which made it possible to model different systems that could be first handled and put together in the end. As a start to the crane model this method turned out to be most valuable, since its flexibility made us modify and exchange the blocks rather easily.

Afterwards, the whole crane kinematics has been modelled in *MATLAB R2007a* that allowed for solving the derived differential equations. Its *m*-code can be found in chapter 7 as well as on the CD in the appendix of this thesis work.

Friction experiments were performed in the laboratory hall at Växjö University. Since there was no adequate digital control system available in the laboratory, a *dSpace* system was provided by courtesy of Kalmar University. Sensor signals were fed into the *dSpace* hardware and could be readout via the *Control Desk* software. The block models for controlling the valves were created in *Simulink*. *Control Desk* was connected to the *Simulink* environment and in turn, the block models could be converted into *ppc*-files that were required to run the *Control Desk* software.

2 The laboratory crane

Design and construction of harvester machines is an important part for the development of new control possibilities. Therefore we intent to achieve an environment in which new algorithms can be tested. By means of a laboratory crane it is easier and safer to detect possible errors that can result during the development process. By courtesy of Rottne Industri a small type of the *Solid F9* forwarder was provided to the laboratory hall of the department of technology and design at Växjö University in March 2007.

2.1 System description

This type of a forwarder is primarily a thinning forwarder but also, due to its robust design, it can be used for log-hauling operations in small final felling stands. In Figure 6 a sketch of Rottne's *Solid F9-6* forwarder vehicle is depicted, illustrating vehicle body and hydraulic crane. This is the configuration set-up that is used for daily logging work in the forest.

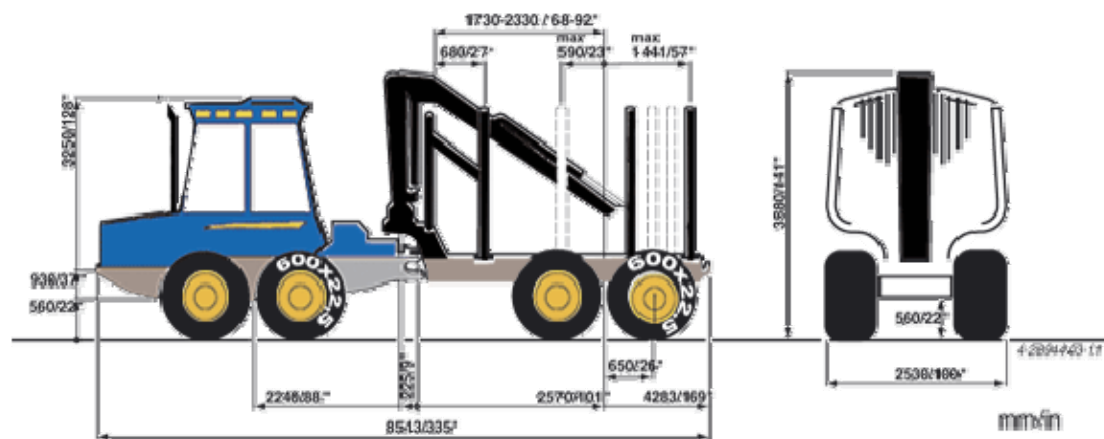


Figure 6: Solid F9 forwarder [15]

The laboratory crane is mounted on a floor stand which is in turn affixed on the concrete floor of the laboratory hall. Hence, the construction is friction-locked so that the crane mount is well-positioned and can't swerve from its origin position. In assembled state the crane consists in principle of mechanical links, joints and hydraulic actuators. The links can be assumed to be rigid - however, there is some sort of flexibility in the joints, most notably when the rotary joint of the 1st link is pivoted very quickly. Anyhow, we can neglect this matter of fact since our developed model only considers movements in two dimensions. Rotation around the vertical axis will not be considered. Accordingly, our crane model consists of three joints, two revolute joints (rotational) for the first arm and one prismatic joint (translatory) for the extension arm. The 2nd link that is attached to the 1st joint is in general referred to as the *boom* arm, the 3rd link is defined as the *jib* arm and the 4th link inside of the jib is simply called *extension* arm (see Figure 7).

The laboratory crane is not equipped with a gripper or a rotator that are in normal operating conditions attached to the crane-tip to handle the logs. The crane weights approximately 1100 kg and when fully extended it measures an operating distance of 5.5 meter. The crane assemblies and components are drafted in Figure 7.

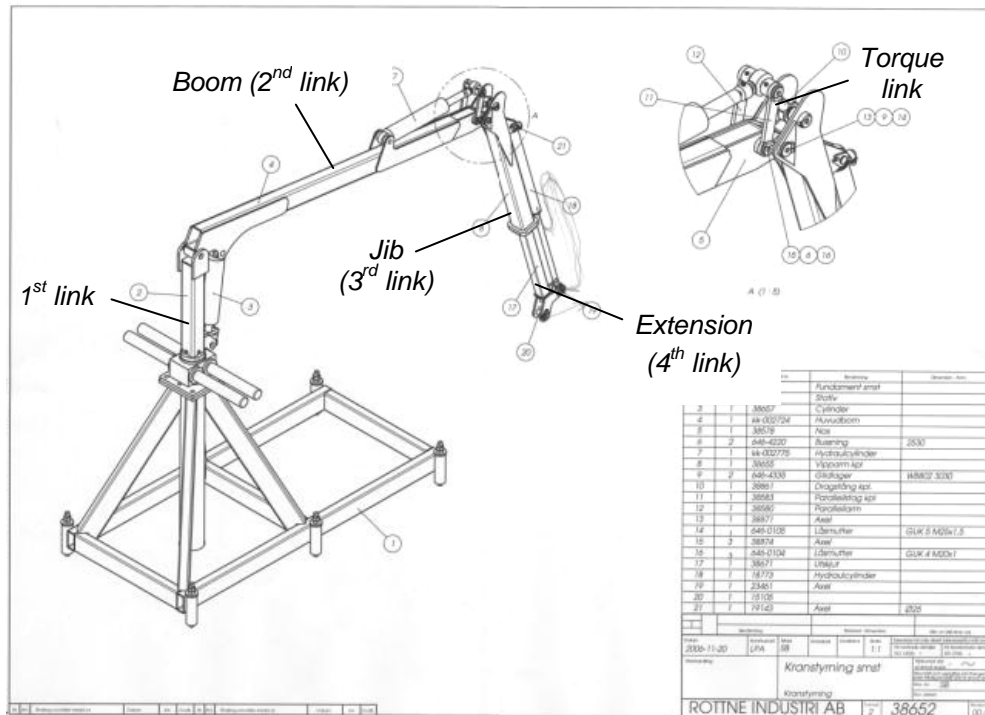


Figure 7: Draft of crane assemblies [12]

2.2 Description of the crane components and assemblies [7]

In this chapter we will describe the crane parts, measuring instruments (transmitters, transducers and amplifiers), the hydraulic system and other peripheral equipments that will be used with the laboratory crane.

2.2.1 Rigid Beams

The crane's framework consists of mechanical links, namely three beams and a telescope beam that slides inside of the 3rd link. All of the crane links will be modelled as rigid bodies. The motivation for this assumption is given by a more straight-forward derivation of the crane dynamics (see chapter 3) which will simplify the equations of motion extremely.

Sketches of the crane links are explicitly given in chapter 2.3, whereas the dimensions of the bodies can be found in the *MATLAB*-code, listed in the appendix at the end of this work.

2.2.2 Hydraulic system

A hydraulic system consists of a pump, a tank, filters, individual types of valves, hydraulic cylinders and hoses between the different units.

Generally a forwarder has separate systems, one for transmission and one for the working hydraulics. The load-sensing hydraulic system is based on the physical principle that fluids are entirely incompressible. The pump delivers an oil flow at high pressure. By controlling the valves, the fluid is delivered to both chambers in the hydraulic cylinder depending on the direction of movement that is desired as oil is dropped simultaneously from the other cylinder chamber. The tank works as storage for oil but it is also important to eliminate the air bubbles that are generated by the pump. There are extra fine filters installed in all hydraulic

applications ($>3\mu$) in order to intercept the particles that are released from the cylinder components. These particles could wear the cylinder components, especially the gaskets inside of the valves and consequently harm the cylinders and distort the straight-forward manner of the mathematic model.

2.2.2.1 Hydraulic cylinders

Hydraulic cylinders are used in order to apply a force to the crane elements that controls the joint motions. In general, hydraulic actuators are much more powerful than electrical actuators of comparable size due to high actuation forces and high power density. Because of their simple construction and low cost, hydraulic cylinders are widely used. A hydraulic cylinder basically consists of the cylinder unit, a piston and gaskets that are located at the intersection of piston and cylinder (see Figure 8).



Figure 8: Sketch of a double-acting hydraulic cylinder

The resulting force arises when letting compressed oil fill one of the spaces between cylinder and piston at the same time as the other one is dropped off. This force depends on the oil pressure inside of each chamber and on the size of the area the pressure acts on. Consequently the flow and both chambers' cross-section areas determine how fast the cylinder piston moves.

There are several manufactures of hydraulic cylinders but the cylinder's diameters are often standardized. On the other hand, stroke and total length can be ordered entirely optional according to the customer's demand. The cylinder sketch is given in Figure 24 and its parameters can be found in the appendix.

2.2.2.2 Valve package

Valve packages exist in a multitude of versions from several manufactures. Traditionally a valve block is designed including a slider that regulates both supply and return port.

The valve package in Figure 9 controls the hydraulic flow by means of separate sliders for each port. Each slider is operated electrically with a spool and a local regulator. This type of valve block includes possibilities for more exact and more flexible control of the crane. For example this makes it possible to set the pressure in the return line deliberately in order to break the movement of the oil. In particular this is favourable when chamber pressures alternate from positive to negative pressure.



Figure 9: Valve block with separated input and output control

2.2.2.3 Hydraulic power unit

A hydraulic power unit consists of a pump, a tank, filters and valves for pressure restriction. There are different types of pumps available depending on the technical solution that is used in order to create the oil flow. The common pump types are gear pumps, radial-piston distributor pumps and axial piston pumps. For flexible hydraulic applications, an axial piston pump is used in most cases since these can be operated with a variable displacement that is the amount of oil that theoretically passes the pump during one rotation. The main advantage is that the pump can be continuously adjusted from zero flow to maximum flow. Thus, this type of pump is very energy efficient and suitable at applications where flow varies heavily.

The assembly of a hydraulic unit and the special performance of the pump depends on the oil flows and the pressures that are requested. For the laboratory crane that implies a capacity of approximately 40 l/min at 200 bar pressure which corresponds to an effective energy of approximately 15 kW. The hydraulic power unit as shown in Figure 10 is located at Växjö University. This unit has a capacity of 60 l/min at 210 bar.



Figure 10: Hydraulic unit at Växjö University

2.2.3 Sensors

There are a number of sensors required in order to operate the crane and to carry out feedback control. The sensors can be used to as direct-input sampling in order to know which condition the crane has at any time.

In Figure 11 the different types of sensors and their location at the crane are sketched.

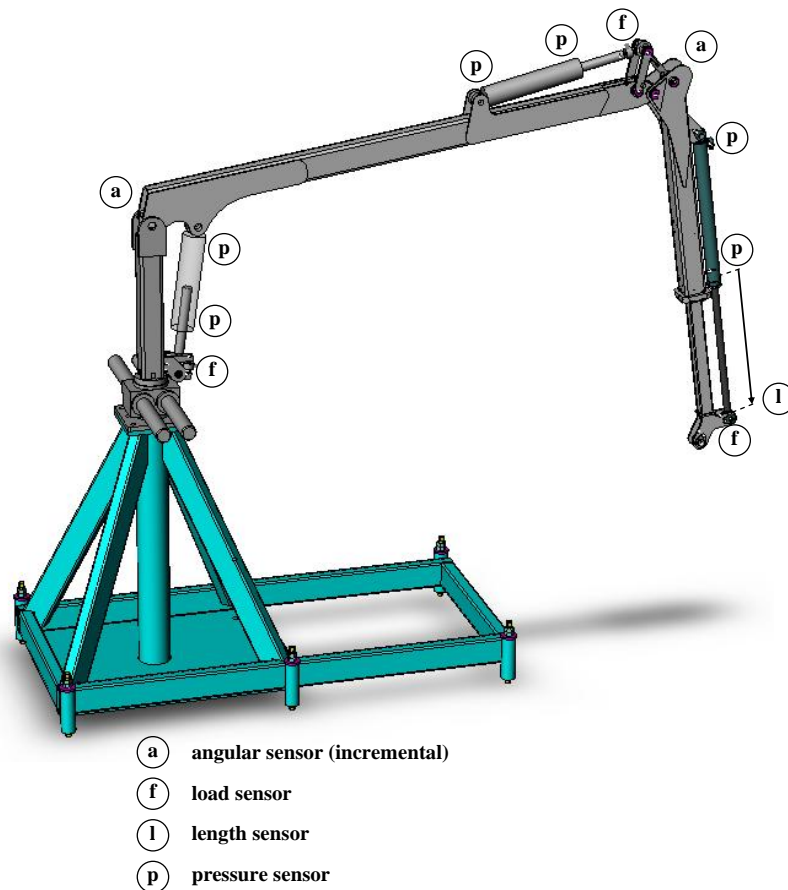


Figure 11: Crane and sensor placement

As mentioned earlier, we will disregard the movement that permits the rotary motion of the whole crane. Therefore we do not have any sensors installed at the 1st joint. Thus, the relevant types of sensors are pressure, position, angle and force sensors. In the following section the sensors are described more detailed along with their particular specifications. Before employing the sensors at the laboratory crane, appropriate connection and signal adjustment has to be done in order to interface with the *dSpace* system. Technical data sheets of the used sensors can be found in the appendix.

2.2.3.1 Pressure sensors

Pressures are often measured using the physical principle that the medium that is pressurized squeezes against a mechanical diaphragm. This diaphragm will deform and thus the deformation can be related to the pressure inside of the medium. In order to obtain a good precision, one has to adjust the measuring area to the expected pressures that arise. A common pressure sensor is shown in Figure 5. Amplifiers are used with pressure sensors in order to obtain a suitable level of the measuring signal.



Figure 12: Pressure sensor MBS 2050

The crane's pressure sensors are of the type MBS 2050 from the manufacturer Danfoss, see Figure 12. The sensors have a measurement range between 0 - 40 MPa and a sensitivity of 0.3% of maximum pressure. The output signal is in the range of 10% - 90% of the supply voltage (5 V) which corresponds to the measurement range.

2.2.3.2 Load sensors

There are several possibilities to measure the resulting force on a cylinder. The laboratory crane is equipped with load cells that can be connected directly between the cylinder and its mounting. These sensors have a good precision but come with the drawback of being comparatively expensive. In Figure 13 the load sensor from HBM is shown.



Figure 13: Load Sensor U9B

For the 1st and 2nd cylinder (lifting and jibbing) sensors with a capacity of 50 kN have been chosen, whereas the sensor of the 3rd cylinder (extending) has a capacity of 20 kN. The sensors have a typical sensitivity of 0.5% of maximum level. The outgoing signal from the sensors is very weak. This is why the sensor has to be connected to an amplifier box to be fed with a supply voltage of 24 V.

Another possibility to evaluate the resulting force of the cylinder chambers is to measure the pressure in both chambers, the gravitation force and derive a friction model describing the size of the friction force precisely (see chapter 5).

2.2.3.3 Angular sensors

In order to measure the rotation angles between adjacent links, incremental sensors are widely used. These should be designed to determine both the direction from the pulse and the zero level in order to avoid resets at each system start. Figure 14 represents an incremental sensor that could be appropriate for goniometry.

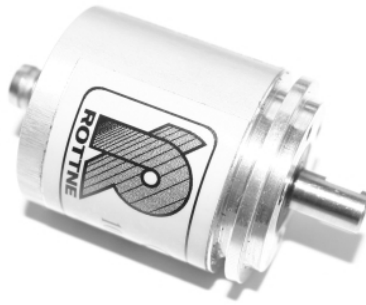


Figure 14: Angular sensor

The angular sensors are from Emeta with a resolution of 1000 pulses per turn, which yields in a resolution of approximately 0.3 degrees per pulse. However, it is possible to obtain a more detailed analysis of the signals. By dividing one turn into 4000 steps the sensors can be operated with a resolution smaller than 0.1 degrees. This resolution corresponds to a crane-tip displacement of 6 mm. The sensors are supplied with 10 V or 24 V.

2.2.3.4 Position sensor

Position sensors are used for measuring the cylinder lengths and speeds. In order to obtain a stable and precise signal, the correct attachment of these sensors is most important. The crane consists of a thread sensor that operates as a common potentiometer by coiling up a thread, which is attached to the telescopic beam. When moving the telescopic beam very quickly, the dynamics in the thread can influence the results, as the spool cannot reel up the thread fast enough. However, the main advantage is that thread sensors are placed externally and thus easily within reach in order to check its function. To avoid the need of resetting the sensor each time the system is powered up, absolute position encoders should be preferably used. Alternatives encoders can be built-in position sensors, which are located inside of the cylinder. However, these sensors are fairly expensive and difficult to attach. The used sensor is shown in Figure 15.



Figure 15: Thread sensors

The length sensor for measuring the telescopic beam extension is produced by Unimeasure and is of a potentiometer type. It is supplied with a voltage of 10 V at a measuring range of 1250 mm.

2.2.4 Peripheral equipment

2.2.4.1 *dSpace* system

In order to convert all sensor signals and at the same time trigger output signals to the valves, a *dSpace* system is used to which all cables are connected. Since we have only one *dSpace* module available we must prioritize the signals of capital importance. The remaining signals may be sampled with external equipments whereas the problem is to synchronize the clock to the *dSpace* system.

The University of Kalmar has provided a *dSpace* system of the type *DS 1044*. This particular system is most appropriate to use with the laboratory crane and is shown in Figure 16.



Figure 16: *dSpace* system from Kalmar University

2.2.4.2 Amplifier box

The following section provides an overview of the amplifiers and voltage supply units. An amplifier box was built at Växjö University¹, its components are assembled on DIN-strips (35 mm) inside of a plastic box to provide a flexible connection to other applications. The main set-up is shown in Figure 17:

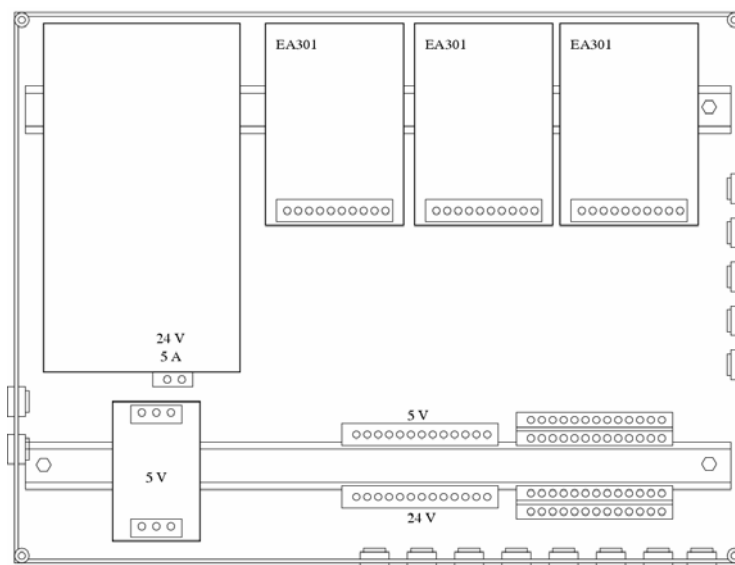


Figure 17: Amplifier box

¹ Thanks to Torbjörn Ekevid, lecturer at Växjö University

The intention of using such kind of box is that all sensors can be fed from voltage sources of 5 V, 10 V respectively 24 V. The signal and supply cables to the sensors are connected on the backside of the box, whereas the output signals to the *dSpace* system are transmitted on the box's left side. On the box's right side there are couplings to provide voltage supply to other applications. A filter is used in order to reduce disturbances that are excited by the main power supply.

2.2.4.3 Interface box

The laboratory crane is controlled via two joysticks. The control signals from the joysticks (related to the joystick deflection) are fed into a so called interface box that forwards the input signals to the input ports of a *dSpace* system². After certain data-processing in the Matlab environment, the converted control signals will be generated back into the interface box. Here, the voltage of the incoming signal will be divided in a defined way to suit the input limitations in *Rottne's* IPS-system. The IPS-box then steers the electronic valves in the valve block of the crane. Figure 18 shows the signal flows between the different hardware parts at the laboratory crane:

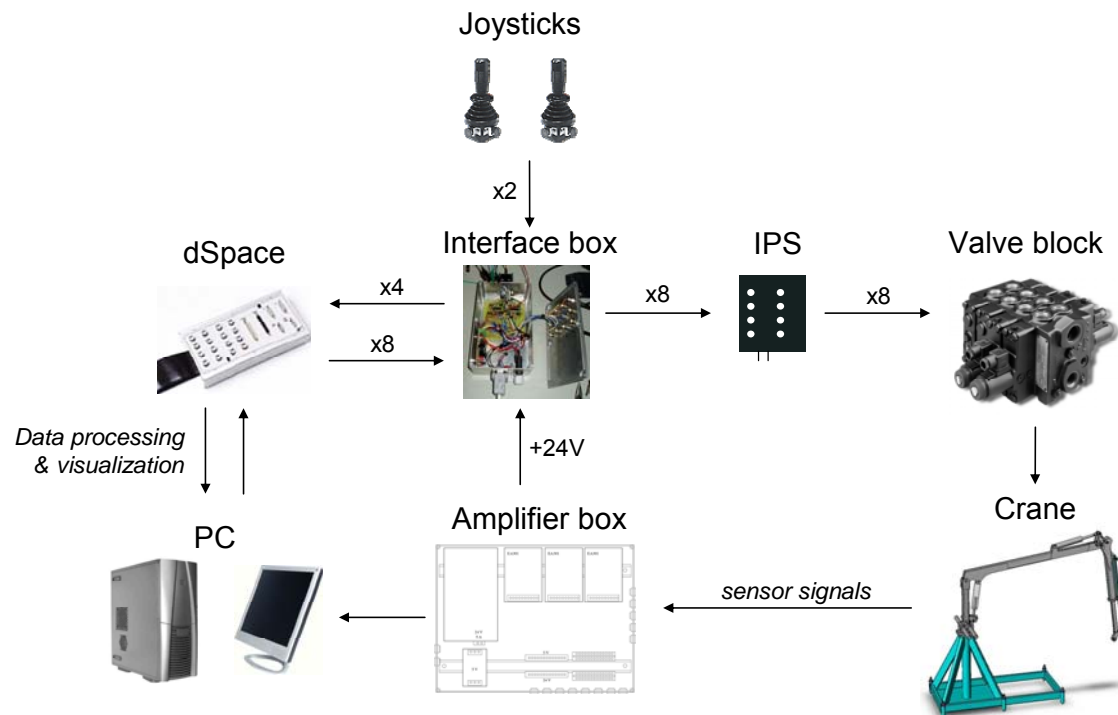


Figure 18: Peripheral equipment and data flow at the laboratory crane

2.3 Sketches of the crane elements

In this chapter we will address the individual crane elements, illustrating the parts that are essential to model the dynamics of the crane. Each link is hereby regarded separately and the coordinates are referred to a local frame that has its origin at each link's rotary joint. We will not explicitly determine the vectors by its specific coordinates in the following section, but one can find the real crane dimensions in the appendix.

² Thanks to Johan Olofsson, student in the department of Electrical Engineering at Växjö University

2.3.1 Link sketches

2.3.1.1 Sketch of the 1st link

We begin with link 1 which is represented in the coordinate frame of ${}_1e$ (Figure 19). One can notice that only the vector to the cylinder's swivel-joint (c_{1e}) and the 2nd joint position (j_2) are necessary to establish a vector chain to the next link. The fact that the ${}_1e_z$ -axis is the inertial frame's vertical gives us the possibility to equate frame ${}_1e$ and the inertial frame ${}_1e$. Furthermore it is not necessary to regard the link's center of gravity since the 1st link is not in motion.

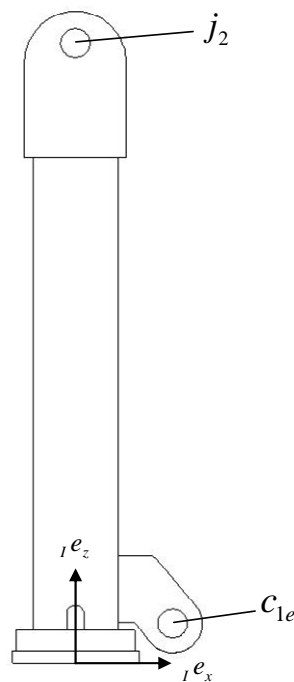


Figure 19: Sketch of the 1st link

2.3.1.2 Sketch of the 2nd link

The second joint combines the 1st link with the 2nd link in the ${}_2e$ -origin (Figure 20). The orientation of ${}_2e$ is determined by its x -axis being parallel to the lower edge of the beam.

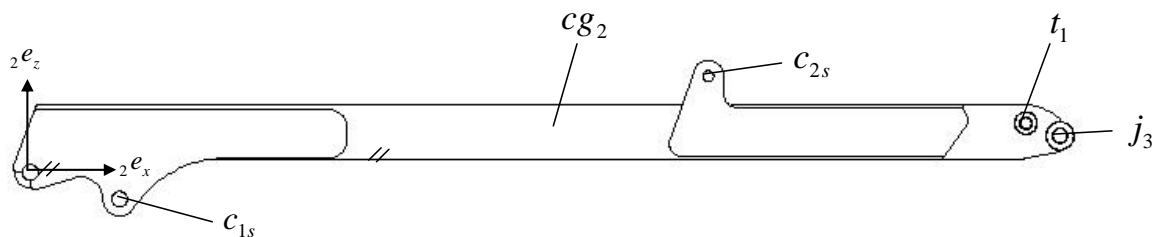


Figure 20: Sketch of the 2nd link

Besides the cylinder joints (c_{1s} and c_{2s}) one has to locate the joint of the 1st torque beam t_1 and the joint in which the 3rd link is pivoted, namely j_3 . Furthermore it is important to identify the center of gravity cg_2 in which the translation and gravity energy is assumed to be stored.

2.3.1.3 Sketch of the torque link

At the end of the 2nd beam, a closed-loop torque linkage is attached to transmit the forces to the 3rd beam. In Figure 21 both torque links are shown along with their centers of gravity and the corresponding joints to the next beam. Notice that ${}_{i2}e$ is fixed in the joint of torque link 1 (j_{i2}) whereby torque link 2 is pivoted to its adjacent link 3 in j_{i3} .

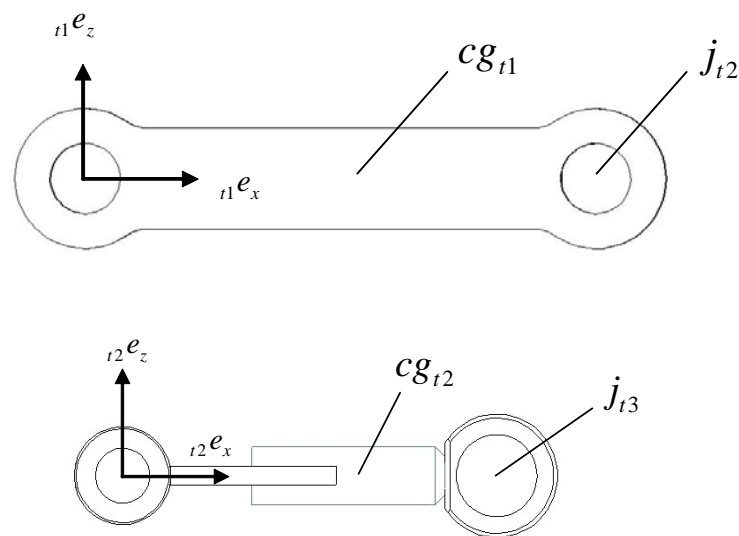


Figure 21: Sketches of the torque links

2.3.1.4 Sketch of the 3rd link

The frame e_3 is placed in joint j_3 and is orientated by the longitudinal direction of the 3rd link (Figure 22). Its necessary coordinates are the center of gravity and the bearing of the 3rd cylinder, namely joint c_{3s} .

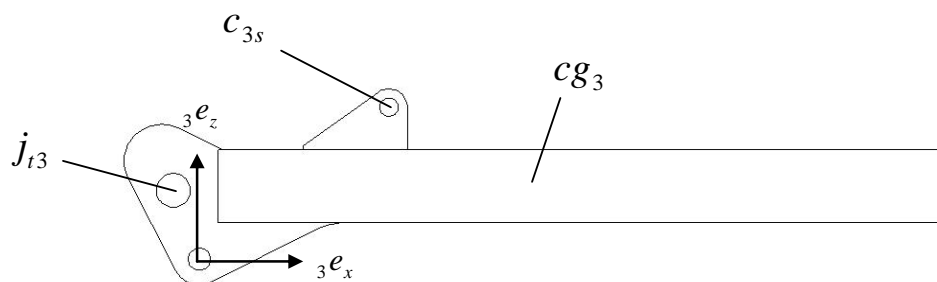


Figure 22: Sketch of the 3rd link

2.3.1.5 Sketch of the 4th link

The telescopic beam is located inside of link 3 and thus, its frame ${}_4e$ has the same orientation as ${}_3e$ (Figure 23). Vertically it is fixed at half the beam's height. Moreover, one has to identify the coordinates of the center of gravity cg_4 , the end position of the 3rd cylinder c_{3e} and the crane-tip position ct .

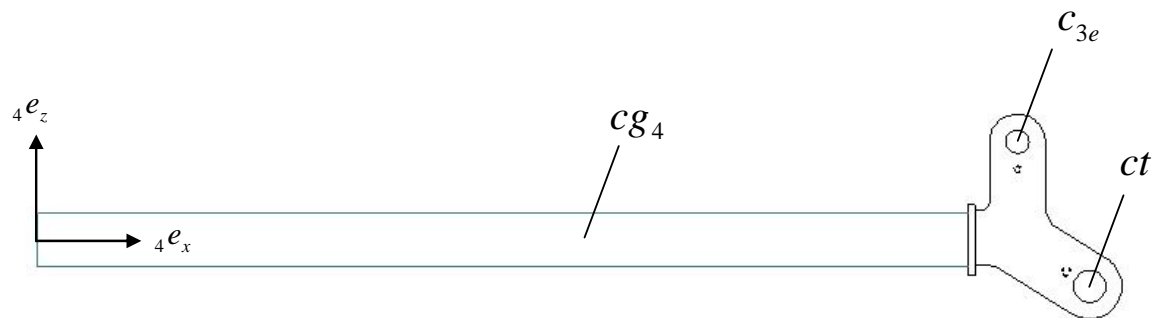


Figure 23: Sketch of the telescopic beam

2.3.2 Cylinder sketches

The laboratory crane is operated by hydraulic cylinders, which serve as actuators. The cylinders are of different size, which results from their individual range of application. By reason of identical constructions we will demonstrate the cylinder parametrization on the basis of the 1st cylinder only. However, it is necessary to fix an own coordinate frame to each cylinder separately, namely in its longitudinal direction (see Figure 24). The resulting slope angle referred to its attached link is then a function of the piston position and will be derived in chapter 3.1.

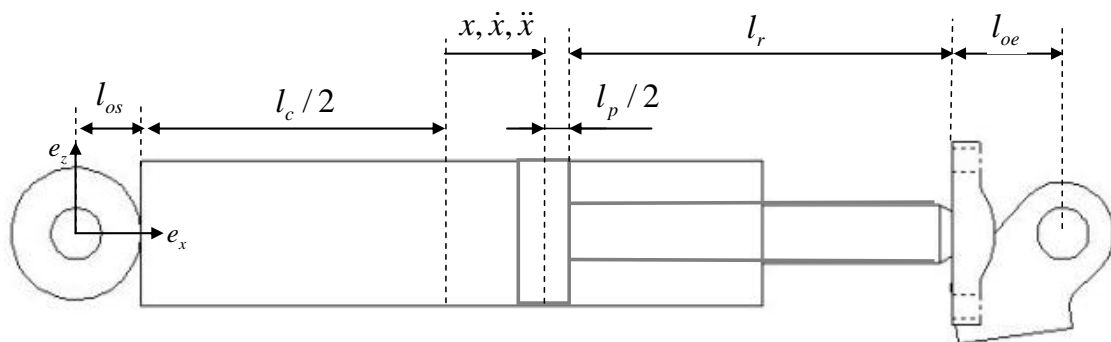


Figure 24: Sketch of the cylinder

The cylinder length is determined by the offset to the cylinder joints at both ends l_{os} and l_{oe} , as well as the lengths of piston, rod and cylinder frame (l_p , l_r and l_c). The only variable remains the stroke of the piston x , whose initial position is assumed to be in the cylinder center. That follows: $x = 0$ at a distance of $l_{os} + l_c/2$ from the cylinder joint.

It is important to note, that all cylinder frames are fixed in the joint in which the cylinder is attached (opening joint). Furthermore the frame's x -axis correlates to the longitudinal direction of the cylinder. From this it follows that cylinder vectors related to its local frame have no portion in y - and z -direction, which holds: $|\vec{r}_c| = \vec{r}_c(x)$.

The cylinder vectors are given as

$${}_{c1}\vec{r}_{c1} = \begin{pmatrix} |{}_{c1}\vec{r}_{c1}| \\ 0 \\ 0 \end{pmatrix} \quad {}_{c2}\vec{r}_{c2} = \begin{pmatrix} |{}_{c2}\vec{r}_{c2}| \\ 0 \\ 0 \end{pmatrix} \quad {}_{c3}\vec{r}_{c3} = \begin{pmatrix} |{}_{c3}\vec{r}_{c3}| \\ 0 \\ 0 \end{pmatrix} \quad (1)$$

with

$$|{}_{c1}\vec{r}_{c1}| = l_{os1} + l_{c1}/2 + x_1 + l_{p1}/2 + l_{r1} + l_{oe1} \quad (2)$$

and $|{}_{c2}\vec{r}_{c2}|$, $|{}_{c3}\vec{r}_{c3}|$ analogical.

One should keep in mind that the frame of cylinder 1 is fixed at the 2nd link. Besides, the 2nd cylinder operates backwards as it is fixed to the torque link. That means the joint angle between the 2nd and 3rd link is decreasing with an increasing cylinder stroke. The position and orientation of each cylinder frame can be seen in Figure 25.

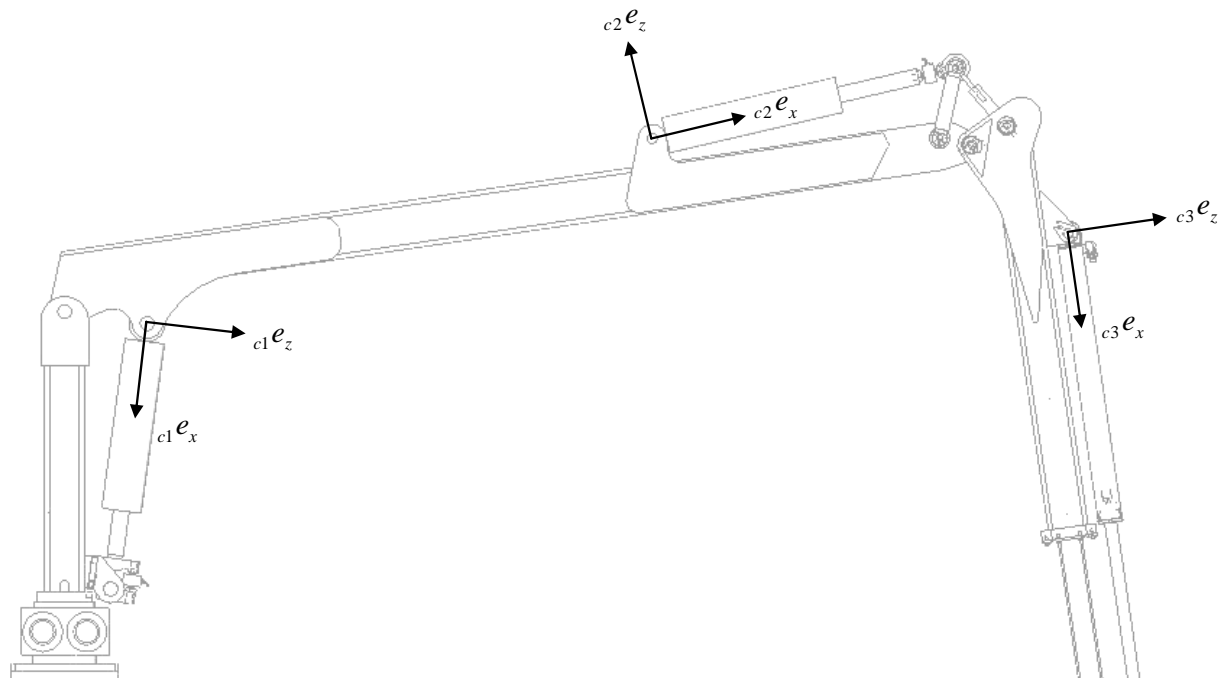


Figure 25: Location and orientation of the cylinder frames

3 Mechanical model

To represent the basic geometric and dynamic aspects of a robot manipulator, one has to define the coherence between the different beams, associated to their adjacent link. In this chapter we will therefore derive a mathematical model of the crane mechanics.

At first we will consider kinematic aspects, including rotational matrices and vector chains. The latter is done in both forward and reverse kinematics. The forward kinematics has to be applied when identifying the position of the crane-tip in terms of the joint variables, whereas the inverse kinematics is used for control purpose. In this regard, one has to identify the joint variables related to the desired position of the end effector. Before we start to model the crane mechanics, some simplifications need to be done in order to keep the mathematical expressions as short as possible. Assumptions are made as follows:

- *The whole model is visually represented in a planar frame that is specified by the rotary joint which is attached to the lower end of the 1st link. It is further used as the inertial frame to which all kinematic vectors are related. Nevertheless we will use vectors of size 3 in order to describe the entire kinetic energy caused by rotation.*
- *The cylinders and its internal components are assumed to be massless and hence store no kind of energy, neither kinetic nor potential energy. This can be assumed due to the fact that the cylinder centers vary merely slightly when the cylinder piston is in motion. The reason for that is the fixed position of the cylinder frame which contributes predominantly to the whole cylinder mass. Rotational energy can be neglected because the cylinder's slope velocities are almost zero (presented in chapter 3.1.2.2).*
- *All parts of the crane, in particular the beams of the crane, are assumed to be rigid bodies and consequently resist any deformation. This denotes that the distance between two points of a link remains constant, regardless of external forces exerted on it.*

3.1 Kinematics of the crane

The main objective of crane kinematics is to establish various coordinate frames in order to represent the position and orientation of rigid bodies. By using transformations among these coordinate frames it is then possible to build vector chains by which all vectors can be expressed in terms of a common inertial frame.

Unlike the Denavit-Hartenberg convention, which is used predominantly in textbooks [4,5], we focus on transformation matrices that describe only the orientation of a frame. This brings the advantage that we are free to choose the orientation of the coordinate frames at each joint and do not have to set it exactly onto an axis of the adjacent frames. Figure 26 shows the procedure of frame setting for orientation purpose and for the Denavit-Hartenberg convention.

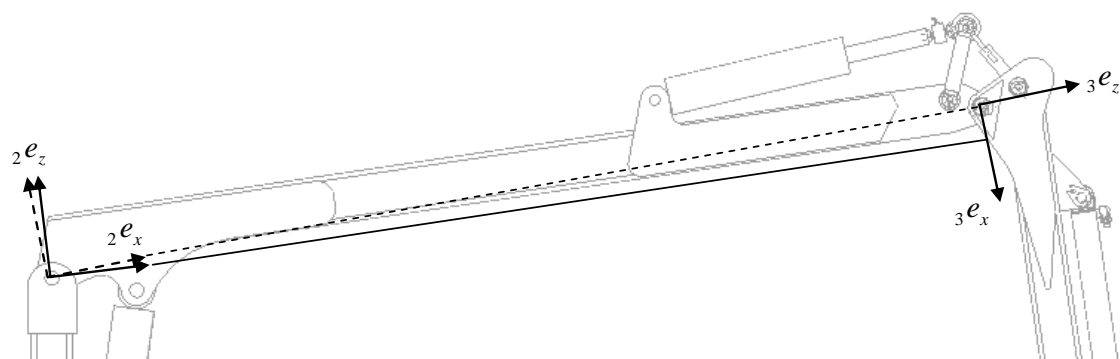


Figure 26: Link-fixed frames (solid line) and Denavit-Hartenberg convention (dashed line)

The dashed frame is used when applying the Denavit-Hartenberg convention. One can notice that its x -axis intersects the 3rd joint in the origin of frame ${}_3e$. However, since we prefer to use the local frames as given in the CAD-model, we chose the orientation of frame ${}_2e$, so that its x -axis is parallel to the lower edge of link 2 (solid line).

As a start to the mechanical model, it is necessary to identify the joint variables that build up the generalized coordinates of the mechanical system. The number of joint variables is well defined by the system's number of degrees of freedom. As our model consists of two rotary joints and one prismatic joint, we write the vector of generalized coordinates as

$$q = \begin{pmatrix} \alpha \\ \beta \\ x_3 \end{pmatrix}, \quad (3)$$

where α is the angle between the 1st link and the 2nd link, β is the angle between the 2nd link and the 3rd link and x_3 is the cylinder extension of the telescopic beam (see Figure 27).

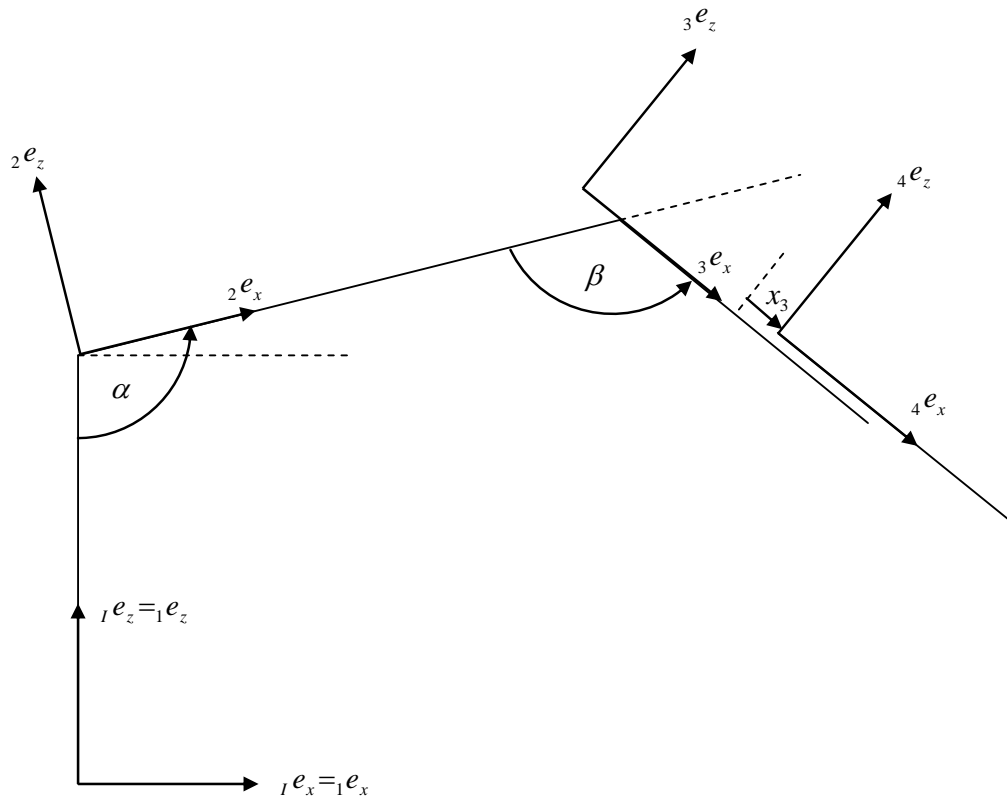


Figure 27: Joint variables and their corresponding frames

Unlike previous definitions of the joint variables, we have defined α and β as the rotation angle from one link to its adjacent link. This brings the advantage, that the angles can be visually verified at the laboratory crane. However, one should keep in mind, that our definition of the joint angles does not directly represent the rotation of the coordinate frames to each other, because the pivoting joint angles are not referred to the same axis. An appropriate determination of the joint angles is addressed in the following section.

3.1.1 Rotation matrices

3.1.1.1 Rotation matrices of link frames

In this section we will address the problem of describing the orientation of a coordinate frame with respect to its adjacent frame. By specifying the geometric relationship between these frames, it is then possible to determine rotation matrices relative to the initial frame. We decide on fixing the initial frame to the rotary joint of the 1st link.

In our case, the transformation can be obtained as an elementary rotation of a reference frame about the y -axis. According to Figure 27 the corresponding rotation matrices in terms of the generalized coordinates are

$${}_1A_2 = A_{y, \frac{\pi}{2} - \alpha} = \begin{pmatrix} \cos(\frac{\pi}{2} - \alpha) & 0 & \sin(\frac{\pi}{2} - \alpha) \\ 0 & 1 & 0 \\ -\sin(\frac{\pi}{2} - \alpha) & 0 & \cos(\frac{\pi}{2} - \alpha) \end{pmatrix} = \begin{pmatrix} \sin(\alpha) & 0 & \cos(\alpha) \\ 0 & 1 & 0 \\ -\cos(\alpha) & 0 & \sin(\alpha) \end{pmatrix} \quad (4)$$

for the 2nd joint and

$${}_2A_3 = A_{y, \pi - \beta} = \begin{pmatrix} \cos(\pi - \beta) & 0 & \sin(\pi - \beta) \\ 0 & 1 & 0 \\ -\sin(\pi - \beta) & 0 & \cos(\pi - \beta) \end{pmatrix} = \begin{pmatrix} -\cos(\beta) & 0 & \sin(\beta) \\ 0 & 1 & 0 \\ -\sin(\beta) & 0 & -\cos(\beta) \end{pmatrix} \quad (5)$$

for the 3rd joint.

As we will model the crane in a planar frame (2-dimensional), we do not have to concern with the rotation of the 1st link about the z -axis. We are then allowed to equal ${}_1A_2$ and ${}_1A_2$.

The extension of the 4th link is based on a prismatic joint, which allows a linear relative motion between the 3rd link and the telescopic beam (4th link). As the telescopic beam is located inside of the 3rd link, they can be seen as invariably parallel to each other, which follows that the 4th link has no rotation about the 3rd joint. Consecutively the rotation from the 4th link to the 3rd link can be expressed through a unit matrix of

$${}_3A_4 = \begin{pmatrix} 1 & 0 & 0 \\ 0 & 1 & 0 \\ 0 & 0 & 1 \end{pmatrix}, \quad (6)$$

which holds that ${}_1A_4 = {}_1A_3$.

When applying kinematic chains in section 3.1.2, we will therefore consider the orientation of ${}_3e$ also as the frame for the referring coordinates of the telescopic beam.

Now, having defined a coordinate frame to each link in terms of the generalized coordinates, we obtain the transformation matrices with respect to the inertial frame by post-multiplication

of the preceding transformation matrices:

$${}_1A_2 = {}_1A_1 \cdot {}_1A_2 = \begin{pmatrix} 1 & 0 & 0 \\ 0 & 1 & 0 \\ 0 & 0 & 1 \end{pmatrix} \cdot \begin{pmatrix} \sin(\alpha) & 0 & \cos(\alpha) \\ 0 & 1 & 0 \\ -\cos(\alpha) & 0 & \sin(\alpha) \end{pmatrix} = \begin{pmatrix} \sin(\alpha) & 0 & \cos(\alpha) \\ 0 & 1 & 0 \\ -\cos(\alpha) & 0 & \sin(\alpha) \end{pmatrix} \quad (7)$$

$$\begin{aligned} {}_1A_3 = {}_1A_1 \cdot {}_1A_2 \cdot {}_2A_3 &= \begin{pmatrix} 1 & 0 & 0 \\ 0 & 1 & 0 \\ 0 & 0 & 1 \end{pmatrix} \cdot \begin{pmatrix} \sin(\alpha) & 0 & \cos(\alpha) \\ 0 & 1 & 0 \\ -\cos(\alpha) & 0 & \sin(\alpha) \end{pmatrix} \cdot \begin{pmatrix} -\cos(\beta) & 0 & \sin(\beta) \\ 0 & 1 & 0 \\ -\sin(\beta) & 0 & -\cos(\beta) \end{pmatrix} \\ &= \begin{pmatrix} -s(\alpha)c(\beta) - c(\alpha)s(\beta) & 0 & s(\alpha)s(\beta) - c(\alpha)c(\beta) \\ 0 & 1 & 0 \\ c(\alpha)c(\beta) - s(\alpha)s(\beta) & 0 & -c(\alpha)s(\beta) - s(\alpha)c(\beta) \end{pmatrix} = {}_1A_4, \end{aligned} \quad (8)$$

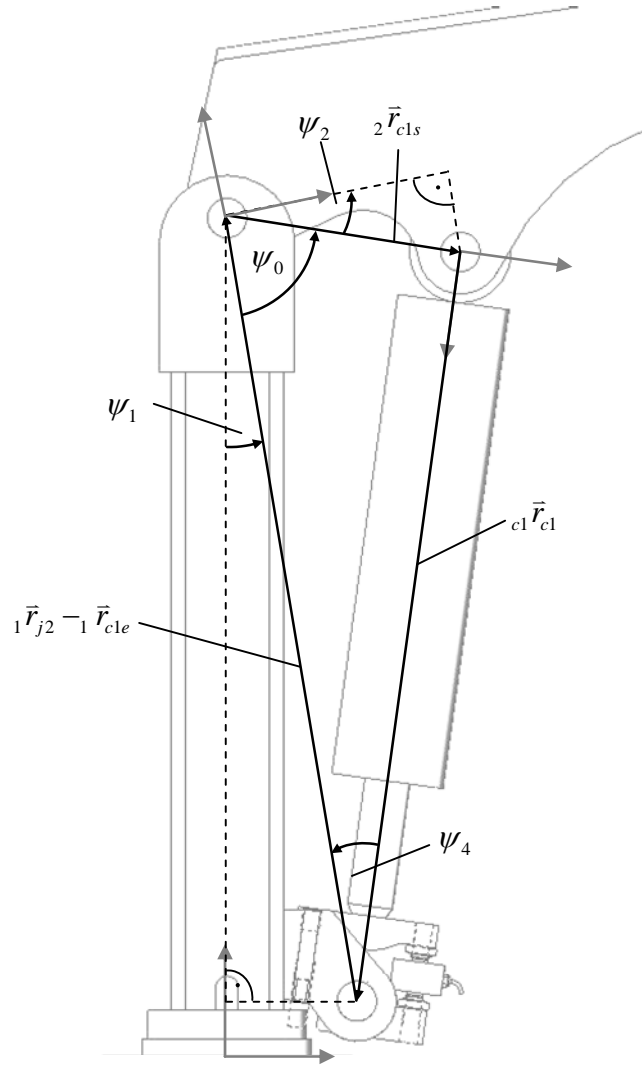
with $s(x) = \sin(x)$ and $c(x) = \cos(x)$ respectively.

One should bear in mind, that only two rotation matrices ${}_1A_2$ and ${}_2A_3$ are necessary to build the vector chains of the crane since ${}_1A_1 = {}_3A_4 = eye(3)$.

3.1.1.2 Rotation matrices of cylinder frames

In order to combine the mechanical model with the hydraulic model it is necessary to determine the direction of the cylinder force. This force can be seen as an external input to the crane mechanics that causes the desired rotation of the joint variables. In this regard we evaluate the cylinders' rotation matrices by using a simple trigonometric approach.

We begin with the first joint variable α , that is computed as a summation of the variable angle ψ_0 and the link-fixed angles ψ_1 and ψ_2 (see Figure 28). Notice, that the dashed lines are parallel to the axes of the corresponding coordinate frame and thus represent its orientation.

Figure 28: Parametrization of α

We apply the law of cosine to the inner triangle in Figure 28 and yield

$$\psi_0 = a \cos \left(\frac{({}_1\bar{r}_{j2} - {}_1\bar{r}_{c1e})^2 + ({}_2\bar{r}_{c2s})^2 - ({}_{c1}\bar{r}_{c1})^2}{2 \cdot |{}_1\bar{r}_{j2} - {}_1\bar{r}_{c1e}| \cdot |{}_2\bar{r}_{c2s}|} \right). \quad (9)$$

In order to obtain ψ_1 and ψ_2 , we refer to a simple vector trigonometry:

$$\psi_1 = a \tan \left(\frac{{}_1\bar{r}_{j2}(x) - {}_1\bar{r}_{c1e}(x)}{{}_1\bar{r}_{j2}(z) - {}_1\bar{r}_{c1e}(z)} \right) \quad (10)$$

$$\psi_2 = a \tan \left(\frac{{}_2\bar{r}_{c1s}(z)}{{}_2\bar{r}_{c1s}(x)} \right) \quad (11)$$

It is important to note that equations 10 and 11 result in negative angles ψ_1 and ψ_2 . In this regard, we have to subtract ψ_1 and ψ_2 from ψ_0 in order to compute the first joint variable α . Plugging the cylinder vector \vec{r}_{c1} in equation 2 gives us a definition of α that describes its direct relationship to the cylinder stroke x_1 :

$$\alpha = a \cos \left(\frac{\left(({}_1\vec{r}_{j2} - {}_1\vec{r}_{c1e})^2 + ({}_2\vec{r}_{c2s})^2 - \left(x_1 + l_{os1} + l_{r1} + l_{oe1} + \frac{l_{c1} + l_{p1}}{2} \right)^2 \right)}{2 \cdot |{}_1\vec{r}_{j2} - {}_1\vec{r}_{c1e}| \cdot |{}_2\vec{r}_{c2s}|} \right) - \psi_1 - \psi_2 \quad (12)$$

As one can notice in Figure 28, the cylinder frame has then been rotated by an angle of $\frac{\pi}{2} + \psi_1 + \psi_4$ related to the inertial frame. This leads to the rotation matrix of the 1st cylinder

$${}_I A_{c1} = \begin{pmatrix} \cos(\frac{\pi}{2} + \psi_1 + \psi_4) & 0 & \sin(\frac{\pi}{2} + \psi_1 + \psi_4) \\ 0 & 1 & 0 \\ -\sin(\frac{\pi}{2} + \psi_1 + \psi_4) & 0 & \cos(\frac{\pi}{2} + \psi_1 + \psi_4) \end{pmatrix} = \begin{pmatrix} -\sin(\psi_1 + \psi_4) & 0 & \cos(\psi_1 + \psi_4) \\ 0 & 1 & 0 \\ -\cos(\psi_1 + \psi_4) & 0 & -\sin(\psi_1 + \psi_4) \end{pmatrix}, \quad (13)$$

where ψ_4 is determined by

$$\psi_4 = a \cos \left(\frac{\left(({}_1\vec{r}_{j2} - {}_1\vec{r}_{c1e})^2 + ({}_c1\vec{r}_{c1})^2 - ({}_2\vec{r}_{c2s})^2 \right)}{2 \cdot |{}_1\vec{r}_{j2} - {}_1\vec{r}_{c1e}| \cdot |{}_c1\vec{r}_{c1}|} \right). \quad (14)$$

However, when modelling the crane in *MATLAB*, tests have shown that processing time is much lower when using a more convenient approach to the rotation angle. Therefore we define the cylinder vector in the inertial frame by means of a vector chain (see chapter 3.1.2) and apply a tangent function to the cylinder vector afterwards in order to obtain ${}_c1e_x$ related to ${}_I e_z$:

$$\psi_1 + \psi_4 = a \tan \left(\frac{{}_I \vec{r}_{c1}(x)}{{}_I \vec{r}_{c1}(z)} \right) = \varphi_1 \quad (15)$$

Here, φ_1 denotes the cylinder slope related to the z -axis of the inertial frame ${}_1e$, however the orientation of the cylinder frame relative to ${}_1e$ and inevitably to ${}_1e$ is determined by a further rotation of $\pi/2$:

$${}_1A_{c1} = \begin{pmatrix} \cos(\pi/2 + \varphi_1) & 0 & \sin(\pi/2 + \varphi_1) \\ 0 & 1 & 0 \\ -\sin(\pi/2 + \varphi_1) & 0 & \cos(\pi/2 + \varphi_1) \end{pmatrix} = \begin{pmatrix} -\sin(\varphi_1) & 0 & \cos(\varphi_1) \\ 0 & 1 & 0 \\ -\cos(\varphi_1) & 0 & -\sin(\varphi_1) \end{pmatrix} \quad (16)$$

Whereas the computing of the transformation of cylinder frame 1 has been fairly simple, it needs some more effort to evaluate the rotation matrix of the 2nd cylinder. The reason for this is a more complex relationship between the joint angle and the cylinder extension due to the fact that a torque link is attached to the end of the 2nd cylinder (see Figure 29).

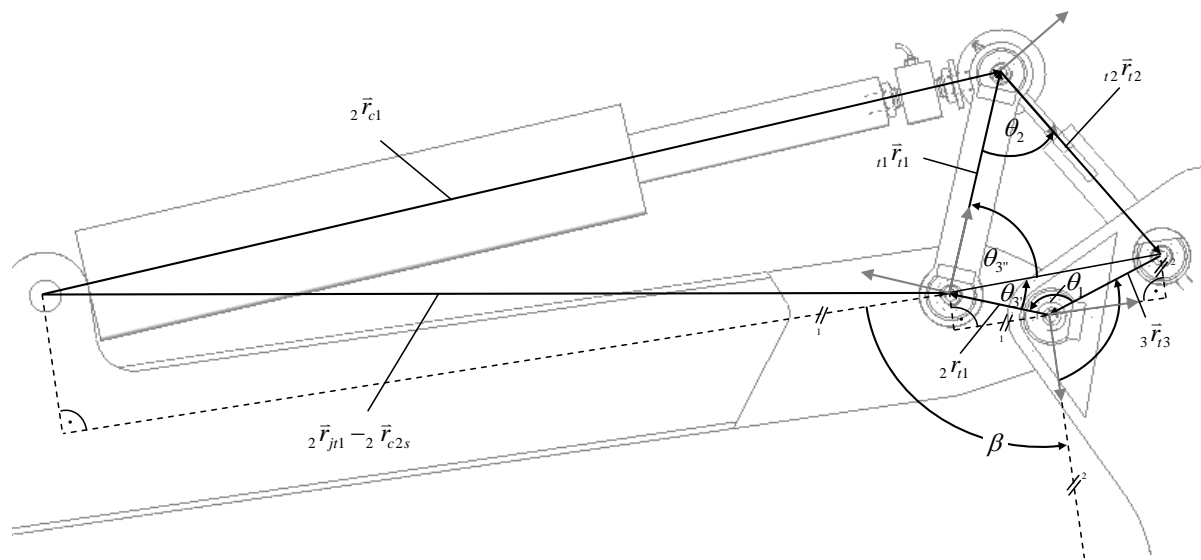


Figure 29: Parametrization of β

We begin with an approach to θ_1 which is the lower angle inside the closed-loop quadrangle $j_3 - t_1 - t_2 - j_{t3}$. Assuming we know the magnitude of β from incremental measuring, θ_1 can then be determined by

$$\theta_1 = 2\pi - \beta - \pi/2 + a \tan\left(\frac{{}_3\bar{r}_{t3}(x)}{{}_3\bar{r}_{t3}(z)}\right) + a \tan\left(\frac{{}_2\bar{r}_{t4}(z)}{{}_2\bar{r}_{t4}(x)}\right) \quad (17)$$

with ${}_2\bar{r}_{t4} = {}_2\bar{r}_{j3} - {}_2\bar{r}_{t1}$.

Once again both $a \tan$ -functions are constant and implicate negative signs, regardless of the joint configuration. Therefore they appear as a positive term at the right hand side of equation 17.

We continue with applying the law of cosine to both triangles that arise when splitting the quadrangle with its horizontal diagonal $\overline{r_{c1}r_{c3}}$:

$$\overline{r_{c1}r_{c3}} = \sqrt{{}_2\bar{r}_{t4}^2 + {}_3\bar{r}_{t3}^2 - 2 \cdot |{}_2\bar{r}_{t4}| \cdot |{}_3\bar{r}_{t3}| \cdot \cos \theta_1} \quad (18)$$

$$\overline{r_{c1}r_{c3}} = \sqrt{{}_{t1}\bar{r}_{t1}^2 + {}_{t2}\bar{r}_{t2}^2 - 2 \cdot |{}_{t1}\bar{r}_{t1}| \cdot |{}_{t2}\bar{r}_{t2}| \cdot \cos \theta_2} \quad (19)$$

Knowing θ_1 , one can easily compute θ_2 by equating the right hand sides of equation 18 and 19. It then holds:

$$\theta_2 = a \cos \left(\frac{{}_{t1}\bar{r}_{t1}^2 + {}_{t2}\bar{r}_{t2}^2 - {}_2\bar{r}_{t4}^2 - {}_3\bar{r}_{t3}^2 + 2 \cdot |{}_2\bar{r}_{t4}| \cdot |{}_3\bar{r}_{t3}| \cdot \cos \theta_1}{2 \cdot |{}_{t1}\bar{r}_{t1}| \cdot |{}_{t2}\bar{r}_{t2}|} \right) \quad (20)$$

Now we take a look at the left hand side of the inner quadrangle. The diagonal divides θ_3 into an upper and lower angle, namely θ_3' and θ_3'' . We apply the law of sine to the arising rectangles and obtain:

$$\theta_3' = a \sin \left(\frac{|{}_3\bar{r}_{t3}|}{|\overline{r_{c1}r_{c3}}|} \cdot \theta_1 \right) \quad (21)$$

$$\theta_3'' = a \sin \left(\frac{|{}_{t2}\bar{r}_{t2}|}{|\overline{r_{c1}r_{c3}}|} \cdot \theta_2 \right) \quad (22)$$

At first sight it is ambiguous that the $a \sin$ -functions in equation 21 and 22 remain positive. Therefore we refer to equation 17 in order to proof that θ_1 is possible to increase beyond 180° , which means that θ_3' is likely to become negative. Inserting the crane's parameters shows that

$$\theta_1 = 2\pi - \beta - \frac{\pi}{2} + a \tan \left(\frac{-0.035}{0.094} \right) + a \tan \left(\frac{0.109 - 0.081}{2.231 - 2.309} \right) = 4.011 - \beta \quad (23)$$

We compute equation 23 and notice that $\theta_1 > 180^\circ$ for $\beta < 50^\circ$. However, since θ_3' also becomes negative, we don't have to concern with this special case any further.

The next step gives us the rotation angle of the 1st torque link. It is determined by a summation of θ_3' , θ_3'' and its correlating angle to the x -axis of frame ${}_2e$:

$$\varepsilon_1 = \theta_3' + \theta_3'' + a \tan\left(\frac{{}_2\vec{r}_{t4}(z)}{{}_2\vec{r}_{t4}(x)}\right) \quad (24)$$

In order to compute to the rotation angle of the 2nd torque link, we simply refer to the already determined angle θ_2 . It holds

$$\varepsilon_2 = \varepsilon_1 + \theta_2 - \pi \quad (25)$$

Finally, the determined torque angles have to be placed in the rotation matrix with their correct signs. The torque matrices referred to the ${}_2e$ -frame are

$${}_2A_{t1} = \begin{pmatrix} \cos(-\varepsilon_1) & 0 & \sin(-\varepsilon_1) \\ 0 & 1 & 0 \\ -\sin(-\varepsilon_1) & 0 & \cos(-\varepsilon_1) \end{pmatrix} = \begin{pmatrix} \cos(\varepsilon_1) & 0 & -\sin(\varepsilon_1) \\ 0 & 1 & 0 \\ \sin(\varepsilon_1) & 0 & \cos(\varepsilon_1) \end{pmatrix} \quad (26)$$

$${}_2A_{t2} = \begin{pmatrix} \cos(-\varepsilon_2) & 0 & \sin(-\varepsilon_2) \\ 0 & 1 & 0 \\ -\sin(-\varepsilon_2) & 0 & \cos(-\varepsilon_2) \end{pmatrix} = \begin{pmatrix} \cos(\varepsilon_2) & 0 & -\sin(\varepsilon_2) \\ 0 & 1 & 0 \\ \sin(\varepsilon_2) & 0 & \cos(\varepsilon_2) \end{pmatrix} \quad (27)$$

In the same fashion as we done when evaluating ${}_1A_{c1}$, we now express the vector of the 2nd cylinder by a vector chain to its start position and its end position and apply a tangent-function to obtain the cylinder's slope angle related to the 2nd link:

$$\varphi_2 = \frac{{}_2\vec{r}_{c2}(z)}{{}_2\vec{r}_{c2}(x)} \quad (28)$$

Finally the rotation matrix of the 2nd cylinder is computed as

$${}_1A_{c2} = \begin{pmatrix} \cos(-\varphi_2) & 0 & \sin(-\varphi_2) \\ 0 & 1 & 0 \\ -\sin(-\varphi_2) & 0 & \cos(-\varphi_2) \end{pmatrix} = \begin{pmatrix} \cos(\varphi_2) & 0 & -\sin(\varphi_2) \\ 0 & 1 & 0 \\ \sin(\varphi_2) & 0 & \cos(\varphi_2) \end{pmatrix} \quad (29)$$

We will not explicitly replace the rotation angles in equation 26 and 27 in terms of the piston stroke as the equations become fairly extensive. The computing in *MATLAB* shows that equation 24 consists of more than 50 different terms and thus it is hard to handle in written form.

3.1.2 Kinematic chains

A kinematic chain can be seen as a structure of several rigid bodies that are connected via kinematic pairs, e.g. by prismatic and revolute joints. The laboratory crane consists of both an open kinematic chain, as well as a closed kinematic chain, which is formed by the torque links that are attached to the 3rd joint. A kinematic chain does not consider forces and torques to the mechanical system, thus it is only a geometric description of the crane.

In this section, we will address both forward and inverse kinematics. Whereas the goal of forward kinematics is to determine the position of the end effector in terms of the joint variables, the problem of inverse kinematics is to find the values of the joint variables given the end effector's position. As opposed to forward kinematics where there is only one possible solution for the end effector's coordinates, there may be multiple solutions for the joint variables when formulating the inverse kinematics problem.

3.1.2.1 Determination of forward kinematics

Direct kinematic equations establish the functional relationship between the joint variables and the position of the end effector. For us, the problem of the forward kinematics is to specify the position of the crane-tip in terms of the generalized coordinates q . Afterwards it must be related to the piston position in order to connect the crane mechanics to the hydraulic model. The crane-tip position is hereby well defined by the joint variables α , β and x_3 , respectively by the cylinder strokes x_1 , x_2 and x_3 . When applying the rotation matrices that have been derived earlier in chapter 3.1.1, we are then able to express vectors from the inertial frame to any point of the crane on the basis of a vector chain.

Below, a set of vectors is given, that describe the distance and orientation of the centers of gravity of all links related to the initial frame ${}_1e$:

$${}_1\vec{r}_{cg1} = {}_1\vec{r}_{cg1} \quad (30)$$

$${}_1\vec{r}_{cg2} = {}_1\vec{r}_{j2} + {}_1A_2 \cdot {}_2\vec{r}_{cg2} \quad (31)$$

$${}_1\vec{r}_{cg3} = {}_1\vec{r}_{j2} + {}_1A_2 \cdot {}_2\vec{r}_{j3} + {}_1A_3 \cdot {}_3\vec{r}_{cg3} \quad (32)$$

$${}_1\vec{r}_{cg4} = {}_1\vec{r}_{j2} + {}_1A_2 \cdot {}_2\vec{r}_{j3} + {}_1A_3 \cdot ({}_3\vec{r}_{c3s} + {}_3\vec{r}_{c3} - {}_4\vec{r}_{c3e} + {}_4\vec{r}_{cg4}) \quad (33)$$

In an analogous manner, the vector to the crane-tip can be computed as

$${}_1\vec{r}_{ct} = {}_1\vec{r}_{j2} + {}_1A_2 \cdot {}_2\vec{r}_{j3} + {}_1A_3 \cdot ({}_3\vec{r}_{c3s} + {}_3\vec{r}_{c3} - {}_4\vec{r}_{c3e} + {}_4\vec{r}_{ct}). \quad (34)$$

The latter vector chain to the crane-tip ${}_1\vec{r}_{ct}$ is also sketched in Figure 30. This vector is of particular importance to the crane control, as it will be used as a feedback signal to the control interface. The main control topic will be discussed separately in chapter 6.

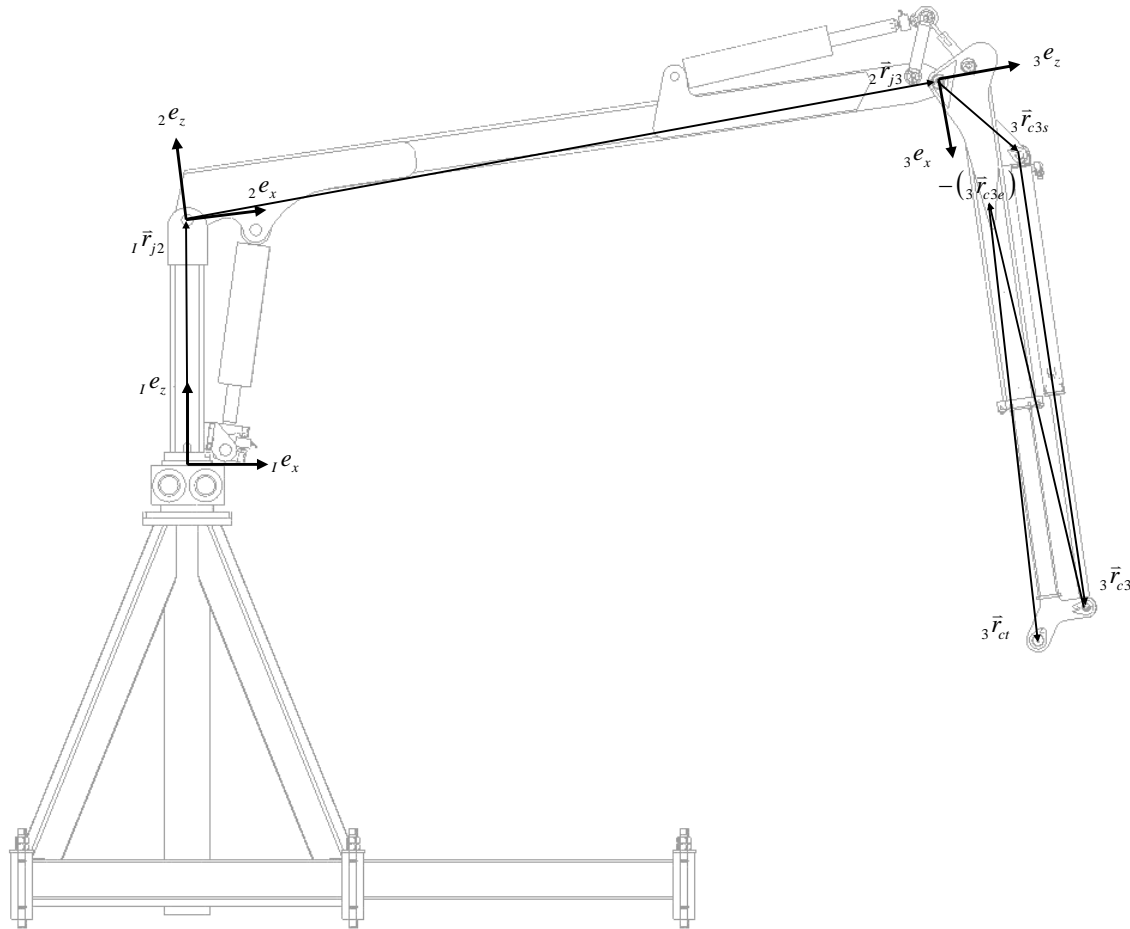


Figure 30: Vector chain to crane-tip ${}_1\vec{r}_{ct}$

3.1.2.2 Determination of inverse kinematics

As one could notice in the preceding section, it was fairly easy to compute the vector coordinates of the crane-tip in terms of the joint variables α , β and x_3 . However, in order to control the crane, we have to apply the principle of inverse kinematics that deals with the problem of finding the joint variables related to a given position of the end-effector. Once knowing the exact joint angle at a certain crane configuration we will develop a systematic algorithm in order to transform the desired motion specifications assigned to the end-effector into the corresponding piston strokes.

The main problem of inverse kinematics is that there may exist more than one possible configuration of the vector of generalized coordinates for a specific position of the end-effector. Besides, the equations to solve are in general non-linear, which might end up in an admissible solution that is out of the cranes working area. The problem of multiple solutions rises, if the number of degrees of freedom is higher than the number of variables that are necessary to describe a given task.

Our first goal is to express the crane-tip position in terms of the generalized coordinates. There are several ways to derive inverse kinematics equations, e.g. as proposed in [4, 5]. These equations are much too difficult to solve directly. Nevertheless we have to identify the joint variables in a closed form without iterative search in order to solve the equations rapidly and thus meet the demands of the sampling rate. Therefore we will apply a geometrical approach to determine the joint variables with relative certainty.

Unlike the problem of forward kinematics that always consists of one unique solution, there may be several solutions or even no solution at all when applying the principle of inverse kinematics. As a start, we set the extension of the telescopic beam to zero, however it will be varied later on in chapter 6. With two degrees of freedom in our system, there are now only two crane configurations possible (see Figure 31):

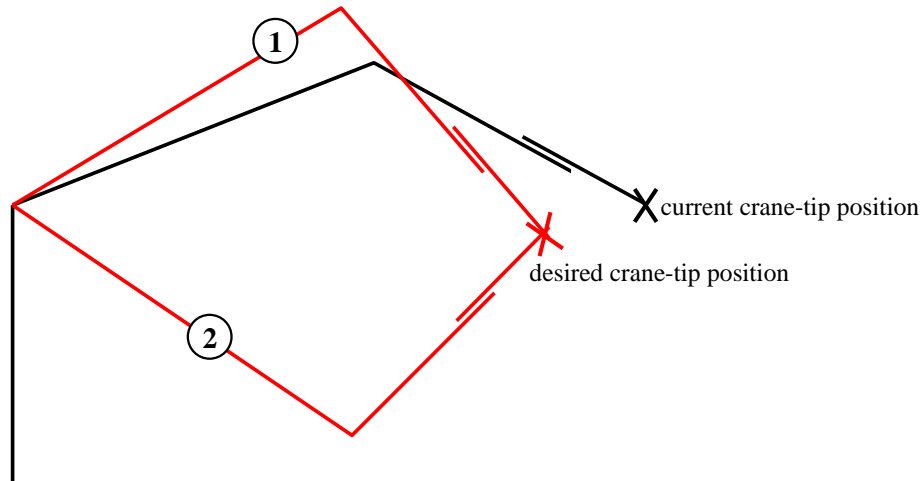


Figure 31: Redundancy of inverse kinematics with 2 possible solutions

The number of possible solutions to the inverse kinematics problem strongly depends on the particular engineering design of the manipulator. With a restriction of the revolute joints α and β to less than 180° , the 2nd solution in Figure 31 then corresponds to a physically unrealizable configuration as β exceeds 180° .

By using a geometrical approach to the problem of inverse kinematics, we are able to define the corresponding set of joint variables α and β for the 1st solution (see Figure 32).

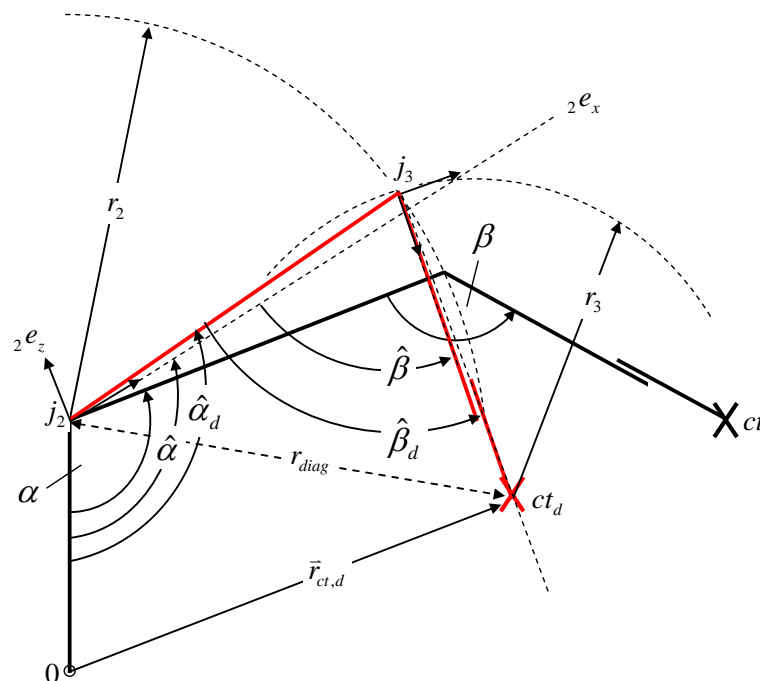


Figure 32: Determination of inverse kinematics

Introducing $\hat{\alpha}_d$ and $\hat{\beta}_d$ as the desired angles related to the joint-to-joint axis, the law of cosine brings us

$$\hat{\beta}_d = a \cos\left(\frac{r_2^2 + r_3^2 - r_{diag}^2}{2r_2r_3}\right) \quad (35)$$

with $r_2 = \overline{j_2j_3}$ and $r_3 = \overline{j_3ct_d}$.

Knowing the desired coordinates of the end-effector, the diagonal that divides the quadrangle $0-j_2-j_3-ct_d$ can be written as

$$r_{diag} = \left| \vec{r}_{ct,d} - \vec{r}_{j_3} \right|. \quad (36)$$

The desired rotation angle $\hat{\alpha}_d$ is then equal to the summation of the upper and lower angle about the 2nd joint. The two angles can be determined by applying the law of cosine to both triangles:

$$\hat{\alpha}_d = a \cos\left(\frac{r_{j_2}^2 + r_{diag}^2 - r_{ct,d}^2}{2r_{j_2}r_{diag}}\right) + a \cos\left(\frac{r_2^2 + r_{diag}^2 - r_3^2}{2r_2r_{diag}}\right). \quad (37)$$

The desired (predetermined) position of the crane-tip and consequently the vector $\vec{r}_{ct,d}$ will be computed in chapter 6 in terms of the joystick control input. However, inserting any possible value for the end-effector's position (within working range) leads to a unique solution.

Finally the slope angles between the frame's x -axis and the joint axis have to be considered. The desired joint variables are then defined as

$$\alpha_d = \hat{\alpha}_d - a \tan\left(\frac{{}_2\vec{r}_{j_3}(z)}{{}_2\vec{r}_{j_3}(x)}\right) \text{ and} \quad (38)$$

$$\beta_d = \hat{\beta}_d + a \tan\left(\frac{{}_2\vec{r}_{j_3}(z)}{{}_2\vec{r}_{j_3}(x)}\right) - a \tan\left(\frac{{}_3\vec{r}_{ct}(z)}{{}_3\vec{r}_{ct}(x)}\right) \text{ respectively.} \quad (39)$$

With equations 38 and 39 the joint angles are now well-defined at a certain crane position. Notice, that such a unique solution only exists at a given extension of the telescopic beam. However, when operating the crane, we will optimize the joint extension by applying the derived formulas for varying cylinder strokes x_3 . The corresponding algorithm will be developed in chapter 6 by means of a penalty function.

3.1.2.2.1 Joint variable α

Having derived the joint angles in terms of the end-effector's position, it is now time to write the piston stroke x_1 and x_2 as a function of the joint variables α and β . By using a trigonometric approach, the orientation of each cylinder frame was given in terms of the generalized coordinates. Therefore we go back to the results of chapter 3.1.1. Solving equation 12 for the cylinder stroke shows that

$$x_1 = \sqrt{-2\cos(\alpha + \psi_1 + \psi_2) \cdot \left| {}_1\vec{r}_{j2} - {}_1\vec{r}_{cle} \right| \cdot \left| {}_2\vec{r}_{c2s} \right| + ({}_1\vec{r}_{j2} - {}_1\vec{r}_{cle})^2 + ({}_2\vec{r}_{c2s})^2} - l_{osl} + l_{r1} + l_{oel} + \frac{l_{c1} + l_{p1}}{2} \quad (40)$$

This particular relationship between the joint angle α and the piston position x_1 is graphed in Figure 33. The MATLAB code can be found in *angle_limits_alpha.m*.

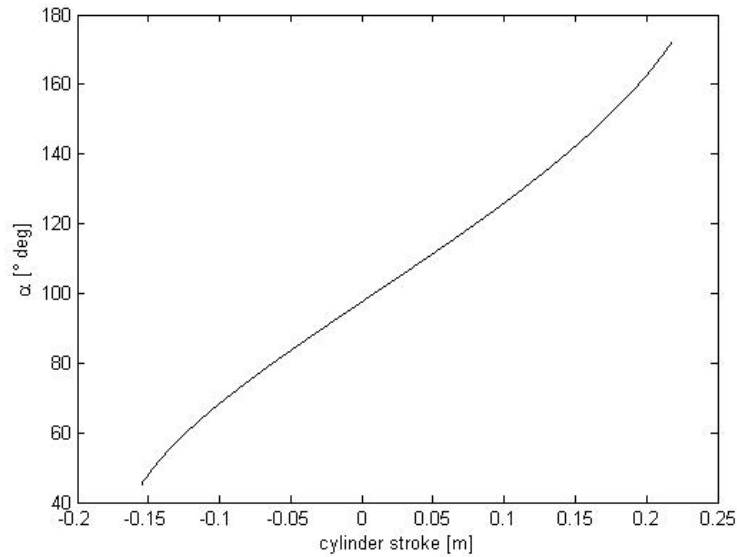


Figure 33: Correlation between joint angle α and piston stroke x_1

When operating the crane it has to be assured that the second link is not rotating beyond an angle of 180° in order to keep the system stable. Therefore we have to define an upper angle-limitation of $\alpha_{\max} = 180^\circ$. However, this configuration would correspond to a cylinder extension that is out of range and thus impossible to obtain. Because of constraints in the cylinder dimension, we can extend the piston to a maximum of $x_{\max} = 217$ mm. As one can notice in Figure 33, this specific threshold corresponds to a maximum joint angle of $\alpha_{\max} = 172^\circ$. Consequently, we have to apply this angular limitation to the control parameters in order to restrict x_1 from extending logically beyond the cylinder's end. Figure 33 also shows that the maximum cylinder retraction of $x_{\min} = -0.155$ mm (due to the rod length) leads to a limitation in the lower angle of $\alpha_{\min} = 45^\circ$. These geometrical restraints have been approved and verified with the corresponding configuration at the laboratory crane.

Furthermore it appears that the relationship between α and x_1 is almost linear, most notably in the range of $-0.1 \text{ m} < x_1 \leq 0.15 \text{ m}$. In any case the designers try to keep this relation linear in order to facilitate manual operating of the crane.

3.1.2.2.2 Joint variable β

In chapter 3.1.1 we have learned that it is quite a big effort to compute the rotation matrices of the torque links in chapter 3.1.1. Now we take advantage of these results and state the relation between the 3rd joint variable β and the stroke of the 2nd cylinder x_2 .

In a first step, it is our goal to determine the overall vector of the 2nd cylinder in terms of β . For this purpose, we apply a closed vector chain from the second joint to both the start position and the end position of the cylinder and yield

$${}_2\vec{r}_{c2} = {}_2\vec{r}_{t1} + {}_2A_{t1} \cdot {}_{t1}\vec{r}_{t1} - {}_2\vec{r}_{c2s}. \quad (41)$$

One should notice, that the joint variable β is hidden in the rotation matrix ${}_2A_{t1}$.

Now we proceed in the same way as we did when computed the stroke of the 1st cylinder - we substitute the cylinder vector ${}_2\vec{r}_{c2}$ with the individual cylinder elements (equation 2) and rewrite equation 41 with focus on the piston length x_2 :

$$x_2 = |{}_2\vec{r}_{c2}| - l_{os1} + l_{r1} + l_{oe1} + \frac{l_{c1} + l_{p1}}{2} \quad (42)$$

In this case, the above-quoted relationship between β and x_2 is rather complex since β appears in several terms of $|{}_2\vec{r}_{c2}|$. Thus we do not give an extensive formulation of $x_2(\beta)$ at this point. Instead we compute this particular relationship with *MATLAB* again, which yields in the following figure (*m-file: angle_limits_beta.m*):

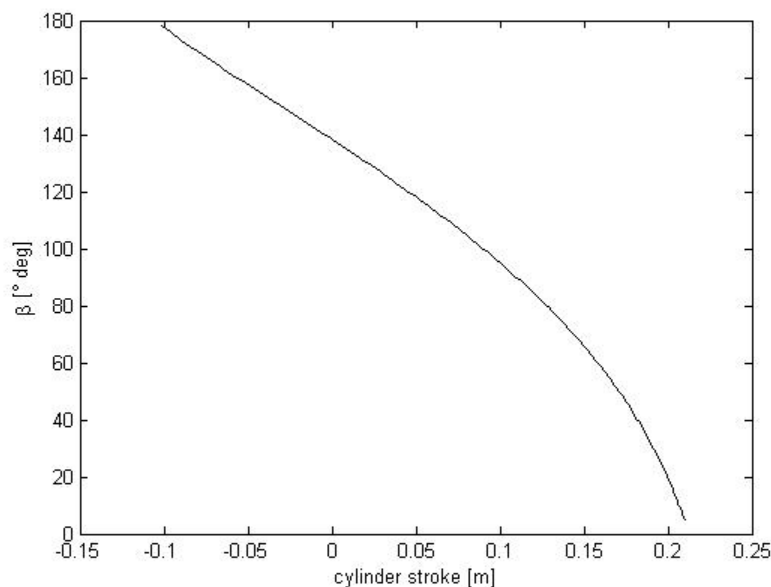


Figure 34: Correlation between joint angle β and piston stroke x_2

According to Figure 34, the maximum angle of $\beta_{\max} = 178^\circ$ is reached at a retraction stroke of $x_{2\min} = -0.101$ m. This retraction determines the upper angular limitation as it corresponds to the end position of the cylinder. As one can notice, certain linearity is given below a cylinder extension of approximately $x_2 = 0.150$ m. When moving the piston further than this threshold, the relationship becomes rather non-linear until the cylinder reaches its maximum extension of $x_{2\max} = 0.210$ m at a joint angle of $\beta_{\min} = 5^\circ$.

3.1.2.2.3 Joint variable x_3

The 3rd cylinder steers the extension and retraction of the telescopic beam. As it has no rotation around any axis, the only limitation for this cylinder is due to its cylinder length. With a total length of the cylinder of $l_c = 0.71$ m and a piston length of $l_p = 0.08$ m, the maximum cylinder extension and cylinder retraction are $x_{3\max} = 0.315$ m and $x_{3\min} = -0.315$ m respectively. It is obvious that the relation between the piston stroke and the extension of the telescopic beam is directly proportional.

3.1.3 Workspace

The workspace of the crane represents the portion of the environment that the crane's end effector can access. As we model the crane in a planar frame with no rotation about the z -axis, the total workspace is then the total area swept out by the crane-tip as all possible motions are executed.

In our case, the robot is designed as an anthropomorphic manipulator, because the links are designated as the body, upper arm, and forearm respectively. Its geometry is realized with three revolute joints and a prismatic joint, which provides a larger workspace than other kinematic geometries relative to its size. This feature becomes extremely indispensable with increasing log size and thus a large accessible working area is of great importance for an effective forwarder.

The working area is constrained by the geometry of the crane links as well as the operating range of its joint variables. The mechanical constraints on the joints have been determined in the previous section and are summarized in Table 1:

Joint variable	Minimum value	Maximum value
α	45°	172°
β	5°	178°
x_3	-0.315 m	0.315 m

Table 1: Limitations of joint variables

With this set of limitation, we apply the possible range of joint variables to the *MATLAB* model *workingarea.m* in order to define the various positioning of the crane-tip. The operating working area of the crane manipulator is shown in Figure 35:

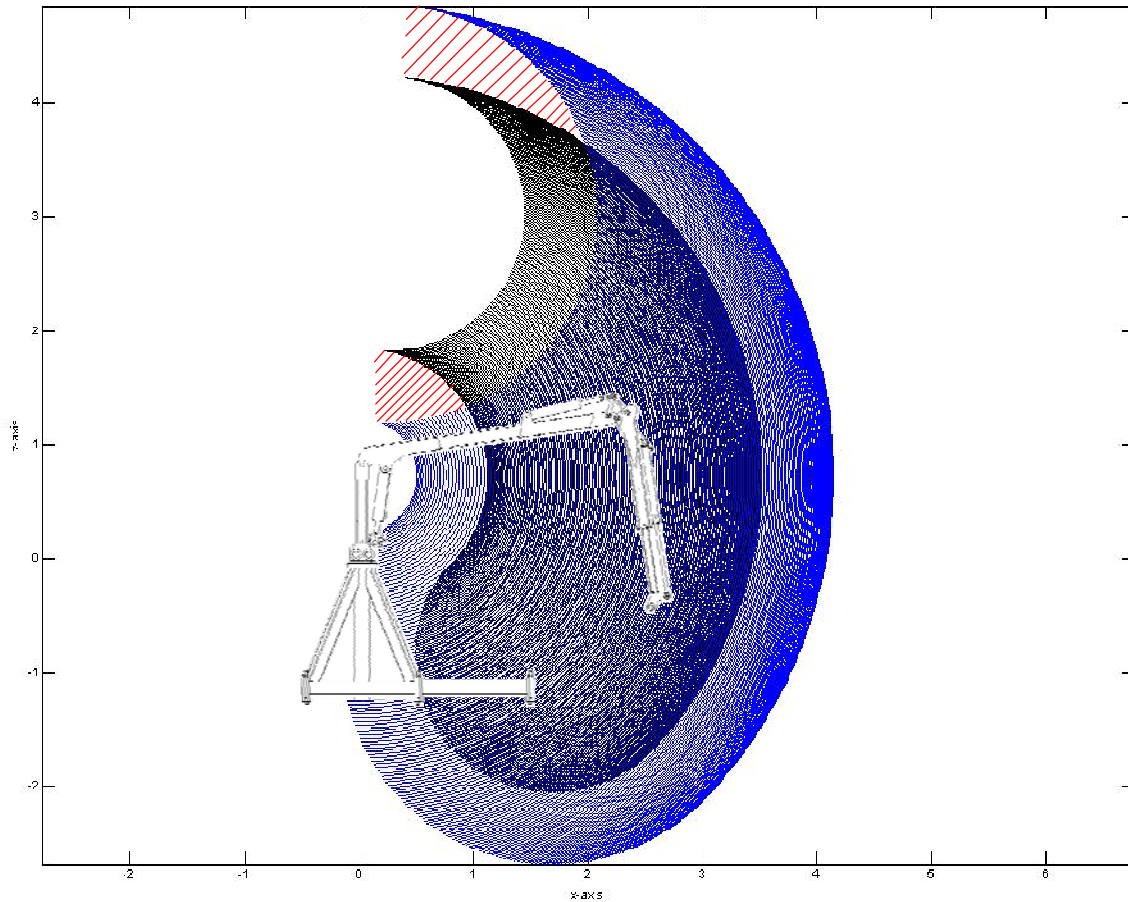


Figure 35: Working area

The blue area represents the position of the crane-tip accessible with a maximum extension of the telescopic beam whereas the black area gives the operating position with a maximum retraction of the telescopic beam. The red area (clearance between upper and lower end of bubbles) is accessible with extensions in between the limitation range.

Also notice, that Figure 35 represents all possible crane-tip positions only because of cylinder limitations. However, we will further define some more constraints in chapter 6 due to obstacle avoidance as well as safety tolerance. The latter will be implemented in the control algorithm in order to slow down the crane-tip before leaving its working area.

3.2 Dynamics of the crane

The derivation of a dynamic crane model plays an essential role in simulation of crane motions. Whereas the kinematics equations of chapter 3.1 describe the crane's motion without regarding the interacting forces and torques, the dynamics formulate explicitly the relationship between force and motion. In this chapter we will therefore consider the equations of motion that are most important for the simulation and the design of new control algorithms. This allows testing of control and motion planning strategies without the need of a physical system.

3.2.1 Euler-Lagrange formulation

The dynamic approach in this work is based on the Euler-Lagrange method that describes the motion of a mechanical structure with holonomic constraints. Since the Euler-Lagrange formulation is straightforward, there is no need to consider joint forces explicitly. The whole mechanical system is divided into several parts whereas the individual equations will be consolidated in the end. In order to determine the Euler-Lagrange equations, we will formulate the system's Lagrangian, namely the difference between the system's kinetic energy and potential energy.

At the beginning of chapter 3 we defined the set of variables that is represented by the vector of generalized coordinates q . Notice that the number of degrees of freedom determines the vector size. In our case the vector consists of three joint variables, that is two revolute joints and one prismatic joint. Consequently, the vector of generalized coordinates q efficiently describes the position and orientation of the links in a planar frame.

As a function of the generalized coordinates, the Lagrangian L of the system can be defined as

$$L = T - V, \quad (43)$$

where T is the total kinetic energy and V is the total potential energy of the system respectively.

The general Lagrange equations is written in the form of

$$\frac{d}{dt} \frac{\partial L}{\partial \dot{q}} - \frac{\partial L}{\partial q} = Q, \quad (44)$$

where Q is the vector of generalized forces associated with q . The terms of the Lagrangian will be determined in the next sections.

3.2.2 Kinetic energy

The total kinetic energy of a rigid body is given by two terms - the translational kinetic energy (relative to the motion of each link) and the rotational kinetic energy (relative to the motion of each joint). It is written as a summation of the energy stored in each link:

$$T = T_{trans} + T_{rot} = \sum_{i=2}^n \left(\frac{1}{2} {}_I \bar{v}_{i,cg}^T m_i {}_I \bar{v}_{i,cg} + \frac{1}{2} {}_I \omega_i^T A_{ii} I_{ii} A_{ii}^T {}_I \omega_i \right), \quad (45)$$

where m_i is the total mass of the body i , ${}_I \bar{v}_{i,cg}$ and ${}_I \omega_i$ are the linear and angular velocity vectors related to the inertial frame and ${}_i I_i$ denotes the inertia tensor about the individual centers of gravity $r_{i,cg}$. The vectors necessary for computing the kinetic energy are sketched in Figure 36:

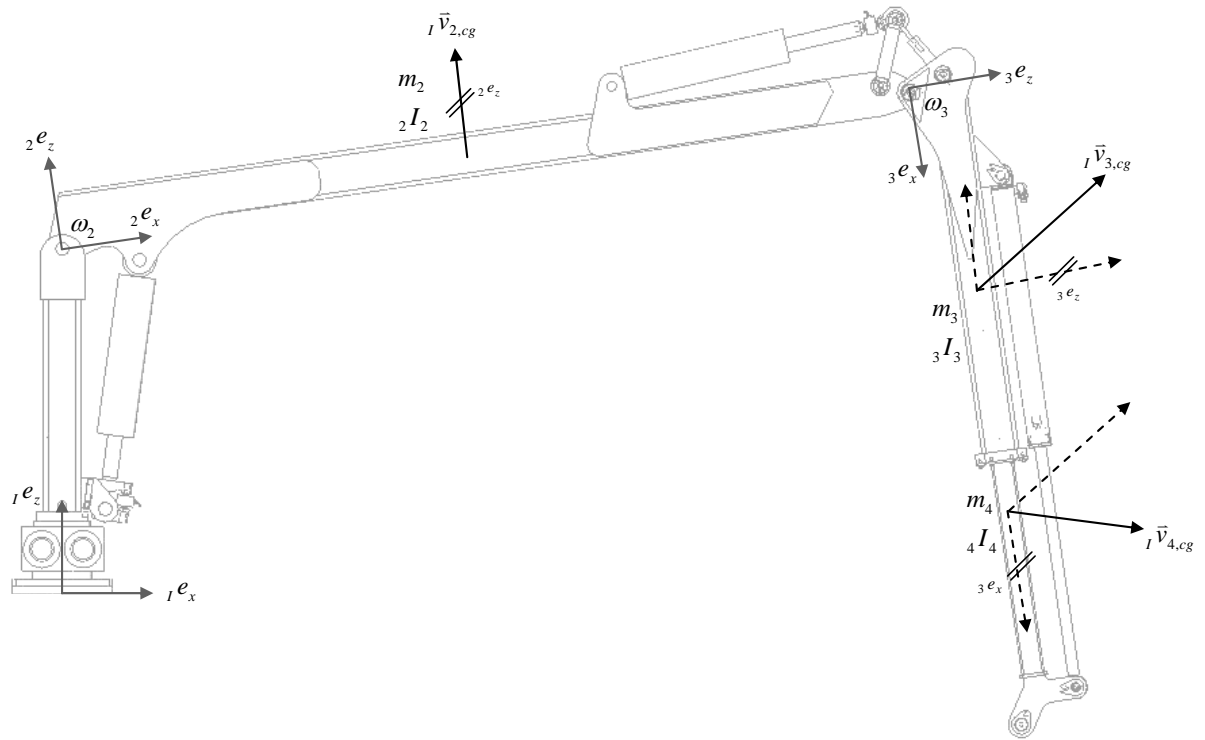


Figure 36: Evaluation of kinetic energy

As already mentioned earlier, we have simplified the dynamic crane model by reducing the mechanical parts to $n = 4$. Furthermore, the 1st link is not in motion when the crane is considered to operate in a planar frame. Thus the dynamic formulation takes three links into account, namely the 2nd, the 3rd and the telescopic link. The mass as well as the inertia tensor of each link is given in the appendix.

We will now focus on the unknown quantities of equation 45 that have to be determined. In this regard, the linear and angular velocities of the respective centers of gravity must be given as a function of the generalized coordinates. For this purpose, both velocities are expressed in terms of the Jacobian matrix that represents the contribution of the joint variables to the velocity of a single link i :

$$v_i = J_{v_i, cg}(q) \cdot \dot{q} \quad (46)$$

$$\omega_i = J_{\omega_i}(q) \cdot \dot{q}, \quad (47)$$

where $J_{v_i, cg}$ denotes the translational Jacobian of the center of gravity and J_{ω_i} the rotational Jacobian respectively. Notice, that the translatory velocity is only dependent on the joint variables and is not time-dependent which follows that $\frac{\partial \bar{r}}{\partial t} = 0$.

The Jacobian matrix can be obtained by a partial derivation of a vector with respect to the generalized coordinates. In our case, the Jacobian matrices are determined by:

$$J_{v_i, cg}(q) = \frac{\partial {}_I \bar{r}_{i, cg}}{\partial q} \quad (48)$$

$$J_{\omega_i}(q) = \frac{\partial {}_I \omega_i}{\partial \dot{q}}. \quad (49)$$

Replacing equations 46 and 47 in equation 56 yields in

$$T = \frac{1}{2} \dot{q}^T \left[\sum_{i=2}^n \left(J_{v_i, cg}(q)^T m_i J_{v_i, cg}(q) + J_{\omega_i}(q)^T A_{i i} I_{i i} A_i^T J_{\omega_i}(q) \right) \right] \dot{q} \quad (50)$$

3.2.3 Potential energy

The crane is assumed to consist of rigid bodies with no joint flexibility. Thus the potential energy that is stored in the system happens to come up only due to gravitational forces. It can be expressed by assuming that the mass of each link is concentrated at its center of gravity:

$$V = mg^T {}_I \bar{r}_{cg}, \quad (51)$$

where g is the gravity acceleration vector and ${}_I \bar{r}_{cg}$ the vector of the centers of mass in the inertial frame associated to q .

The total potential energy of the crane manipulator is then given by

$$V = \sum_{i=2}^n m_i g^T {}_I \bar{r}_{i, cg}(q), \quad (52)$$

where ${}_I \bar{r}_{i, cg}$ has been derived in chapter 3.1.2 and the mass of each link can be found in the appendix.

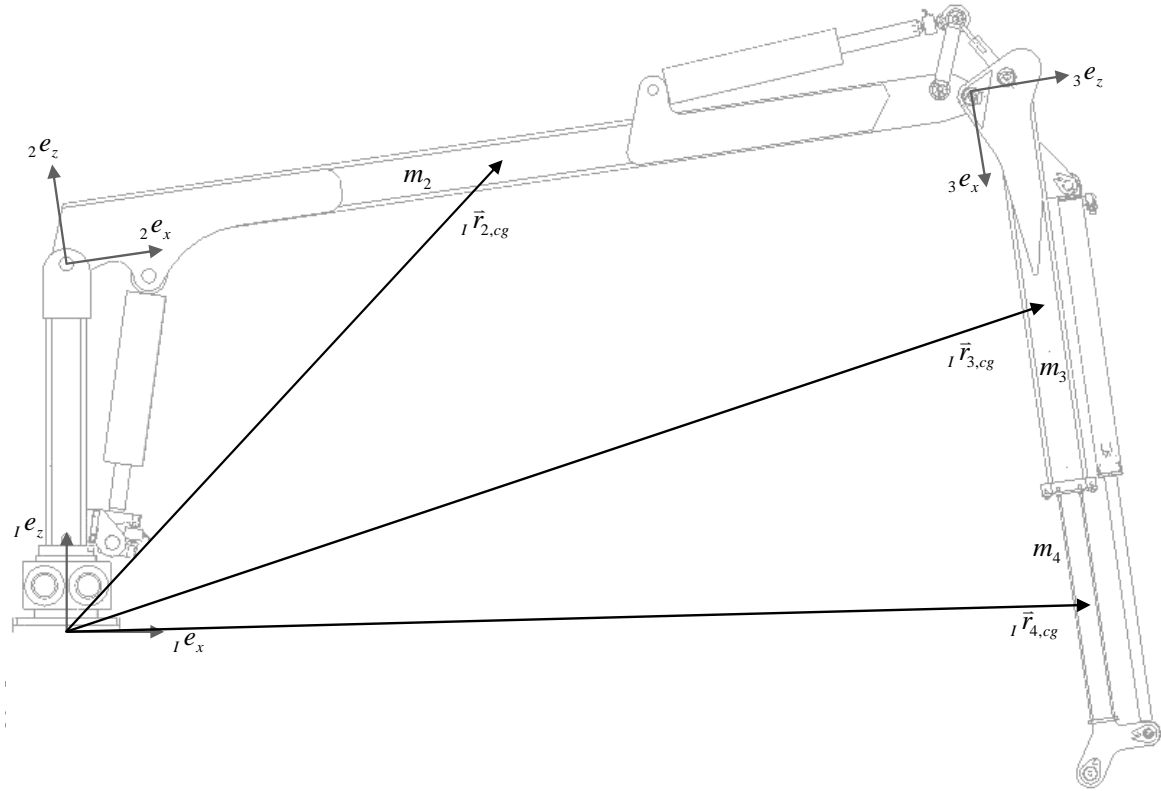


Figure 37: Evaluation of potential energy

3.2.4 Generalized forces

The generalized force vector Q represents the applied forces in the constraints of the bodies that are not covered by equation 50 and 52. The goal of this section is to formulate a set of forces associated to the generalized coordinates q .

By separating the three cylinder actuators from the mechanical parts of the crane, the resulting cylinder force can be seen as an external force that acts onto the crane parts. According to this, there are in total six cylinder forces that are introduced to the links ($m = 6$). The generalized forces can then be formulated as

$$Q = \sum_{j=1}^m \left(\left(\frac{\partial {}_I \bar{r}_{j,f}(q)}{\partial q} \right)^T {}_I f_j \right), \quad (53)$$

where ${}_I f_j$ terms the force vector related to the inertial frame and ${}_I \bar{r}_{j,f}(q)$ denotes the point of force application.

We can further derive the velocity Jacobian $J_{v_j,f}(q)$ in the same fashion, as done in equation 48, which yields in

$$Q = \sum_{j=1}^m \left({}_I f_j^T J_{v_j,f}(q) \right). \quad (54)$$

Figure 38 sketches the cylinder forces f_m and the respective vectors to the points of force application:

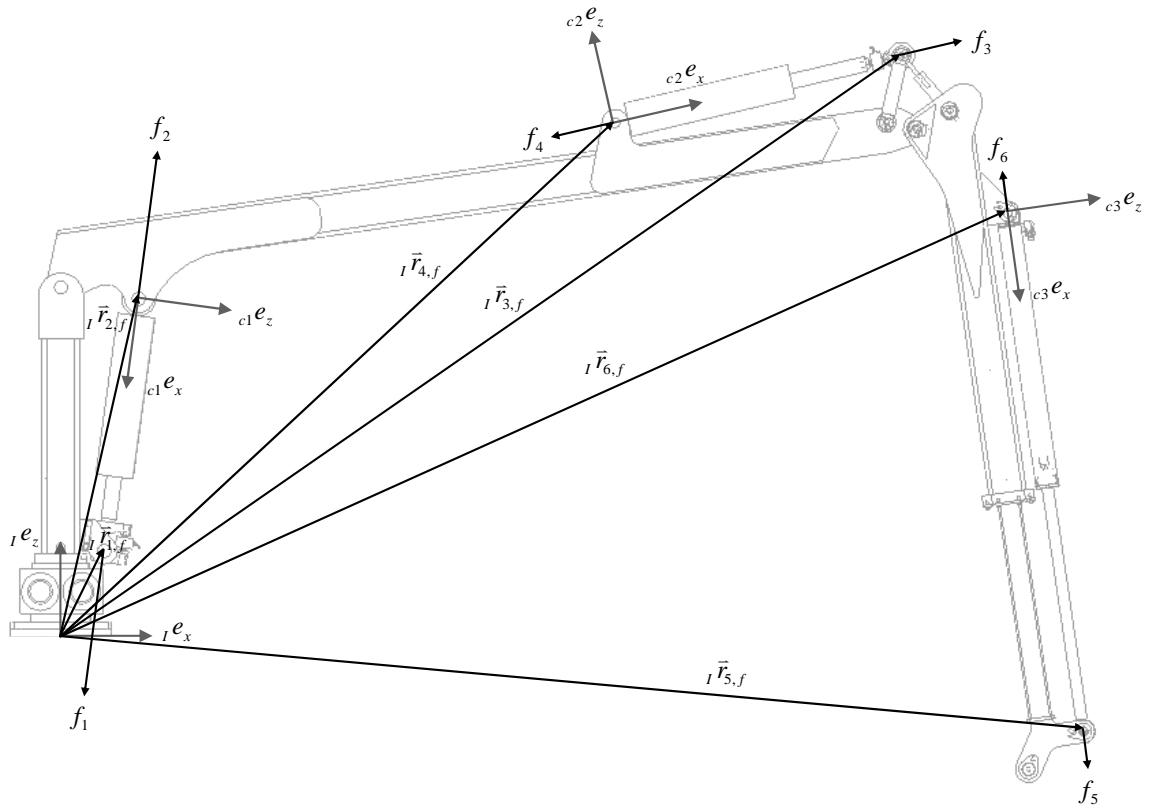


Figure 38: Evaluation of generalized forces

One should keep in mind that the transmitted actuator force f_j is aligned between two bodies and thus corresponds to a spring-damping phenomenon. Anyhow, we will not consider a spring-damping behaviour of two bodies in contact. Instead we assume that the generalized force is expressed solely in terms of the resulting cylinder force, caused by the differential pressure of the adjacent cylinder chambers. The detailed determination of the cylinder forces will be separately addressed in chapter 4.2.

3.2.5 Equations of motion

As mentioned in the beginning of this chapter, the Euler-Lagrange equation can be written in terms of the system's total kinetic and potential energy. We replace equation 43 in equation 44, which gives us

$$\frac{d}{dt} \frac{\partial (T(q, \dot{q}) - V(q))}{\partial \dot{q}} - \frac{\partial (T(q, \dot{q}) - V(q))}{\partial q} = Q^T. \quad (55)$$

We begin with the computation of the 1st term of the equation's left hand side. In the latter section, we have computed V as a function of the generalized coordinates q only, and

therefore the following holds:

$$\frac{\partial (V(q))}{\partial \dot{q}} = 0 \quad (56)$$

It is then obvious that after applying the distributive law, equation 55 yields in

$$\frac{d}{dt} \left(\frac{\partial T(q, \dot{q})}{\partial \dot{q}} \right) - \left(\frac{\partial T(q, \dot{q})}{\partial q} \right) + \left(\frac{\partial V(q)}{\partial q} \right) = Q^T. \quad (57)$$

According to [10] one can also substitute the time derivative for the partial derivative related to q which gives us

$$\frac{\partial}{\partial \dot{q}} \left(\frac{\partial T(q, \dot{q})}{\partial \dot{q}} \right)^T \ddot{q} + \frac{\partial}{\partial q} \left(\frac{\partial T(q, \dot{q})}{\partial \dot{q}} \right)^T \dot{q} + \frac{\partial}{\partial t} \left(\frac{\partial T(q, \dot{q})}{\partial \dot{q}} \right)^T - \left(\frac{\partial T(q, \dot{q})}{\partial q} \right)^T + \left(\frac{\partial V(q)}{\partial q} \right)^T = Q. \quad (58)$$

Finally, we define the $n \times n$ mass matrix

$$M(q) = \frac{\partial}{\partial \dot{q}} \left(\frac{\partial T(q, \dot{q})}{\partial \dot{q}} \right)^T, \quad (59)$$

and the vector of gyroscopic and active forces

$$h(q, \dot{q}) = -\frac{\partial}{\partial q} \left(\frac{\partial T(q, \dot{q})}{\partial \dot{q}} \right)^T \dot{q} - \frac{\partial}{\partial t} \left(\frac{\partial T(q, \dot{q})}{\partial \dot{q}} \right)^T + \left(\frac{\partial T(q, \dot{q})}{\partial q} \right)^T - \left(\frac{\partial V(q)}{\partial q} \right)^T + Q \quad (60)$$

for replacing them in equation 58 which yields in:

$$M(q) \ddot{q} - h(q, \dot{q}) = 0 \quad (61)$$

Rewriting equation 61 shows that

$$\ddot{q} = M(q)^{-1} h(q, \dot{q}) \quad (62)$$

which allows us to define our first state space set of the mechanical system:

$$\begin{bmatrix} \dot{y}_1 \\ \dot{y}_2 \end{bmatrix} = \begin{bmatrix} y_2 \\ \ddot{q} \end{bmatrix}, \text{ with } y_{12} = [y_1 \ y_2]^T \quad (63)$$

4 Hydraulic model

In this chapter we will derive a non-linear model of the hydraulic system that is connected to the laboratory crane. A hydraulic system consists of hydraulic cylinders, a hydraulic pump, hoses between the different units and valves for controlling the hydraulic flow. This work will not specifically regard the hydraulics of the pump, but it has been a major topic of ongoing works that in this concern also deals with the subject of load sensing of excavators and forestry machines [2].

As a start, the hydraulic system will be distinguished into a valve model and a cylinder model. Afterwards, both sub-systems will be combined in order to derive the non-linear state space equations of the entire hydraulic system. Finally in chapter 7, the derived equations are applied to a *MATLAB* environment where the overall aim is to create a suitable *m-file* that captures the dynamic model of the crane.

4.1 Mathematical model of the spool valve

The valve block represents the main control unit of the crane. It is made up of six proportional directional valves including a spool and two return springs at each end. The following section describes a static valve model and will further expound the valve dynamics in order to derive the equations of motion. In this regard, we will also consider the critical flow through the valves and thus distinguish between laminar and turbulent flow.

4.1.1 Static model of the spool valve

4.1.1.1 Valve configuration

The valves that are used for controlling the double-acting hydraulic cylinders are solely 4/3-valves, that is, four ways and three positions. Thus, there are two incoming ports (pump supply and return tank) and two outgoing ports (A and B) connected to the valve (see Figure 39).

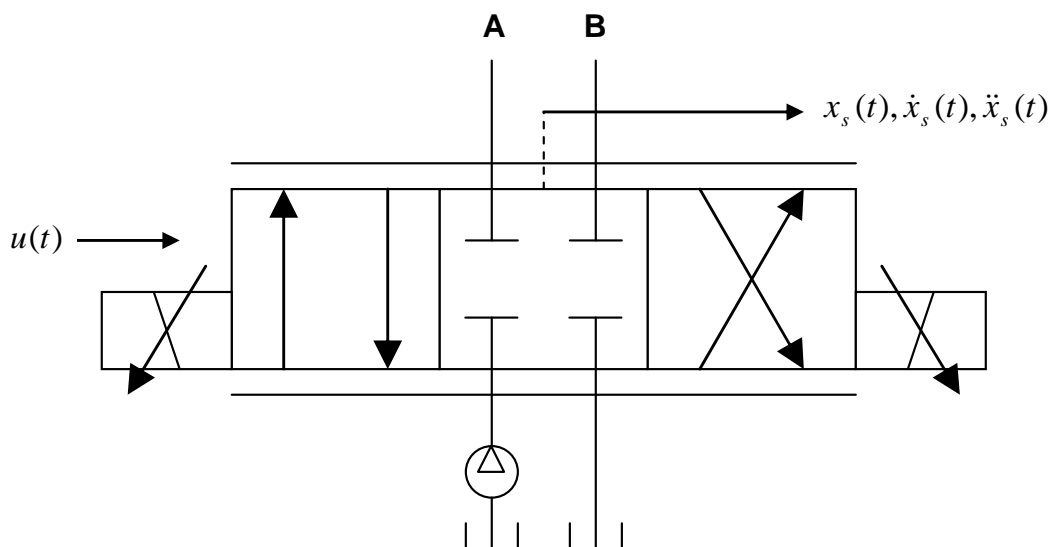


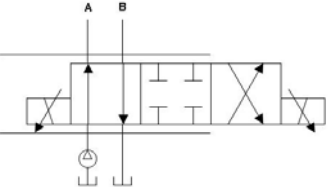
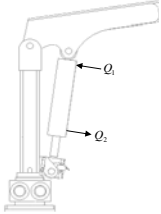
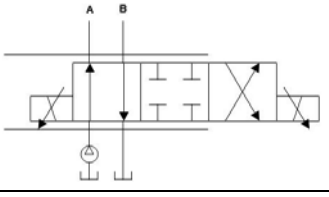
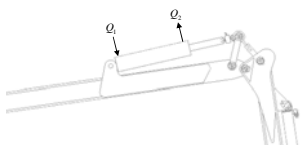
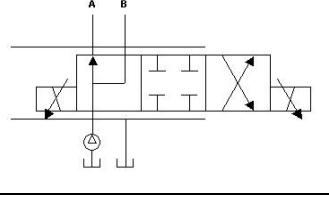
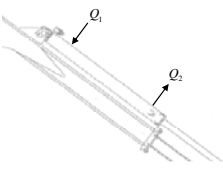
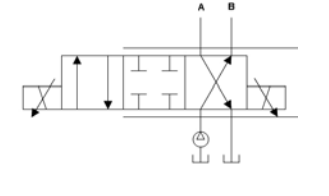
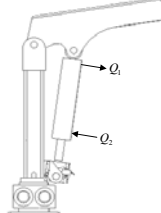
Figure 39: Sketch of a 4/3 valve

One should bear in mind that port A is always connected to cylinder chamber 1 (blind-end side), whereas port B is linked with cylinder chamber 2 (rod-end side).

The spool's position can be regulated such as the supply port is connected to either port A ($x_s > 0$) or port B ($x_s < 0$). The intermediate position ($x_s = 0$, sketched in Figure 39) is to freeze the cylinder piston, where all the valve flow through the ports is stopped immediately. A spring is used at both ends of the spool in order to force the spool back into its initial position. This will cause a flow stop when the coil is not energized.

The sixth valve, which controls the flow to the cylinder of the telescopic beam, is slightly different compared to the other valves, as it is a so-called regenerative valve. During the extraction movement, ports A and B are then both connected to the supply port. From this it follows, that the pressures in chamber A and chamber B are nearly the same and the piston will only move due to the larger cross-sectional area of the cylinder's blind-end chamber (A). The resulting cylinder force ($F = pA_{rod}$) then determines the piston velocity and will push the oil from the rod-end of the cylinder (chamber B) back into chamber A. As a conclusion, a regenerative valve gives rise to rapid extractions with less oil consumption.

The several valve configurations and their system responses are sketched in Table 2:

Spool position x_s	Valve nr. / Cylinder nr. ³	Cylinder response	Joint variable
	2 / 1		$\ddot{\alpha} \uparrow$
	3 / 2		$\ddot{\beta} \downarrow$
	6 / 3		$\ddot{x}_3 \uparrow$
	2 / 1		$\ddot{\alpha} \downarrow$

³ Valve nr.1 is used in order to control the rotary joint located at link 1 which is not discussed in this work due to a planar model. Besides, valve nr.4 and nr.5 are not in use.

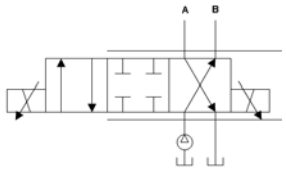
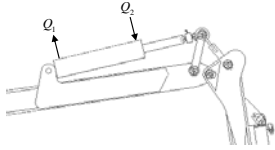
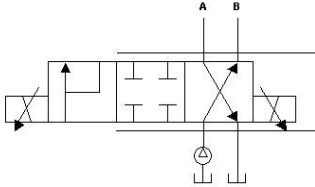
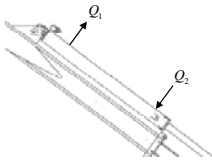
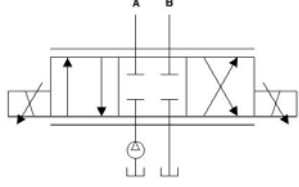
Spool position x_s	Valve nr. / Cylinder nr.	Cylinder response	Joint variable
	3 / 2		$\ddot{\beta} \uparrow$
	6 / 3		$\ddot{x}_3 \downarrow$
	2 / 1 3 / 2 6 / 3	no valve flow	$\ddot{\alpha} = 0$ $\ddot{\beta} = 0$ $\ddot{x}_3 = 0$

Table 2: Flow response of different valve configurations

4.1.1.2 Working principle

Generally the crane valves are controlled electronically, that is by solenoid-operated devices such as coils. However, the valve block of the laboratory crane is equipped with certain kind of pre-valves in addition to the main valve so that its working principle can be explained as follows:

The induced magnetic field provides the transformation of an electrical signal into an electromagnetic force, which drives the spool of the pre-valve to its desired position (see Figure 40). In general there are two pre-valves controlling one main valve. One pre-valve controls the pressure at one end of the main valve, the other pre-valve at the other end. The main valve spool is centered by springs. Hence, a flow (q_A' , q_B') is caused into the main valve chamber and generates a pressure at the spool ends, meaning that the position of the main spool x_s is thereby hydraulically operated. From the spool displacement it follows that a flow is generated through the valve port caused by the supply pressure p_s and the tank pressure p_0 . The output flows of the valve (q_A , q_B) then vary the pressures in both cylinder chambers.

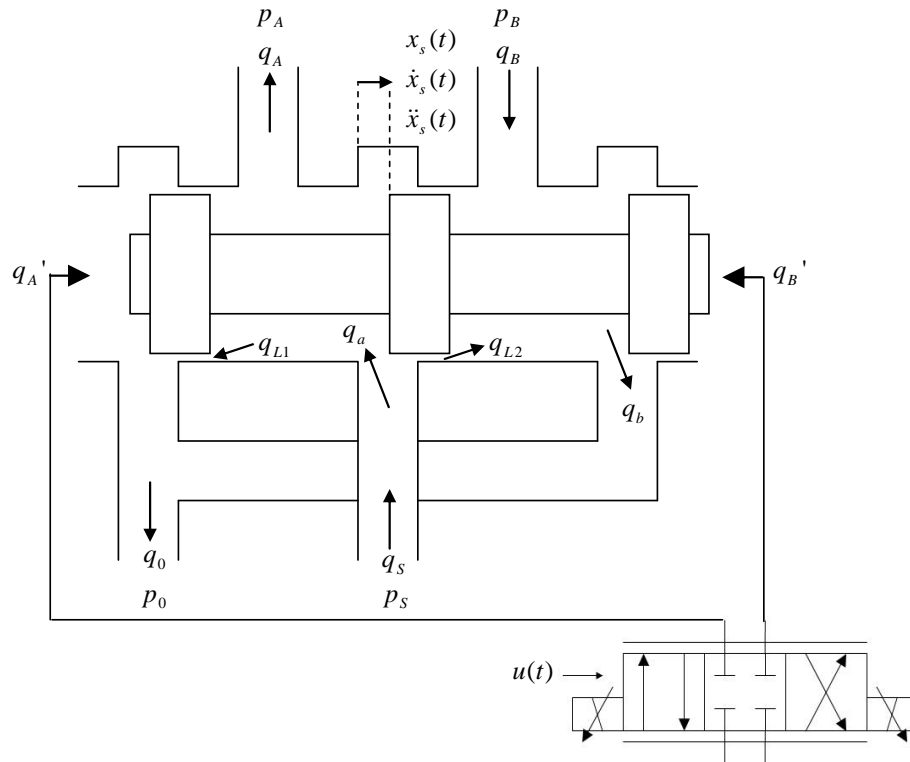


Figure 40: Orifice flows of a 4/3-valve

The main valve of the crane is a so called flow valve. It is constructed to give an oil flow to the valve that is proportional to the control signal. The differential oil pressure across the main valve is kept constant, in our case it is kept to eight bars. The constant pressure across the valve makes the flow to be dependent only of the main spool position.

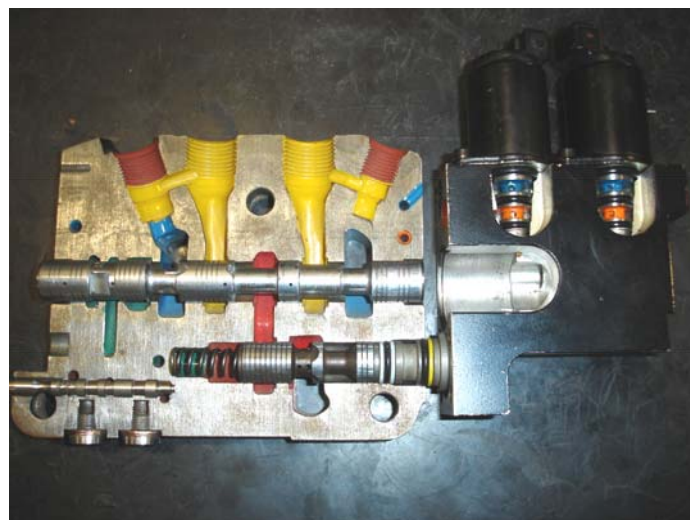


Figure 41: Valve spool block (Parker)

In Figure 41 a valve block from *Parker Fluid Control Division* is shown. The pre-valve spools are located at the right-hand side whereas the main valve spool is the silver rod in the middle. On the lower right, one can notice the spool of the pre-valve controlling the differential pressure. The lower left valve is used for load sensing. This is because the load-induced

pressure downstream of an orifice is sensed and pump flow is adjusted to maintain a constant pressure drop (and therefore flow) across the orifice. The red channels are for pressurized oil and the blue ones indicate the oil that flows back to the tank. The yellow ones are the channels to the chambers of the cylinder. The green channel is controlling the oil pressure across the main valve.

The pump that is connected to the valves of the laboratory crane is assumed to produce a constant pressure. When operating the crane, the pump is adjusted to a supply pressure of $p_s = 140$ bar. It also seems reasonable that the tank pressure p_0 can be put on an atmosphere pressure level, as the fluid must be allowed to flow freely back into the tank. The experimental setup for friction evaluation (see chapter 5) also includes a separate hydraulic cylinder controlled by a traditional industrial proportional control valve.

4.1.1.3 Flow equations

Hydraulic flows can arise when a restriction causes a pressure drop between adjacent spatiality. In Figure 40 one could identify that the shifted spool determines the restriction size of the cross-section areas of supply and return port. Consequently q_A and q_B can be seen as restriction flows, that are functions of the spool position and the local pressure difference at the orifice.

The flow through a restriction is generally turbulent and then happens to be proportional to the squared root of the pressure drop:

$$q = C_0 x_s \sqrt{\Delta p} \quad (64)$$

In practice there is some loss of energy at the orifices that can be considered in terms of a constant discharge coefficient C_0 :

$$C_0 = \frac{Q_N}{x_{s,\max} \sqrt{\frac{\Delta p_N}{2}}} \quad (65)$$

where Q_N is the nominal flow and Δp_N the nominal pressure drop respectively. Both quantities are based on static valve characteristics that are provided in data sheets.

When applying equation 64 to the valves of the laboratory crane, the orifice flows yield in

$$q_{tur,A} = C_0 x_s \operatorname{sgn}(p_S - p_A) \sqrt{|p_S - p_A|} \quad (66)$$

$$q_{tur,B} = C_0 x_s \operatorname{sgn}(p_B - p_0) \sqrt{|p_B - p_0|} \text{ for } x_s > 0, \text{ and}$$

$$q_{tur,A} = C_0 x_s \operatorname{sgn}(p_A - p_0) \sqrt{|p_A - p_0|} \quad (67)$$

$$q_{tur,B} = C_0 x_s \operatorname{sgn}(p_S - p_B) \sqrt{|p_S - p_B|} \text{ for } x_s < 0 \text{ respectively.}$$

One should keep in mind, that equation 66 changes when using the regenerative valve of the 3rd cylinder. In this case the flow from port B becomes

$$q_{tur,B} = C_0 x_s \operatorname{sgn}(p_B - p_S) \sqrt{|p_B - p_S|}. \quad (68)$$

Laminar flow can arise when the restriction at the orifice is fairly narrow, for example in the origin of an opening process. Then the flow happens to become directly proportional to the pressure drop and hence equations 66 and 67 change to:

$$q_{lam,A} = C_0 x_s (p_S - p_A) \left(\frac{|p_S - p_A|}{p_{tr}} \right) \quad (69)$$

$$q_{lam,B} = C_0 x_s (p_B - p_0) \left(\frac{|p_B - p_0|}{p_{tr}} \right) \text{ for } x_s > 0, \text{ and}$$

$$q_{lam,A} = C_0 x_s (p_A - p_0) \left(\frac{|p_A - p_0|}{p_{tr}} \right) \quad (70)$$

$$q_{lam,B} = C_0 x_s (p_S - p_B) \left(\frac{|p_S - p_B|}{p_{tr}} \right) \text{ for } x_s < 0 \text{ respectively.}$$

According to [1] the transition region at which the flow turns from a laminar to a turbulent state can be estimated in terms of the transition pressure

$$p_{tr} = \left(\frac{3 \operatorname{Re}_{tr}^2 \nu}{4 C_0} \right)^2, \quad (71)$$

where Re_{tr} is the threshold for the Reynolds number and ν is the kinematic viscosity of the fluid.

The flow is assumed to be laminar when the pressure drop is below transition pressure. The Reynolds number then indicates the point at which the flow changes to a turbulent state. In traditional hydraulic applications the critical Reynolds number is generally in the range of $2000 < \operatorname{Re}_{tr} < 3000$. Plugging Re_{tr} in equation 71, the size of the transition pressure is then in a range of approximately 2 to 4 bar. Hence, the maximum laminar flow is given at

$$q_{lam,max} = 3 C_0 x_s p_{tr}, \quad (72)$$

whereas the turbulent flow has its minimum at

$$q_{tur,min} = C_0 x_s \sqrt{p_{tr}}. \quad (73)$$

In order to achieve a smooth transition between the two flow states, we harmonize equations

66/69 and 67/70 respectively, which gives a more practical description of the flow dynamics:

$$q_{trans} = \left| \frac{\Delta p - p_{tr,min}}{p_{tr,max} - p_{tr,min}} \right| q_{tur} + \left(1 - \left| \frac{\Delta p - p_{tr,min}}{p_{tr,max} - p_{tr,min}} \right| \right) q_{lam} \cdot \quad (74)$$

where q_{trans} is the flow in the transition range $p_{tr,min} < \Delta p < p_{tr,max}$.

From the different flow equations we graph the flow's dependency on the pressure drop and the maximum spool opening in *MATLAB* and yield the chart depicted in Figure 42:

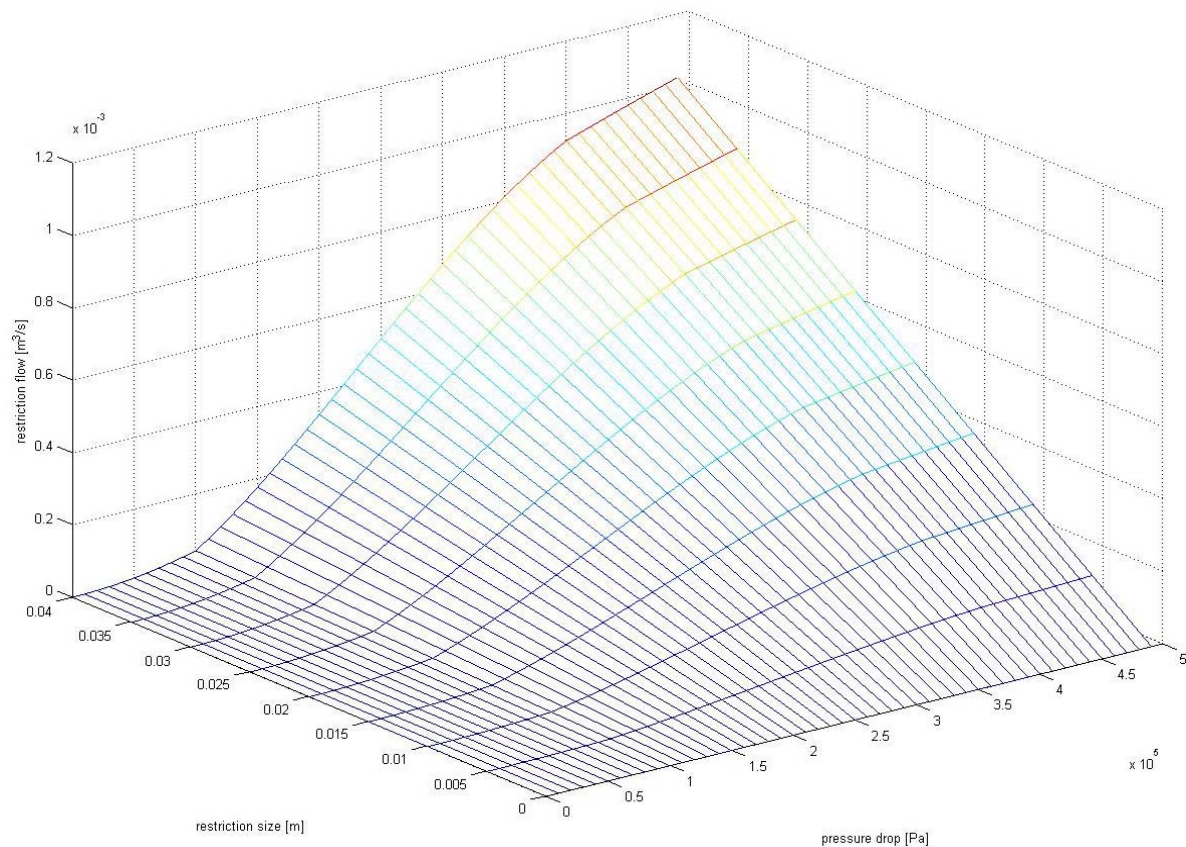


Figure 42: Restriction flow in terms of a merged laminar and turbulent flow

As one can notice in Figure 42, the laminar flow increases constantly with the pressure drop until a level of 2 bar has been reached. From 2-4 bar equation 74 takes effect until the turbulent flow dominates and thus the flow gradient decreases. In either case, the size of the restriction opening is always directly proportional to the valve flow.

Strictly speaking there is some leakage between the spool and the inner body of the valve. It follows that there has to be a flow (q_{L1} and q_{L2}) from the inner spool segment to its adjacent chambers (see Figure 40). The corresponding flow chart is given in Figure 43.

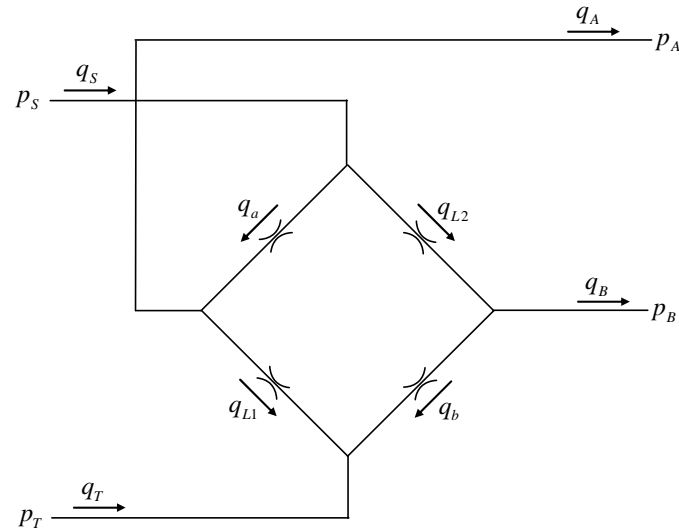


Figure 43: Restriction flows of a 4/3-valve [1]

According to Figure 43, the port flows are computed in the following manner:

$$\begin{aligned}
 q_A &= q_a(x_s, p_S, p_A) - q_{L1}(x_g, p_A, p_T) \\
 q_B &= q_b(x_s, p_B, p_T) - q_{L2}(x_g, p_S, p_B) \\
 q_S &= q_a(x_s, p_S, p_A) + q_{L2}(x_g, p_S, p_B) \\
 q_0 &= q_b(x_s, p_A, p_T) + q_{L1}(x_g, p_B, p_T)
 \end{aligned} \tag{75}$$

We notice that the leakage flow is a function of the gap size x_g between the spool and the valve frame. In general, the gap size is almost minuscule which follows that the leakage flow is innately low. However, when using a spool configuration that overlaps the ports, leakage can be further reduced primarily in the non-energized mode. As a matter of negligible leakage flow and also in order to keep the equations manageable, we will subsequently not include the leakage effect of the valves to the hydraulic model.

4.1.2 Dynamics of the spool valve

The dynamic spool model is an essential part when designing control devices. We have learned that the spool position is the main control input to the static system and therefore it will be represented in a linear function of the control input.

Before we start to model the spool dynamics, the following assumptions are made in order to keep the equations of motion rather straightforward:

- *The leakage flow, derived in the previous chapter is negligible and will consequently not be considered in the dynamic model*
- *The complex behaviour of the hydraulically operated spool will be simplified and described by a solenoid operated spool*

- Inside the hydraulic hose, there is no pressure drop. However, the rise in pressure at the cylinder connectors is taken into account specially.

- The pump supplies the valves with a steadily constant pressure whereas the tank pressure is put on a level of atmosphere pressure.

- Hydraulic friction inside of the hoses will be neglected

The dynamic of a spool valve follows approximately a linear differential equation of second order described in equation 76:

$$m \frac{dx_s^2(t)}{dt^2} + c \frac{dx_s(t)}{dt} + kx_s(t) = F, \quad (76)$$

where m is the mass of the spool, c the damping factor and k the spring stiffness. The force F can be seen as an input to the system, e.g. the input current to the valves.

By substituting $k = m\omega_n^2$ and $c = 2\zeta\sqrt{km}$ equation 76 becomes

$$\frac{dx_s^2(t)}{dt^2} + 2\omega_n\zeta \frac{dx_s(t)}{dt} + \omega_n^2 x_s(t) = \omega_n^2 u(t), [3] \quad (77)$$

where $u(t)$ is the systems control input.

The system behaviour is then sufficiently described by the two fundamental model parameters, the valve's natural frequency

$$\omega_n^2 = \sqrt{\frac{1}{\tau^2} + \omega_d^2} \quad (78)$$

and its damping ratio

$$\zeta = \frac{1}{\sqrt{1 + \tau^2 \omega_d^2}} \quad (79)$$

as functions of the time constant τ and the ringing frequency ω_d . According to [1], the parameters of a proportional control valve can be estimated with $\omega_n \approx 2 \cdot \pi \cdot 161s^{-1}$ and $\zeta \approx 0.48$.

As we notice, the right hand side of equation 77 is not equal to zero, which makes the system become inhomogeneous. That is, the term $\omega_n^2 u(t)$ can be seen as an input to the homogenous system. The action of changing the spool position is then induced by the control input $u(t)$.

With the initial conditions of the spool valve being $x_s(0) = 0$, $\dot{x}_s(0) = 0$ and $u(0) = 0$, we can apply the Laplace transform to equation 77, which results in

$$s^2 X(s) + 2\omega_n \zeta s X(s) + \omega_n^2 X(s) = \omega_n^2 U(s). \quad (80)$$

Written equation 80 as a relation between input and output finally yields in the transfer function of the form

$$G(s) = \frac{X(s)}{U(s)} = \frac{\omega_n^2}{s^2 + 2\omega_n \zeta s + \omega_n^2} = \frac{1}{\frac{1}{\omega_n^2} s^2 + \frac{2\zeta}{\omega_n} s + 1}. \quad (81)$$

The system behaviour can now be described qualitatively by the poles, namely if the denominator of the transfer function is set to zero.

From equation 81 we obtain $s_{1,2} = \omega_n(-\zeta \pm \sqrt{\zeta^2 - 1})$, which gives us three possible states for the spool behaviour, dependent on the value of ζ . Generally, the damping ratio is less than one ($\zeta < 1$) and hence we find two complex values for s . The system is under-damped and oscillates with the damped frequency $\omega_d = \omega_n \sqrt{1 - \zeta^2}$. The corresponding model is shown in the *Simulink* block in Figure 44 and will be extensively discussed in chapter 7:

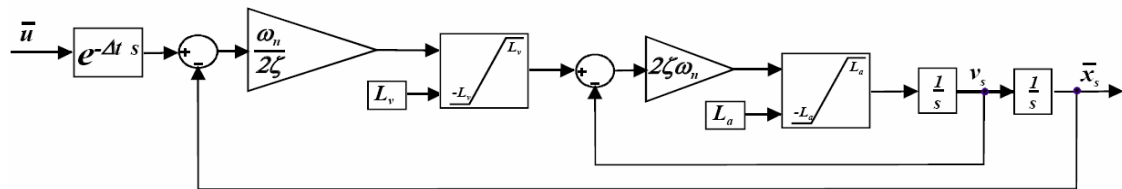


Figure 44: *Simulink* block of the spool dynamics [1]

The dynamic spool model contains two non-linearities: On the one hand, limitations in velocity L_v and acceleration L_a have to be taken into consideration. On the other hand a delay in the phase lag Δt has to be adjusted in order to match the phase of the system response.

As a last step, the mathematical model of the spool valve is represented in a state space function. By defining the state vector $y_{34} = [y_3 \ y_4]^T = [x_s \ \dot{x}_s]^T$, the state space correlation can be written in the form

$$\begin{bmatrix} \dot{y}_3 \\ \dot{y}_4 \end{bmatrix} = \begin{bmatrix} 0 & 1 \\ -\omega_n^2 & -2\zeta\omega_n \end{bmatrix} y_{34} + \begin{bmatrix} 0 \\ \omega_n^2 u(t) \end{bmatrix}. \quad (82)$$

We notice that the position of the spool, which will be the input signal for the later described cylinder model, is solely determined by the control input $u(t)$.

4.2 Mathematical model of the cylinder

In this chapter we will develop a common mathematical model of a double-acting hydraulic cylinder. As a start, a static cylinder model will be examined in order to derive the equilibrium of forces at the cylinder. In terms of formulations, these forces can then be represented in order to describe the dynamic behaviour of the cylinder.

To allow object oriented block simulation, the cylinder model includes cylinder leakage, cylinder friction and the effect of pressure drop at the cylinder connectors. The phenomenon of non-linear cylinder friction is a fairly extensive issue and will be addressed separately in chapter 5.

4.2.1 Static model of the cylinder

The aim of a static cylinder model is to find an expression of the resulting cylinder force, which can be seen as a non-potential force to the mechanical system of the crane. For this purpose we sketch a common differential cylinder that is presented in the schematic Figure 45:

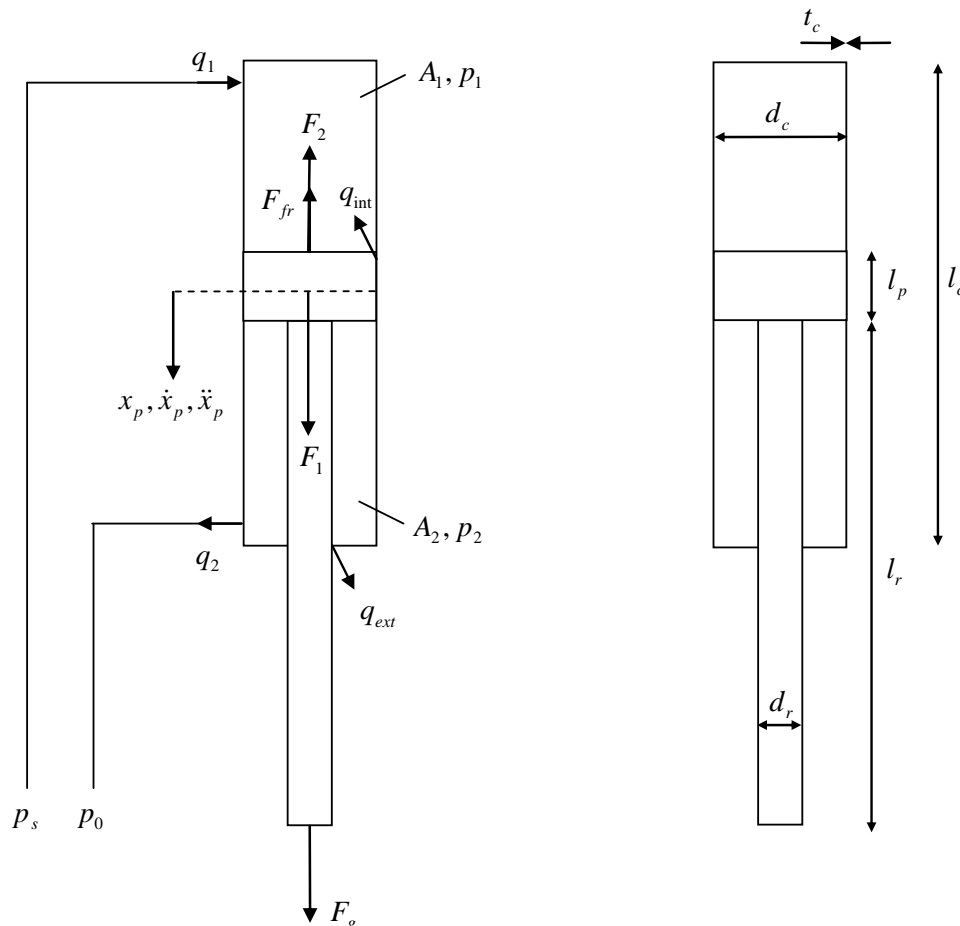


Figure 45: Schematic sketch of a double-acting cylinder

The figure on the left indicates the forces and flows at the cylinder whereas the latter's build up the equations of motion which will be derived in the following sections. The figure on the right gives the cylinder dimensions in terms of the cylinder's characteristic parameters. The exact cylinder dimensions are given in the appendix.

Basically, the resulting force of a double-acting cylinder is determined by the chamber's product difference of pressure and cross-sectional area: $p_2A_2 - p_1A_1$. According to Figure 45 our enhanced cylinder model also considers friction forces as well as Newton's second law of motion and then the following differential equation holds:

$$m\ddot{x}_p = F_1 - F_2 + F_g - F_{fr} , \quad (83)$$

where \ddot{x}_p is the piston acceleration and m is the mass of the loose parts (basically the mass of piston and rod). The force F_1 is generated by the upper chamber pressure, whereas F_2 comes from the lower chamber. F_g is the gravitational force ($m \cdot g$) and F_{fr} the friction force to solve.

As a start to the mathematical cylinder model, we begin with a geometrical approach to the model's dimensions. Let us define the initial conditions for the oil volume of both cylinder chambers as

$$V_{0,1}(x_p = 0) = \frac{l_c - l_p}{2} A_1 + V_{0,p} = \frac{l_c - l_p}{2} \frac{d_c^2 \pi}{4} + V_{0,p} \text{ and} \quad (84)$$

$$V_{0,2}(x_p = 0) = \frac{l_c - l_p}{2} A_2 + V_{0,p} = \frac{l_c - l_p}{2} \frac{(d_c^2 - d_r^2) \pi}{4} + V_{0,p} \quad (85)$$

respectively.

Notice that $V_{0,p}$ denotes the dead volume in the pre-chambers to which the hydraulic hoses are connected. The initial chamber volume is based on the initial piston position, which is the centering position of the cylinder (see 2.3.2).

The dynamic chamber volumes are then defined by

$$V_1(t) = \frac{l_c - l_p}{2} \frac{d_c^2 \pi}{4} + x_p \frac{d_c^2 \pi}{4} + V_{0,p} = \frac{(l_c - l_p + 2x_p)d_c^2 \pi}{8} + V_{0,p} \text{ and} \quad (86)$$

$$V_2(t) = \frac{l_c - l_p}{2} \frac{(d_c^2 - d_r^2) \pi}{4} - x_p \frac{(d_c^2 - d_r^2) \pi}{4} + V_{0,p} = \frac{(l_c - l_p - 2x_p)(d_c^2 - d_r^2) \pi}{8} + V_{0,p} \quad (87)$$

respectively.

4.2.2 Dynamics of the cylinder

The overall aim of chapter 4 is to derive a state space form of the cylinder dynamics. For this purpose we reapply equation 83 and after some rewriting we yield the following equation of motion:

$$\ddot{x}_p = \frac{1}{m} [(p_1 A_1 - p_2 A_2) + mg - F_{fr}] \quad (88)$$

One can observe, that the only variables in equation 88 are given by the chamber pressures p_1 and p_2 and the friction force F_{fr} . Friction evaluation will be studied extensively in chapter 5, whereas the pressure as a crucial state of the dynamic model is derived in the following section.

The mass of substances in the hydraulic system will remain constant regardless of the process that acts in the system. It holds: $\dot{V} = \sum q$. The principle of mass conservation is graphically shown in Figure 46.

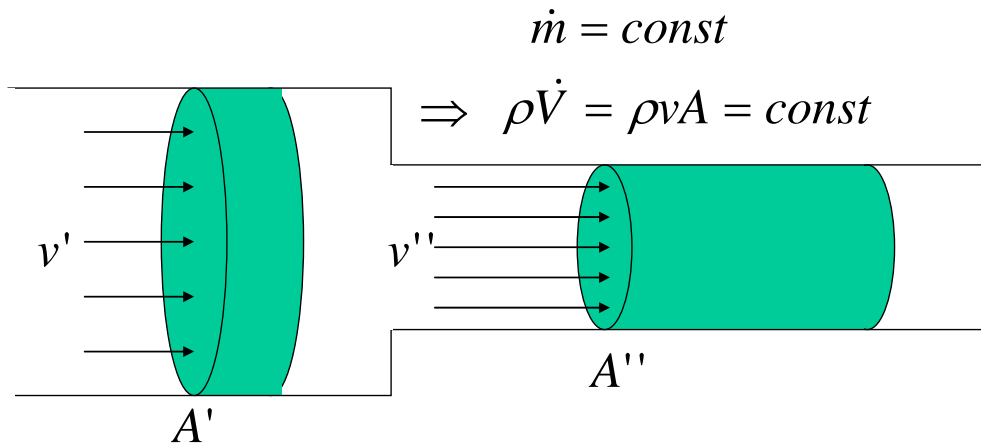


Figure 46: Conservation of mass

This conservation of a fluid mass is described in terms of the following continuity equation:

$$\dot{V}_1 = q_1 + q_{int} \Rightarrow \frac{dm_1}{dt} = \rho_{oil} (q_1 + q_{int}) \quad (89)$$

$$\dot{V}_2 = -q_2 - q_{int} - q_{ext} \Rightarrow \frac{dm_2}{dt} = -\rho_{oil} (q_2 + q_{int} + q_{ext}) \quad (90)$$

where q_{int} is the internal leakage flow between piston and cylinder frame and q_{ext} is the external leakage flow at the rod-end side of the cylinder.

One should keep in mind that q_2 becomes negative when the fluid circulates into the 2nd cylinder chamber (see Figure 45). Furthermore, the compressible fluid makes ρ_{oil} a function of the local cylinder pressures:

$$\rho_{oil}(p) = E_{oil}(p) \frac{\partial \rho_{oil}(p)}{\partial p}, \quad (91)$$

where $E_{oil}(p)$ denotes the bulk modulus of oil elasticity.

Applying $m = \rho V$ to equations 89 and 90 and replacing the derivative of oil density with equation 91, we obtain the following differential equation:

$$\frac{dp_1}{dt} \frac{V_1 \rho_{oil}}{E_{oil}} + \frac{dV_1}{dt} \rho_{oil} = \rho_{oil} (q_1 + q_{int}) \quad (92)$$

$$\frac{dp_2}{dt} \frac{V_2 \rho_{oil}}{E_{oil}} + \frac{dV_2}{dt} \rho_{oil} = -\rho_{oil} (q_2 + q_{int} + q_{ext}) \quad (93)$$

Let us rewrite the latter equations in terms of the derivative of pressure:

$$\frac{dp_1}{dt} = \frac{E_{oil}}{V_1} \left(q_1 + q_{int} - A_1 \frac{dx_p}{dt} \right) \quad (94)$$

$$\frac{dp_2}{dt} = -\frac{E_{oil}}{V_2} \left(q_2 + q_{int} + q_{ext} - A_2 \frac{dx_p}{dt} \right) \quad (95)$$

Hence, we have determined the rate of change in pressure, which can later be used as a state derivative to the dynamic model. Notice, that the time derivation of the overall chamber volume yields merely in $A_1 \frac{dx_p}{dt}$ and $-A_2 \frac{dx_p}{dt}$, respectively.

We now focus on the unknown parameters of the equations 94 and 95. According to [3], the heuristically obtained formula for the bulk modulus of oil elasticity can be written in the form

$$E_{oil}(p) = \frac{1}{2} E_{oil,max} \log_{10} \left(C_1 \frac{p}{p_{max}} + C_2 \right), \quad (96)$$

where $E_{oil,max}$ denotes the magnitude at maximum oil compressibility and p_{max} the maximum system pressure respectively. The oil constants C_1 and C_2 have been determined earlier in [6] as $C_1 = 90$ and $C_2 = 3$.

There are two possible leakage phenomena when operating a hydraulic cylinder. An internal leakage flow q_{int} arises at the restriction of the piston and the inner cylinder body. An external leakage flow q_{ext} appears at the opening for the rod-outlet. In both cases, the leakage can be seen as a flow through an infinitesimal restriction. Thus, the flow happens to be laminar so that it becomes directly proportional to the pressure difference between the mediums:

$$Q_{int} = k_{int}(p_2 - p_1) \quad (97)$$

$$Q_{ext} = k_{ext}(p_2 - p_0) \quad (98)$$

According to [3] the coefficients k_{int} and k_{ext} can be evaluated by means of the general leakage equation

$$k = \frac{\left(\frac{d_i}{2} + r_c\right)}{6\mu L} r_c^3 \pi, \quad (99)$$

where d_i denotes the inner diameter of the bore hole, r_c the radius of the shaft, μ the static friction coefficient and L the length of the restriction.

It is obvious that the leakage flow tends to zero when using appropriate gaskets inside of the cylinder. Nevertheless, we include the leakage flow to our model although the friction coefficient μ has to be estimated without experimental identification. It is also important to notice, that the pressure sensors of the cylinders are located in a pre-chamber to which the hydraulic hose is connected. The diameters of pre-chamber and hose are approximately the same, but they differ from the diameter of the main cylinder chamber. Consequently the pressure inside of the cylinder may vary compared to the measured sensor value. This effect can be represented by Bernoulli's principle:

$$\left(\frac{v}{2}\right)^2 + \frac{p}{\rho} = const \quad (100)$$

This formula states that an increase in velocity occurs simultaneously with a decrease in pressure.

It is obvious that the motion of the piston v_p determines the fluid velocity inside the cylinder chamber. The change in velocity is then given by differing diameters of hydraulic hose and cylinder chamber and can be captured with the continuity equation for the mass flows ($\dot{m} = const$)

$$\frac{A_h v_h}{\rho_{oil}} = \frac{A_c v_p}{\rho_{oil}}, \quad (101)$$

where A_h is the cross-sectional area of the hose and A_c the cross-sectional area of the cylinder respectively.

Assuming that the oil density remains constant, the velocity in the connection region changes to

$$v_h = \frac{A_c}{A_h} v_p. \quad (102)$$

Replacing equation 102 in Bernoulli's formula, the cylinder pressure yields in

$$p_c = \rho_{oil} \frac{v_p}{2} \left[\left(\frac{A_c}{A_h} \right)^2 - 1 \right] + p_h. \quad (103)$$

With a maximum piston velocity of $v_p = 0.5 \frac{m}{s}$ and an approximate oil density of

$\rho_{oil} = 1000 \frac{kg}{m^3}$, the maximum pressure rise is given as a function of the diameters only:

$$\Delta p = 250 Pa \cdot \left[\left(\frac{d_c}{d_h} \right)^4 - 1 \right] \quad (104)$$

A maximum diameter ratio of $d_c/d_h = 10$ at the blind-end side for example leads to a rise in pressure of $\Delta p_{max} \approx 25 \text{ bar}$. It seems absolutely vital that the derived pressure variation should be taken into account when designing control models of the crane. In this regard, we have to consider the increase of pressure in the flow equations 66 - 70 and add the pressure difference of equation 104 to p_A and p_B respectively.

Now, having derived a set of differential equations, we formulate a state space equation of the cylinder hydraulics. To do so, we create the state vector $y_{56} = [y_5 \ y_6]^T = [p_1 \ p_2]^T$, which includes both chamber pressures of the cylinder. Finally we equal y_{56} and equations 94 and 95 as representing the time derivatives of the state vector and obtain the following state space form of the cylinder hydraulics:

$$\dot{y}_5 = \frac{E_{oil}}{V_1} \left(q_1 + q_{int} - A_1 \frac{dx_p}{dt} \right) \quad (105)$$

$$\dot{y}_6 = -\frac{E_{oil}}{V_2} \left(q_2 + q_{int} + q_{ext} - A_2 \frac{dx_p}{dt} \right) \quad (106)$$

At this point we do not explicitly insert the flows that have been derived in chapter 4.1 into the state space form. The case differentiation of the spool valve would end up in a rather extensive formulation of the state space equations. However, one should bear in mind that it can be easily done when it comes to model the hydraulic system in *MATLAB*.

5 Modelling of hydraulic friction

Friction is a non-linear phenomenon that occurs in all kind of mechanical systems, e.g. in bearings, transmissions, cylinder actuators and valves. It is well known that friction is one of the major limitations to achieve good performance of robotic systems. It causes the performance to deteriorate and leads to steady-state errors in position regulation and tracking lags. In general, friction is difficult to describe analytically. There have been different sophisticated models proposed that capture the friction phenomenon, beginning with a classical static friction map to the description of a dynamic model.

This work will focus on several types of friction models that are essential to evaluate the friction in hydraulic cylinders rather precisely. We will briefly expose the physical effect of hydraulic friction and describe the basic idea of static friction modelling. Hereby, the unknown static parameters are estimated through open-loop experiments on the basis of friction maps between velocity and friction force. However, it appears that this classical model is unable to reflect some of the behaviours that are experimentally observed. Therefore we will illustrate an accurate model that captures the internal cylinder dynamics and in this concern also examines the bristle deflection of lubricants. This derived model is vital for describing the friction force at zero velocity and thus seems suitable for the design of model-based friction compensation.

5.1 Friction phenomena

In a classical sense, friction is the tangential force that opposes the motion of two bodies in contact. The main working principle of friction can be explained by microscopic bonding of the surfaces, which generates intermolecular forces as sketched in Figure 47.

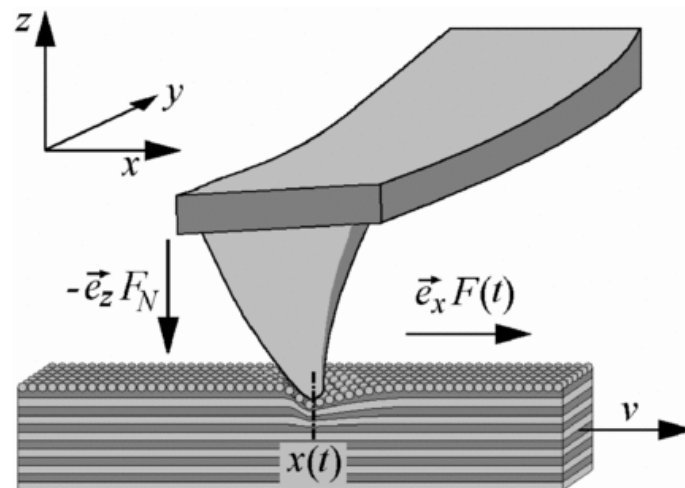


Figure 47: Microscopic approach to friction force [13]

Physically friction can be regarded as a result of several mechanisms that depend on the properties of the bodies, lubrication, wear, temperature variation and velocity of the motion. In the following hydraulic cylinder friction is explained by means of different friction phenomena that each takes care of certain friction aspects, namely static friction, Coulomb friction and viscous friction.

Since the magnitude of friction is mainly independent of the direction of motion, friction often holds a symmetric behaviour related to the magnitude of velocity. As a result, the friction

curves in the following section are mirrored in the origin of the coordinate frame. Nevertheless, when estimating the cylinder friction, we will run open-loop experiments in both directions to examine the friction's dependency on the sign of velocity. For the compensation model, however, we facilitate the model and define the mean value of the evaluated parameters as being the nominal friction parameters.

5.1.1 Static friction model

5.1.1.1 Coulomb friction

In general, friction is the force that is exerted in the opposite direction to the motion of a body whose surface is in contact with another body. The basic idea of friction during motions is that the force is proportional to the normal force F_N and thus it is not affected by the contact area or the magnitude of velocity v :

$$F_C = \mu F_N \text{sign}(v) \text{ for } v \neq 0, \quad (107)$$

where μ is the friction coefficient of the contacting materials.

The friction approximation in equation 107 is termed Coulomb friction and is a function of the sign of velocity as graphed in Figure 48:

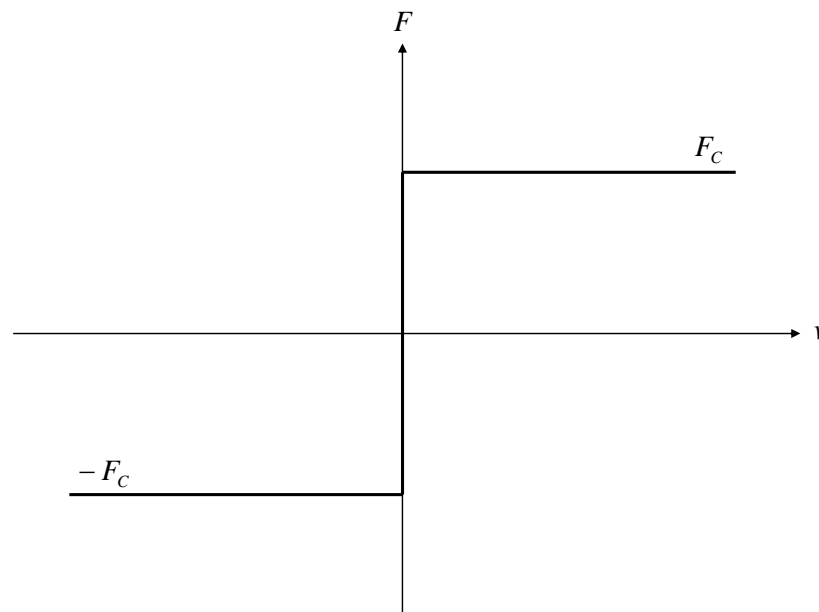


Figure 48: Coulomb friction

One should notice that Coulomb friction represents an ideal model in which the friction force is not defined for zero velocity. Is the motion at rest, the friction force can take on any value in the interval between $-F_C$ and $+F_C$ as the friction is exactly the force that keeps an object from moving.

5.1.1.2 Viscous friction

Although the Coulomb model is an adequate representation of many friction compensators, the viscosity of lubricants has to be taken into account when the system is determined by rapid changes in the velocity. The friction force is then additionally determined by the fluid's internal resistance to flow, which is a result of the shear forces in the fluid layer that increase with velocity. The resulting force is denoted as viscous friction:

$$F_v = k_v |v|^{\delta_v} \text{sign}(v), \quad (108)$$

where k_v is the viscous friction coefficient and δ_v is the gradient that describes the non-linear dependence on the velocity.

Primarily the coefficient δ_v is specified by the geometry of the application. In our case experimental evaluations have shown that the friction force is consistent to the analytical model with an coefficient of $\delta_v \approx 1.5$. The corresponding gradient of viscous friction is depicted in Figure 49:

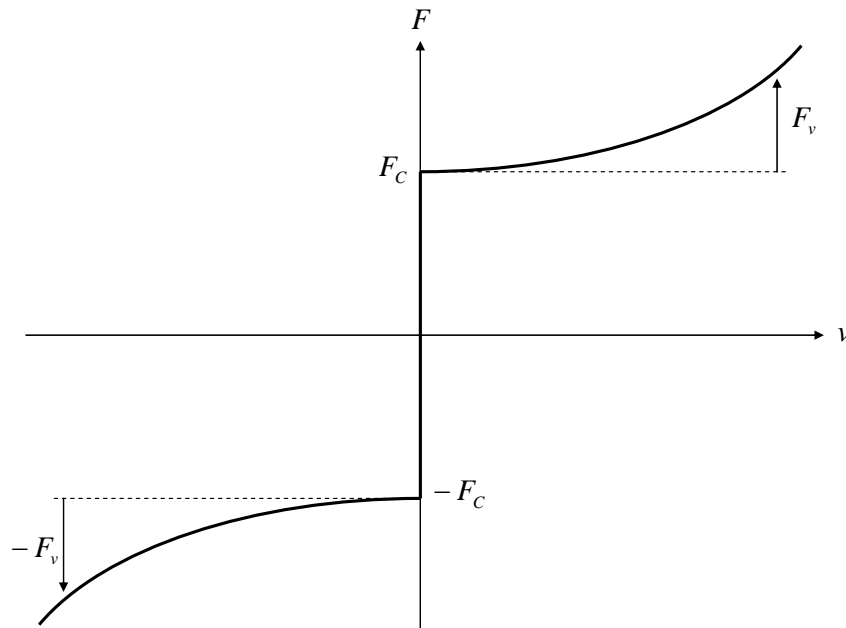


Figure 49: Coulomb friction and Viscous friction

Because viscous friction is often termed as dynamic friction, one should not mistake it for the dynamic friction model that we will derive in chapter 5.1.2.

5.1.1.3 Static friction (Stiction)

Static friction, often termed as stiction, is the threshold value that describes the friction force at rest. Unlike Coulomb friction that is not determined at zero velocity, static friction introduces the force that prevents the sliding of the surfaces of two bodies in contact. In order to overcome static cohesion, stiction force has to be higher than Coulomb friction. Basically static friction can be modelled as counteracted to external forces that are below the stiction threshold, meaning that

$$F_s = F_e \text{ for } v = 0 \quad (109)$$

The corresponding graph is given in Figure 50:

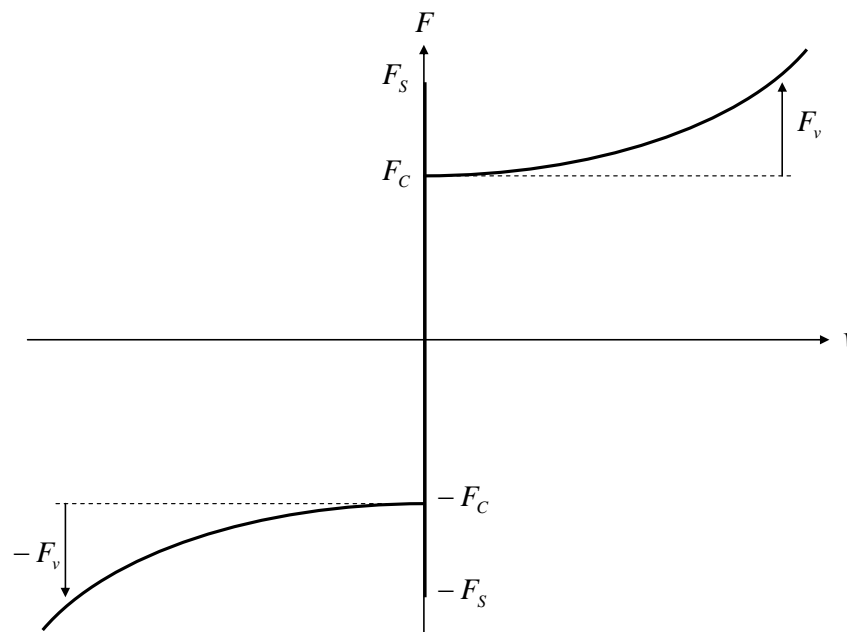


Figure 50: Coulomb friction, Viscous friction and Static friction

When estimating the friction parameters, we have used several cylinders that hold different threshold values for the stiction force. In order to evaluate static friction with a good precision, experiments at very low velocities have to be performed which is rather difficult by reasons of interfering noise in the position sensor. This gives rise to the need for the dynamic model in chapter 5.1.2, which mainly considers the bristle deflection of the lubricants at very low velocities.

5.1.1.4 Stribeck friction

According to the work of Richard Stribeck, friction decreases continuously with increasing velocity when entering the slipping phase. This phenomenon contradicts the discontinuous behaviour of the stiction force. It rather describes the friction force in the transition between sticking and slipping, which can be approximately estimated by the model

$$F_{St} = (F_S - F_C) e^{-\left|\frac{v}{v_\sigma}\right|^{\delta_\sigma}}, \quad (110)$$

in which v_σ denotes the Stribeck velocity and δ_σ the gradient of friction decay in the velocity dependent term.

This leads to a more general model at stick-slip motions that usually has the shape as depicted in Figure 51:

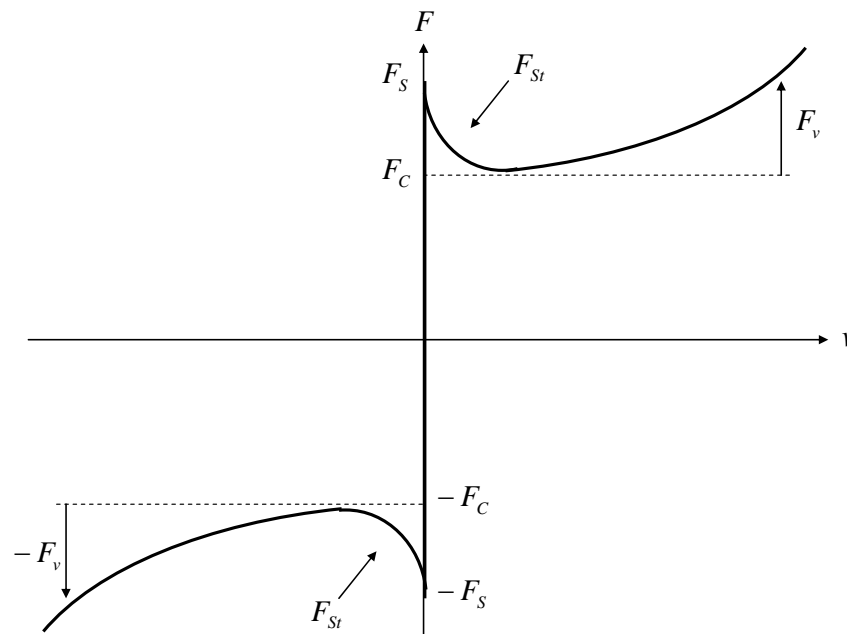


Figure 51: Coluomb friction, Viscous friction, Static friction and Stribeck effect

The peak in Figure 51 is related to the Stribeck force F_{St} at rest and is often termed as breakaway force beyond which the motion is initiated. The breakaway phase is most important for friction modelling and offers some anomalies that are not included in the static friction model but will be captured by a dynamic model later on.

The coefficients v_σ and δ_σ are the unknown parameters in the Stribeck model. A lot of friction models are sufficiently described with $\delta_\sigma = 2$ (e.g. *Adaptive Friction Compensation* by Canudas de Wit and Lischinsky [14]) however both Stribeck coefficients can be evaluated precisely in an easy manner by means of static friction maps that will be derived in chapter 5.2.2. The influence on the friction force of both Stribeck velocity and Stribeck gradient is shown in Figure 52 and Figure 53:

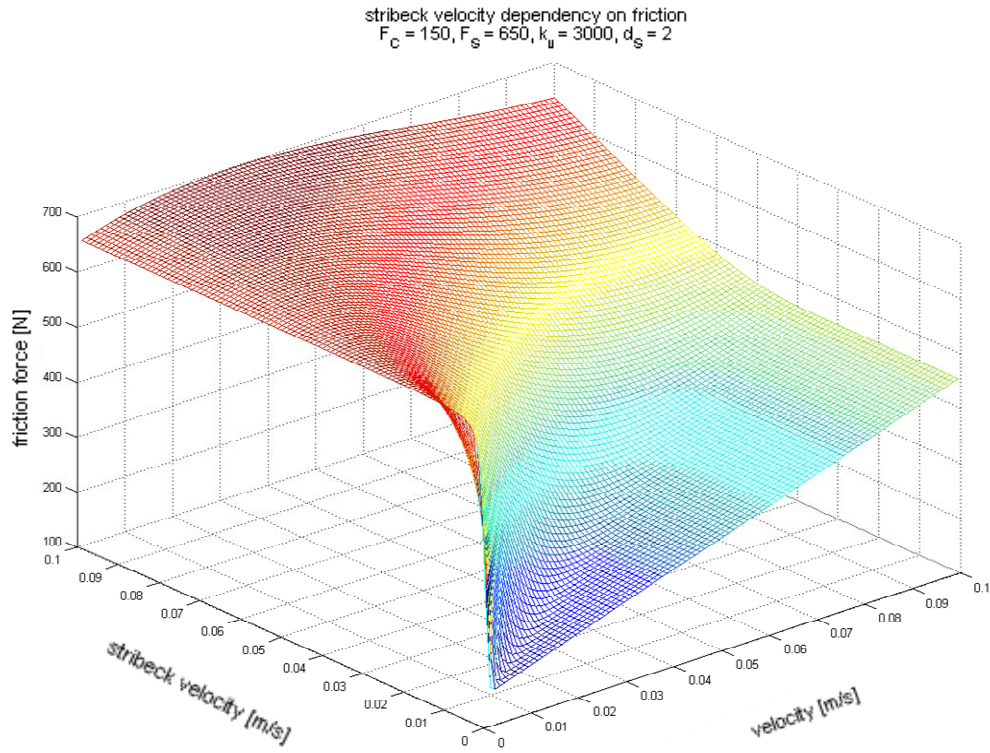


Figure 52: Relationship between Stribeck velocity v_σ and friction force

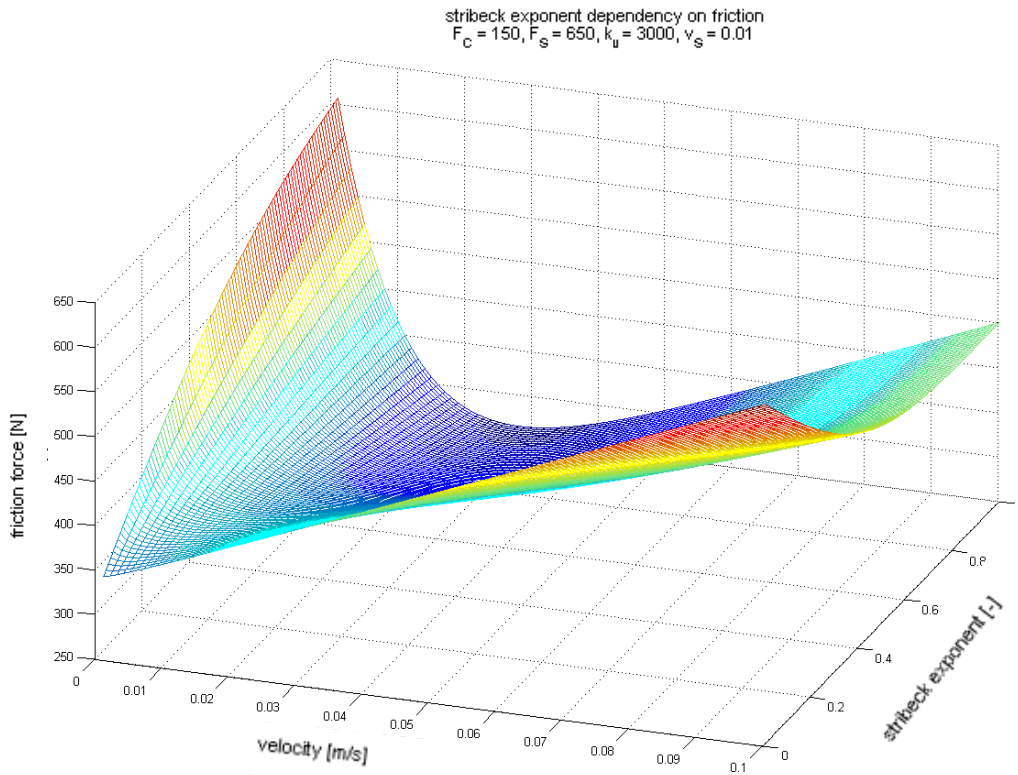


Figure 53: Relationship between Stribeck gradient δ_σ and friction force

It is obvious that the friction force is steeply falling with decreasing Stribeck velocity and increasing Stribeck gradient respectively. Superposing the derived models brings us a complete static friction model that has the form:

$$F = F_C + (F_S - F_C)e^{-\left|\frac{v}{v_\sigma}\right|^{\delta_\sigma}} + k_v |v|^{\delta_v} \text{sign}(v) \text{ or} \quad (111)$$

$$F = \alpha_0 + \alpha_1 e^{-\left|\frac{v}{v_\sigma}\right|^{\delta_\sigma}} + \alpha_2 |v|^{\delta_v} \text{sign}(v) \text{ respectively,} \quad (112)$$

where the substitutions give the static friction parameters

α_0 (Coulomb friction),

$\alpha_0 + \alpha_1$ (Static friction) and (113)

α_2 (Viscous friction).

5.1.2 Dynamic friction model

Although the static model describes the friction phenomenon sufficiently for a wide range of applications, the increasing demands for precise friction evaluation especially in the field of friction compensation of robotic manipulators have driven to the design of numerous dynamic friction models. This work will specifically focus on the bristle interpretation of friction which in [16] is described as the LuGre model. The next section will first give a brief summary of the dynamic properties of friction and finally present the basic idea of the LuGre friction model.

5.1.2.1 Dynamic properties of friction

Dynamic friction plays an important role when the contacting surfaces are steadily in transient motion affected by permanent velocity reversals. This emanates from the assumption that friction is not only determined by velocity but also depends on the rate of changes in the external force. Figure 54 shows the common relationship between breakaway force and the rate of force application.

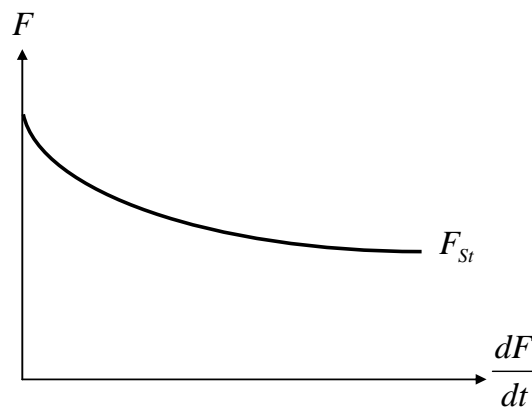


Figure 54: Relation between breakaway force and rate of force application [16]

Figure 54 points out that breakaway force decreases with increasing force rate. Moreover, friction is dependent on the rate of velocity changes. Therefore descriptive experiments have been exerted in order to capture the friction behaviour at different accelerated motions (see Figure 55 below).

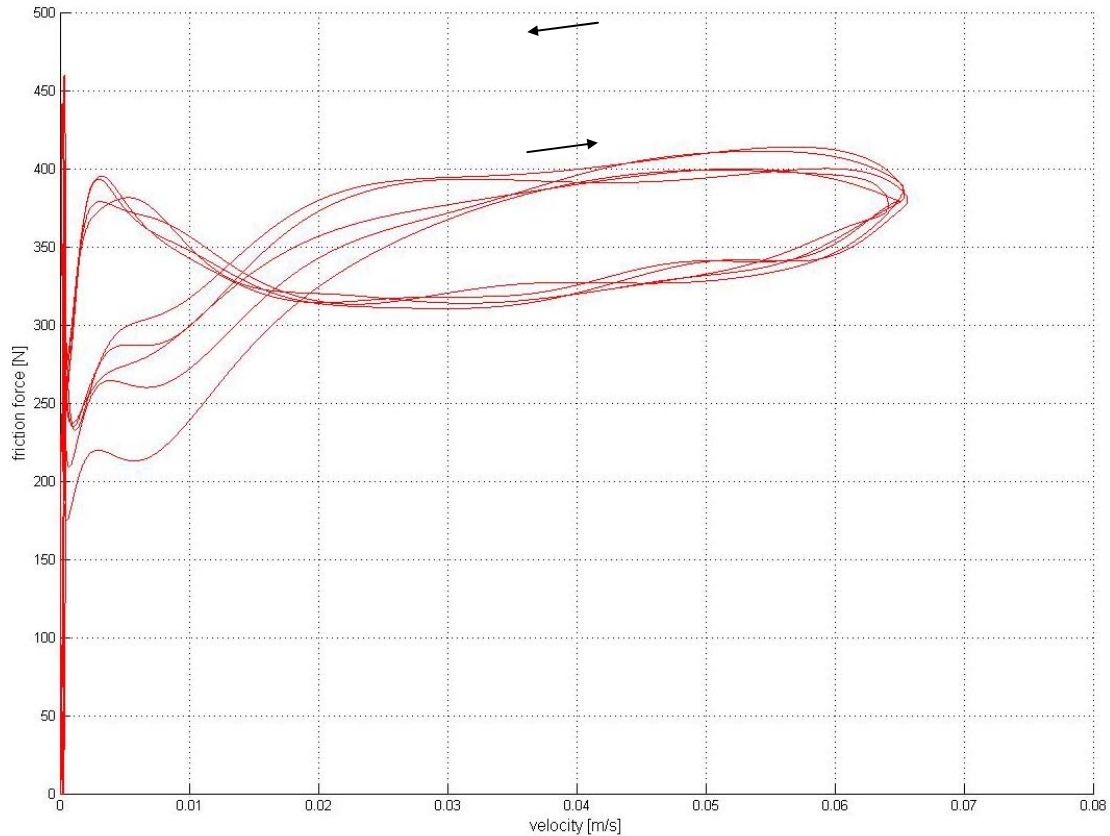


Figure 55: Frictional lag

Figure 55 reveals a hysteresis loop that indicates the significant difference in the friction force for increasing and decreasing velocities of a unidirectional motion. Whereas the breakaway force is higher for decreasing velocities (~ 500 N), the Stribeck effect is very distinctive at increasing velocities. It has also been experimentally proven that the hysteresis loop grows wider as the velocity variation becomes faster.

5.1.2.2 The LuGre Model

The Lund-Grenoble model (*LuGre*) is a widely used dynamic model that describes the microscopic deflection between the contact surfaces in terms of a damping-spring behaviour. The dynamic system can be modeled by an elastic spring, where the friction force is related to the average deflection of the bristles in the sticking phase. For this purpose, we will derive a differential equation that leads to a new system state, namely the bristle deflection z :

$$z = \sum_{i=1}^k z_i, \quad (114)$$

where k denotes the number of bristles in the contacting area of the two surfaces.

The typical microscopic bristle deflection as assumed to appear in a hydraulic cylinder is sketched in Figure 56:

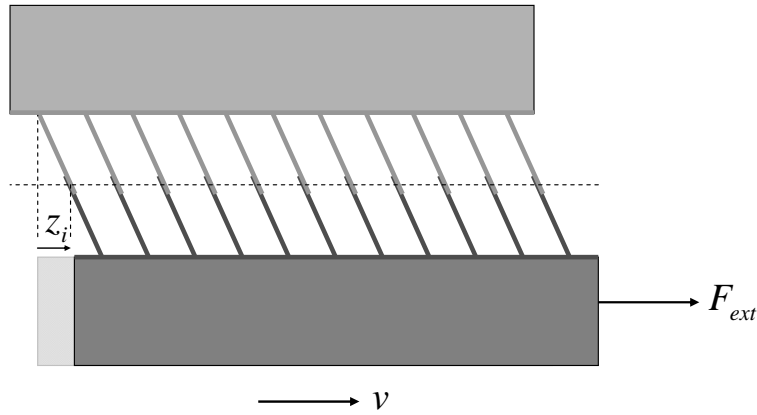


Figure 56: Schematic bristle deflection of contacting surfaces in motion

The standard parametrization of the bristle model can be obtained by establishing the dynamic parameters σ_0 and σ_1 which correspond to the bristle deflection z . By adding linear viscous friction, the dynamic friction force can then be computed as follows:

$$F = \sigma_0 z + \sigma_1 \frac{dz}{dt} + \alpha_2 v, \quad (115)$$

where σ_0 implies the bristle stiffness and σ_1 represents the damping behaviour of the bristles.

For small displacements the bristles will behave like a spring-damping system in whose steady-state the deflection z is a function of the velocity. An appropriate model is given in [14]:

$$\frac{dz}{dt} = v - \frac{\sigma_0 z}{g(v)} |v|, \quad (116)$$

where v is the piston velocity and $g(v)$ the static friction regardless of viscous friction:

$$g(v) = \alpha_0 + \alpha_1 e^{-\left|\frac{v}{v_\sigma}\right|^{\delta_\sigma}} \quad (117)$$

We noticed that estimated cylinder friction in the hydraulic cylinder shows a characteristic which can be divided into three different phases:

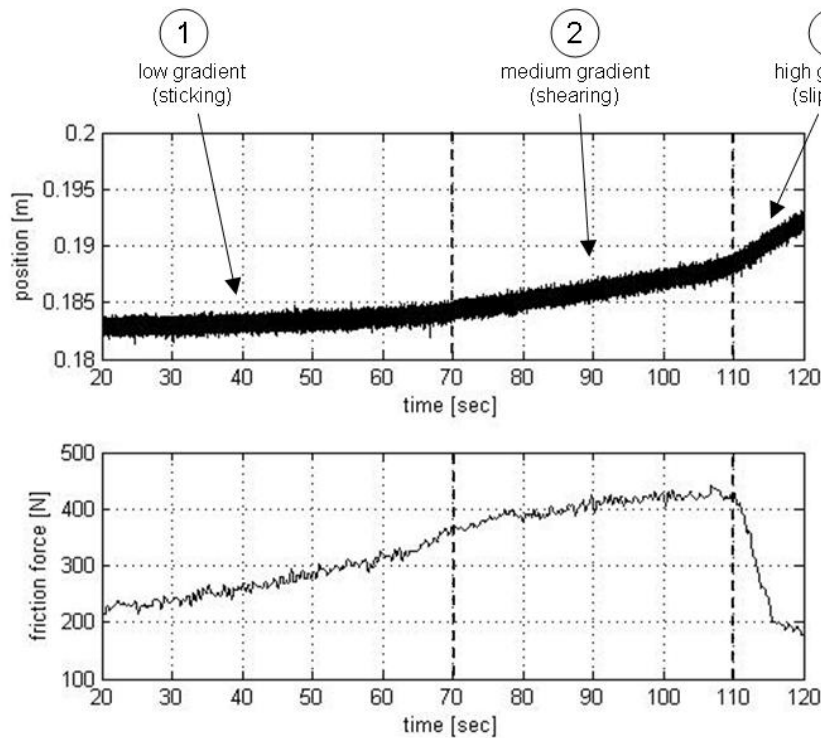


Figure 57: System response of a ramp input control

When increasing the control input from rest, pressure is building up and thus friction force increases slowly (sticking phase). In this phase the bristle deflection and piston velocity respectively is almost zero. Then, at a certain pressure balance, the piston moves due to bristle deflection (shearing phase). Once, the pressure difference between both cylinder chambers exceeds an upper threshold, the piston moves with a noticeable velocity whereas the friction force is determined by Coulomb friction and viscous friction (slipping phase). Figure 58 shows the bristle deflection for all the three phases:

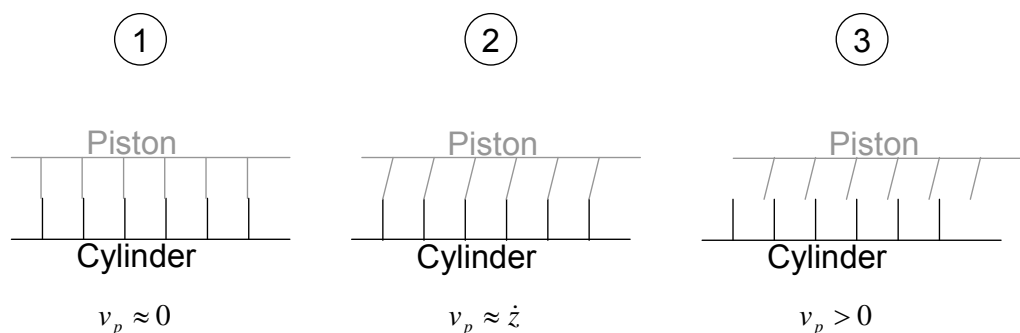


Figure 58: Bristle deflection of hydraulic cylinder

The state variable z will be determined by means of friction experiments in the following chapter.

5.2 Estimation of nominal friction parameter

In this chapter we will apply the derived analytical models of the previous sections for the determination of the friction parameters. At first we describe the test bench that we will use for the friction measurements including the control interface of the valve block. Static parameter estimation with open loop experiments is done in chapter 5.2.2. With the results of static friction, we can run dynamic experiments in order to estimate the dynamic parameters by non-linear numerical methods. Here, we use appropriate experiments that enhance the effects of the unknown values. Finally we adapt the parameters to a suitable friction model and compare the analytical model to real-world friction.

For ran the experiments for the estimation of the friction parameter on two different hydraulic cylinders. The Rottne cylinder was used as the 3rd cylinder, mounted on the laboratory crane. This cylinder was used before in real-world applications. The 2nd cylinder was courtesy of Kalmar University. Its maximum operation pressure was limited to 40 bars due to the mounted pressure sensors (140 bars at the Rottne cylinder).

5.2.1 Experimental set-up

There have been several possibilities to build up an appropriate test rig for friction evaluation. We decided not to dismount the cylinders from the crane due to reconfiguration and difficulties in connecting them to an external body. The idea was to simply disconnect the 3rd cylinder from the crane-tip so that it was free to swivel around the upper joint in which the cylinder was fixed to the 3rd link. In order to keep the crane stable we used a heavy frame that supported the 2nd link from below. Finally we turned the telescopic beam to the position in which it contacted the 2nd and tied both bodies together with a lashing strap to get rid of the 3rd joint's backlash.

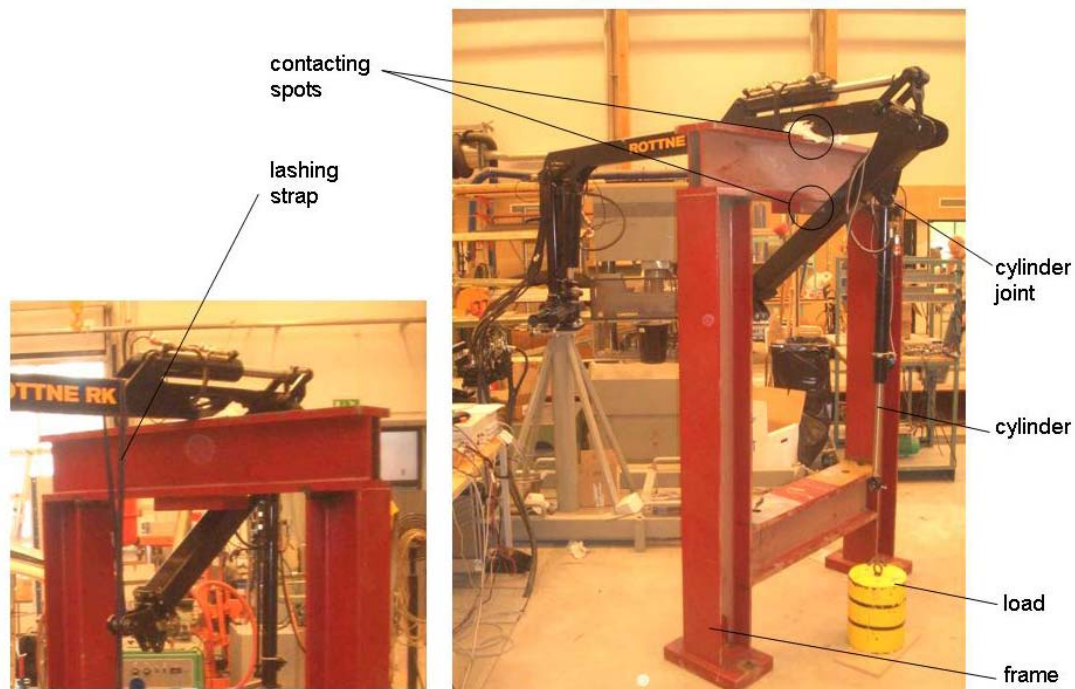


Figure 59: Test-rig for friction measurements

We used several loads with different mass that we simply connected to the cylinder's end. It had to be assured, that the load was not able to hit the ground when extending the cylinder

thoroughly. Moreover, we were not sure if the cylinder begins to oscillate when moving the piston with high velocities. After several tests we found out that heavy cylinder vibrations did not occur, not even in accelerated motions.

With pressure sensors located in each chamber as well as a length sensor for measuring the piston extension we were able to determine the resulting friction force according to equation 118:

$$F_{fr} = p_1 A_1 - p_2 A_2 + mg + m\ddot{x}, \quad (118)$$

where m is the mass of the moving parts (load, piston and rod).

We used a *dSpace* system that we fed with the input signal of both pressure and length sensor. With the *Control Desk* software we were able to capture the signals from the *dSpace* system and moreover, the software calculated the friction force continuously. In order to analyse the signals we saved the data as *mat*-files that we later imported in *MATLAB* to obtain suitable charts.

In order to excite the proper output signal to the valve block we had to build a *Simulink* block, specified by the characteristics of the control box to the valves. The block diagram is shown in Figure 60 which also points out the opposed control signals to port A and B:

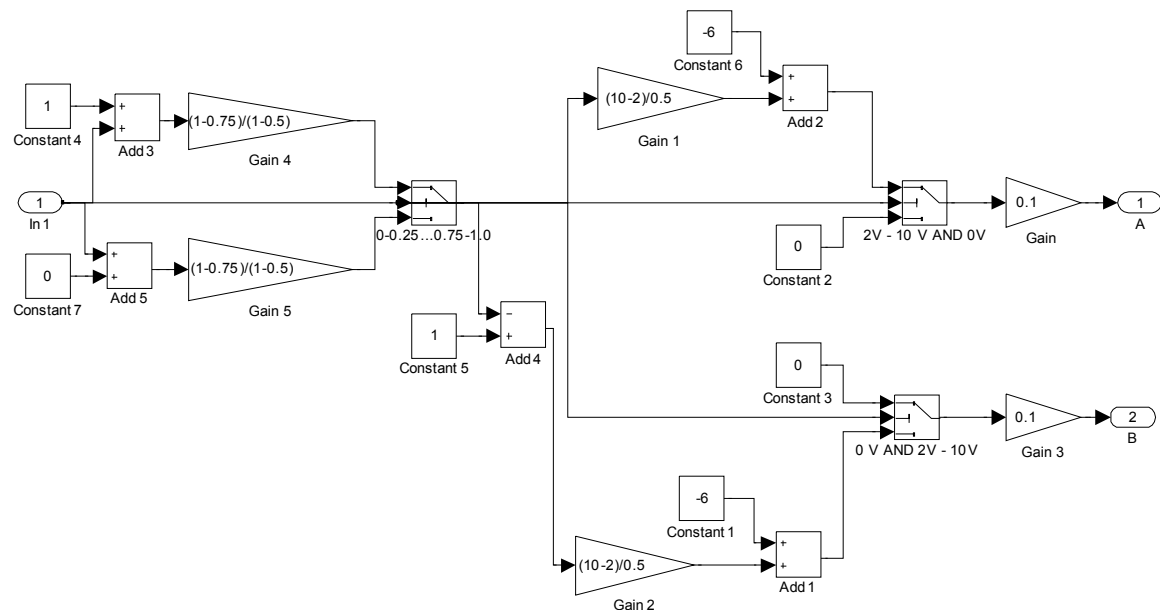


Figure 60: *Simulink* block for output excitation in *dSpace*

Before beginning with the experiments for the estimation of friction parameters, we performed several test runs with small sinusoidal inputs that should be intended to represent the system's frictional behaviour within stick-motions. By implementing equation 118 to the *dSpace* layout we were able to see how friction force was changing due to a sine function input.

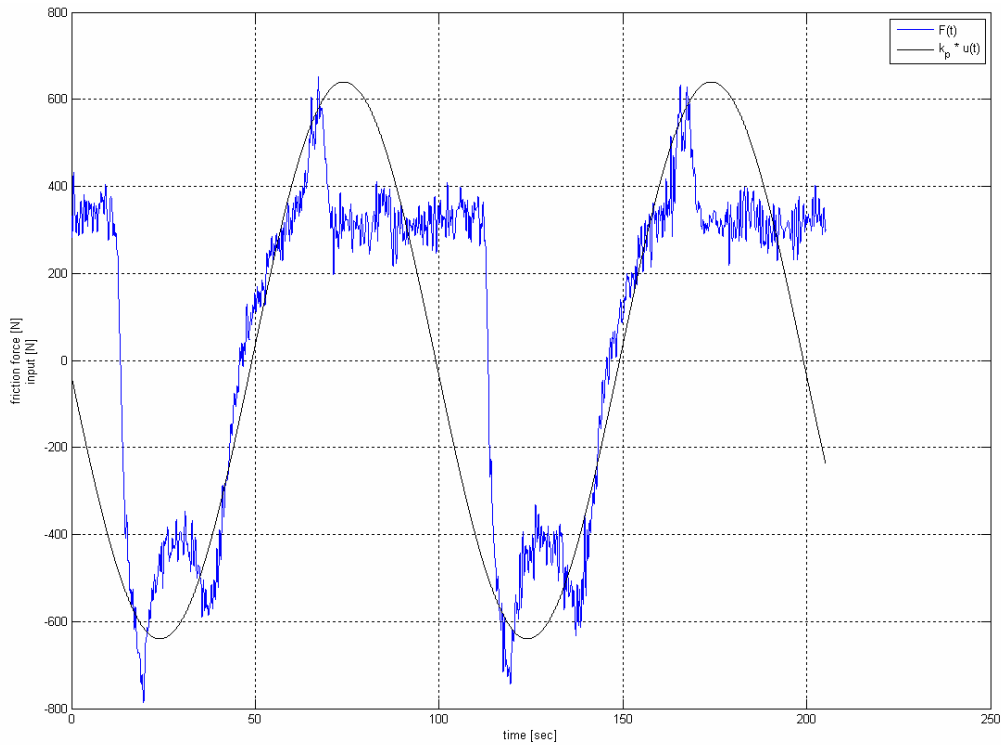


Figure 61: Friction response on sinusoidal input function

Although friction force characteristics apparently represented the point of break-away, we had to track the position signal in order to observe the piston extension that was barely visible to the naked eye. Piston position and its derivative are depicted in Figure 62 and state the slipping regime of the piston:

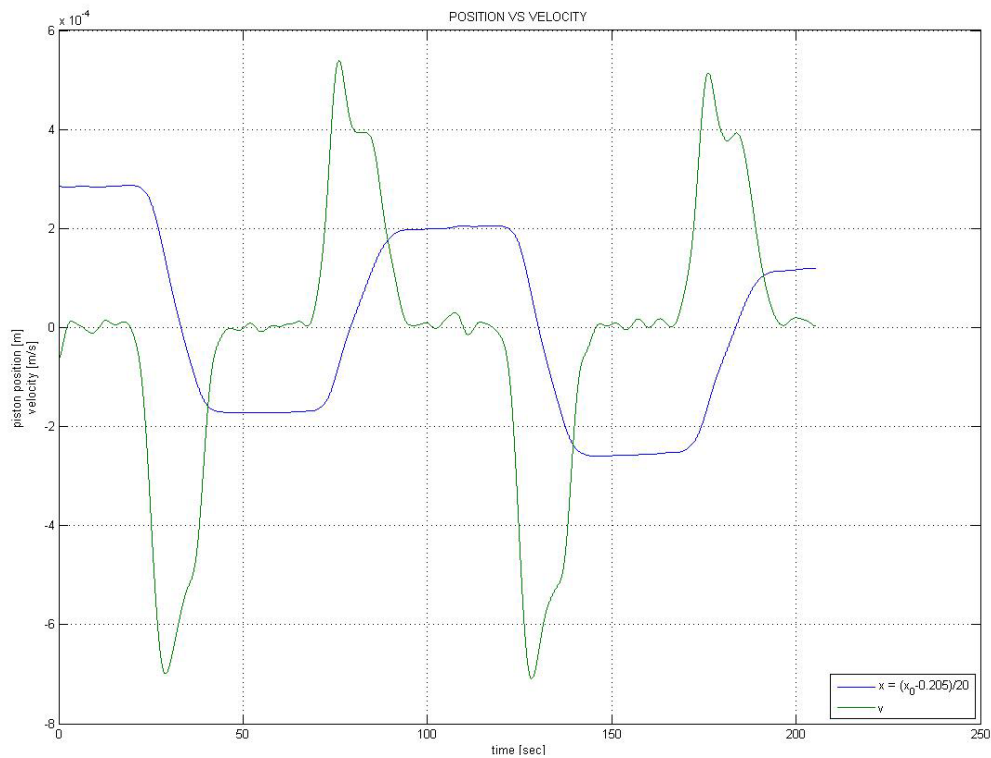


Figure 62: Position and velocity tracking within stick-slip motions

The above derived figures approve that friction force at our test cylinder matches the curves from the previous friction model. The test bench had been configured properly and we were ready to perform experiments for friction parameters estimation.

5.2.2 Static parameter estimation

In this section we will briefly summarize the models of the preceding chapters to a general static friction model. Then static friction will be evaluated through open-loop experiments during constant velocity motions of the hydraulic cylinder. Finally the resultant derived friction-velocity maps can be used for estimating the unknown nominal parameters of the static model.

In chapter 5.1.1 the steady state friction characteristics were given by

$$F = \alpha_0 + \alpha_1 e^{-\left|\frac{v}{v_\sigma}\right|^{\delta_\sigma}} + \alpha_2 |v|^{\delta_v} \text{sign}(v) . \quad (119)$$

In order to determine the static parameters we had to run open-loop experiments on both hydraulic cylinders. Most important to evaluate static friction is to keep the velocity constant due to the effect of frictional lag (see also Figure 55). In this regard we tried to apply a PID velocity control but it failed due to a time delay in the crane's system response. We then simply controlled the output voltage and the current to the valves respectively and noticed that this control method keeps the piston velocity constant as well.

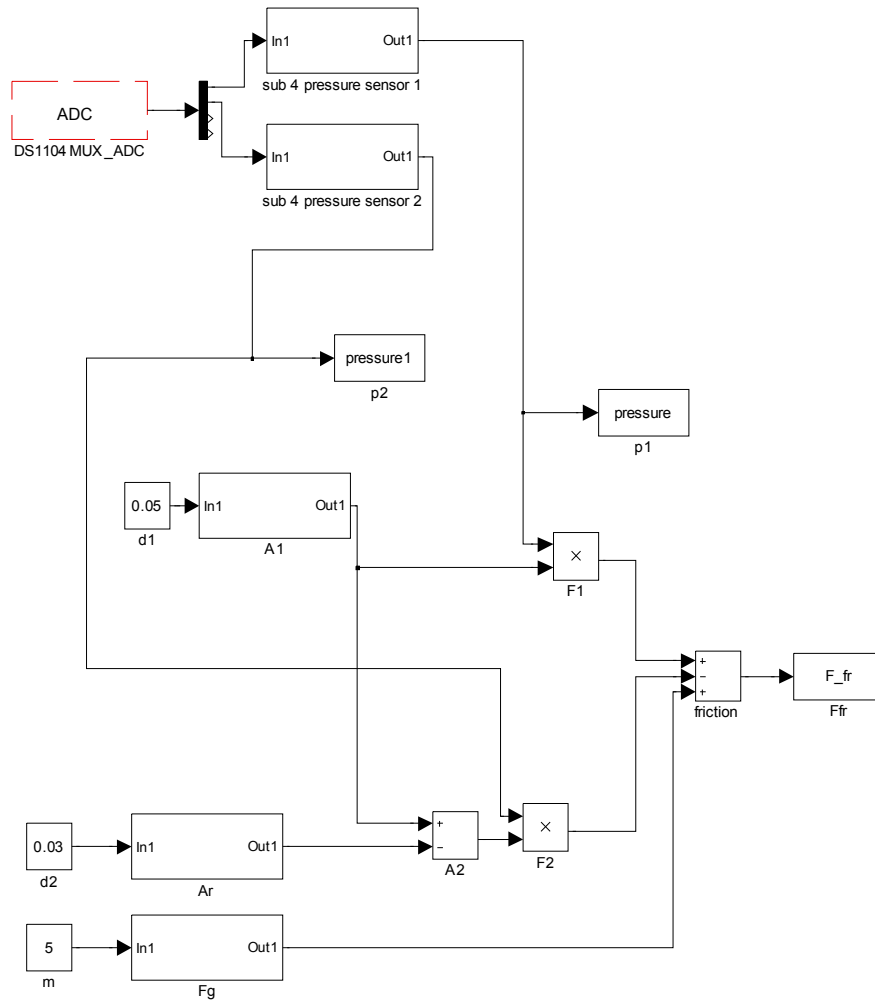
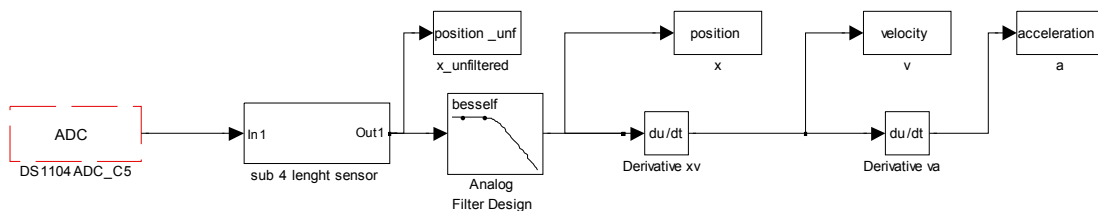
To capture the data loggings, the following signals have been used for static parameter estimation:

- Pressure sensor in the upper cylinder chamber p_1
- Pressure sensor in the lower cylinder chamber p_2
- Length sensor of piston position x_p and its differentiation v_p respectively

Friction force as calculated in equation 83 is then a function of both pressure signals and the cylinder dimensions ($\ddot{x}_p = 0$):

$$F_{fr} = p_1 A_1 - p_2 A_2 + mg \quad (120)$$

The corresponding *Simulink* models for friction force and piston velocity are shown in Figure 63 and Figure 64.

Figure 63: *Simulink* data processing of friction forceFigure 64: *Simulink* data processing of piston velocity

For the measurement of the piston position we had to add a *Bessel-filter* to our *Simulink* model in order to read off the real piston velocity online at very low velocities. Here, the time delay of the filter did not carry weight since the cylinder extended extremely slowly. To keep track of higher velocities, we increased the filter's edge frequency so that a constant signal was always logged within a full extension. For further data processing in *MATLAB* we used the unfiltered signal. Both logging layouts are shown in Figure 65.

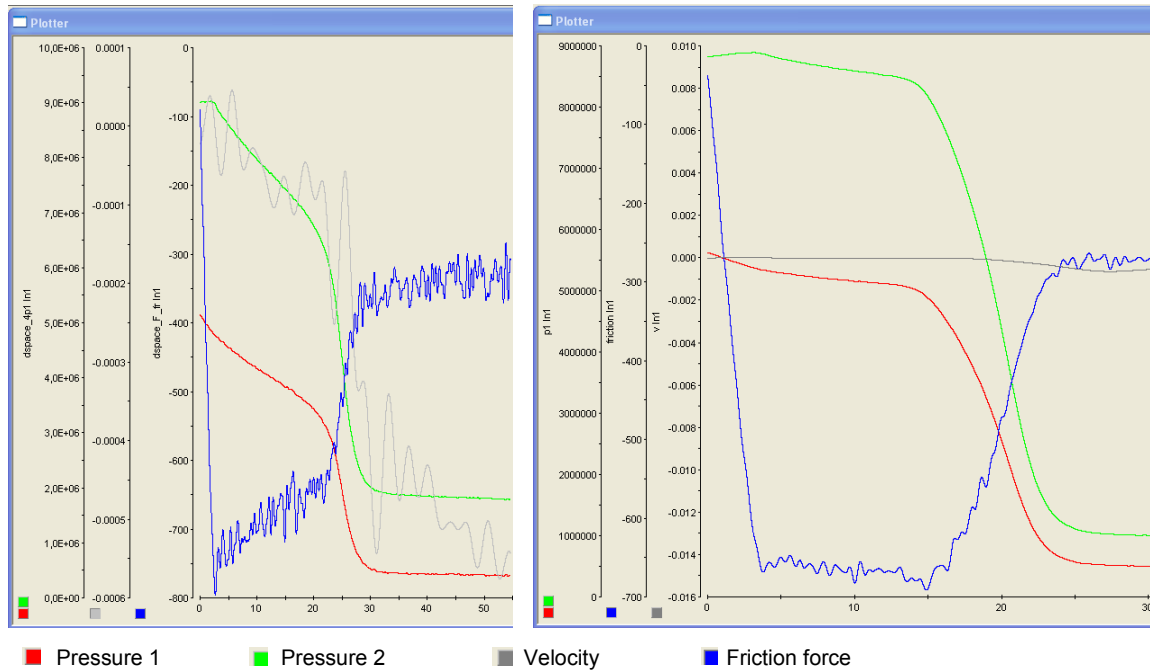


Figure 65: *dSpace* data logging with unfiltered (left) and filtered (right) velocity signal (grey)

We began the experiments with approximately ten different piston velocities in the range of $0.0001 \frac{m}{s}$ to $0.1 \frac{m}{s}$. Within this range numerous values were collected at very low velocity in order to specify the identification of the Stribeck effect. Afterwards we applied the complementary output to the valves to achieve negative velocities for the retracting motion. We also evaluated the static friction at zero velocity by finding the maximum output, friction force respectively at which the piston was kept just about from moving. Hence we were able to determine the coefficients α_0 and α_1 immediately.

After a certain delay all sensor signals remained on a constant level. We saved the *mat* data files and created a chart in *MATLAB* that represented the friction force at different velocities.

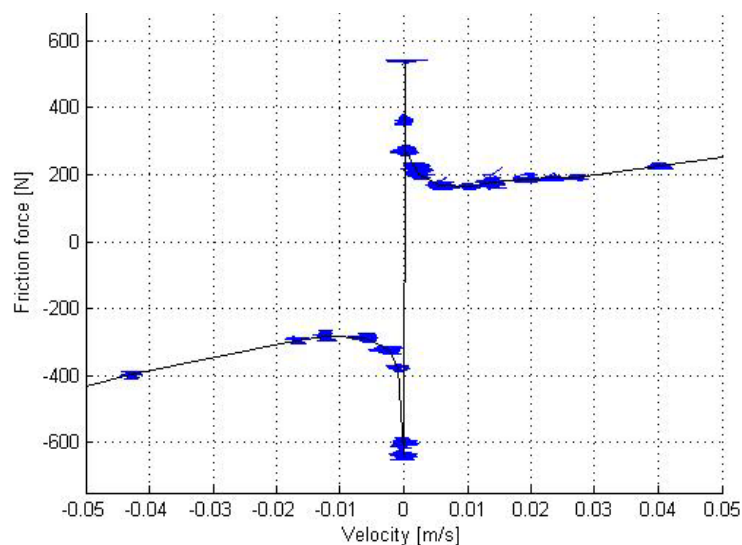


Figure 66: Measured friction force over velocity

In order to obtain a general friction map we had to find a continuous behaviour between friction and velocity. For this purpose we drew a curve through the measured values and applied hereby two different methods.

The first was to simply average the values at each velocity level to eliminate the error due to noise in the sensor signals. As an output, we yielded several well-defined friction values that corresponded each to a certain velocity. This form of a friction map sufficiently describes all the unknown static parameters as graphically estimated in Figure 67.

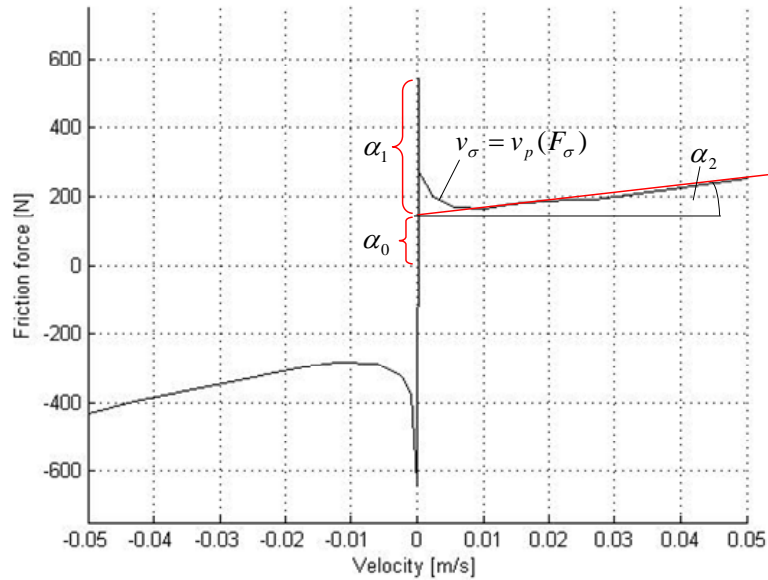


Figure 67: Graphical estimation of static parameters

The Stribeck velocity was determined by equating v_p and v_σ in equation 119, which approximately resulted in:

$$F_\sigma = \alpha_0 + \frac{\alpha_1}{e} \text{ for } \alpha_2 |v_p| \ll F_\sigma \quad (121)$$

The Stribeck velocity to solve is then the point of intersection at the specific friction force F_σ .

Another way of finding an analytical expression of the cylinder friction is to use the optimization toolbox in *MATLAB*. Therefore we applied the *lscurvefit*-command to the experimentally evaluated values. By doing so we were able to determine a non-linear function that represented the static parameters, solved through least square deviation:

$$\min_{\hat{\alpha}_0, \hat{\alpha}_1, \hat{\alpha}_2, \hat{v}_\sigma} \sum_{i=1}^n \left[F(v_p) - \hat{F}(v_p) \right]^2, \quad (122)$$

where $F(v_p)$ includes the measured friction values and $\hat{F}(v_p)$ is the non-linear function solved by the *lscurvefit*-command in *MATLAB*.

However, in this case we encountered the problem of unequally distributed values, which

means that the majority of our measured values corresponded to low velocities. Consequently *MATLAB* solved the least square problem with an inaccurate curve gradient at higher velocities or insufficient consideration of the Stribeck effect (see Figure 68). Consistently, we decided to estimate the parameters manually as proposed in Figure 67.

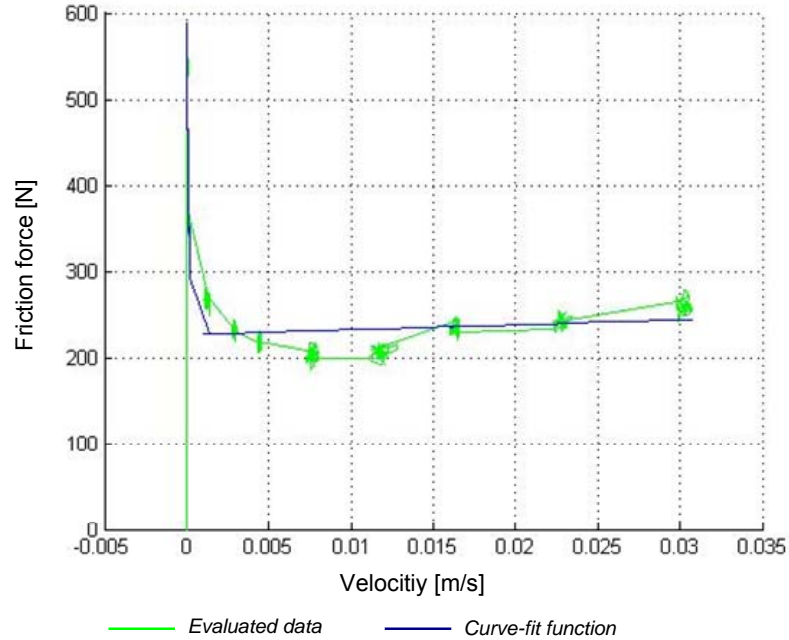


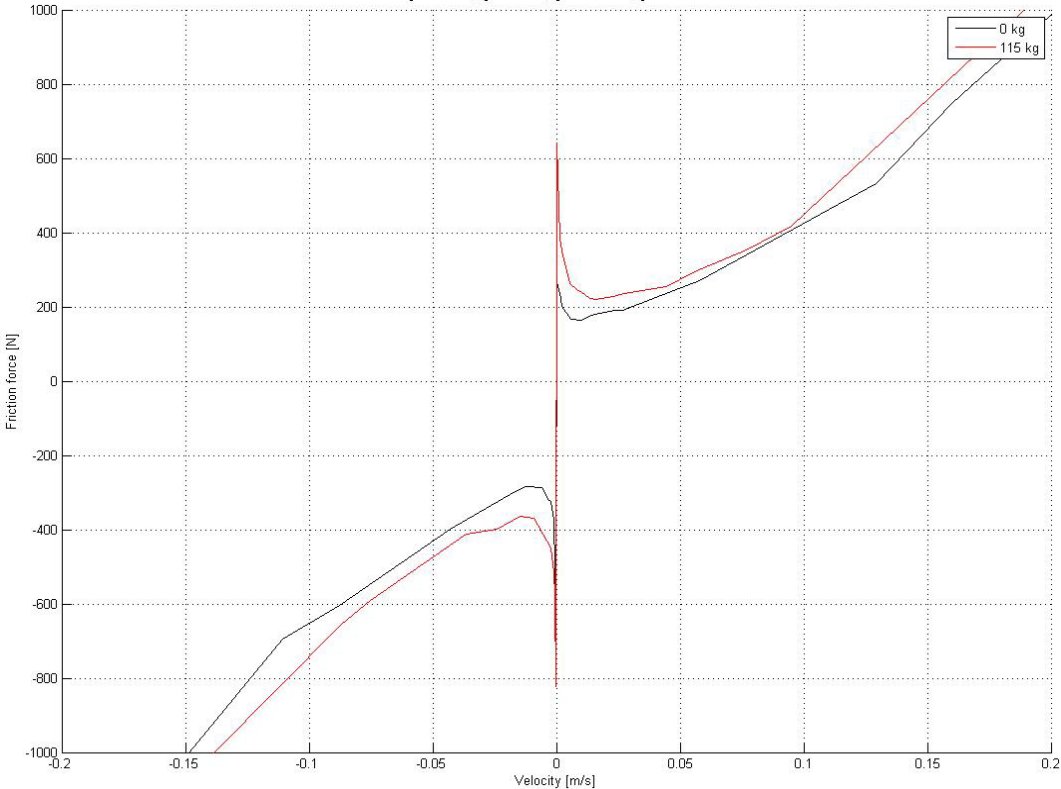
Figure 68: Problem of inaccurate curve gradient when solving the least-square function

Thereafter we substituted the derived parameters in equation 119 in order to verify the resulted continuous graph with the experimentally obtained curve. The friction maps for both cylinders are depicted in Figure 69 whereas the static parameters are listed separately in Table 3:

Cylinder	α_0	α_1	α_2	v_σ
Rottne (0 kg)	160 / 280	180 / 120	8000 / 12000	0.002 / 0.002
Rottne (115 kg)	170 / 350	450 / 450	10500 / 12000	0.004 / 0.002
Kalmar (0 kg)	105 / 80	350 / 300	1250 / 1800	0.01 / 0.015
Kalmar (115 kg)	140 / 100	310 / 350	1200 / 1800	0.015 / 0.02

Table 3: Evaluation of static parameters (extension / retraction)

Rottne cylinder



Kalmar cylinder

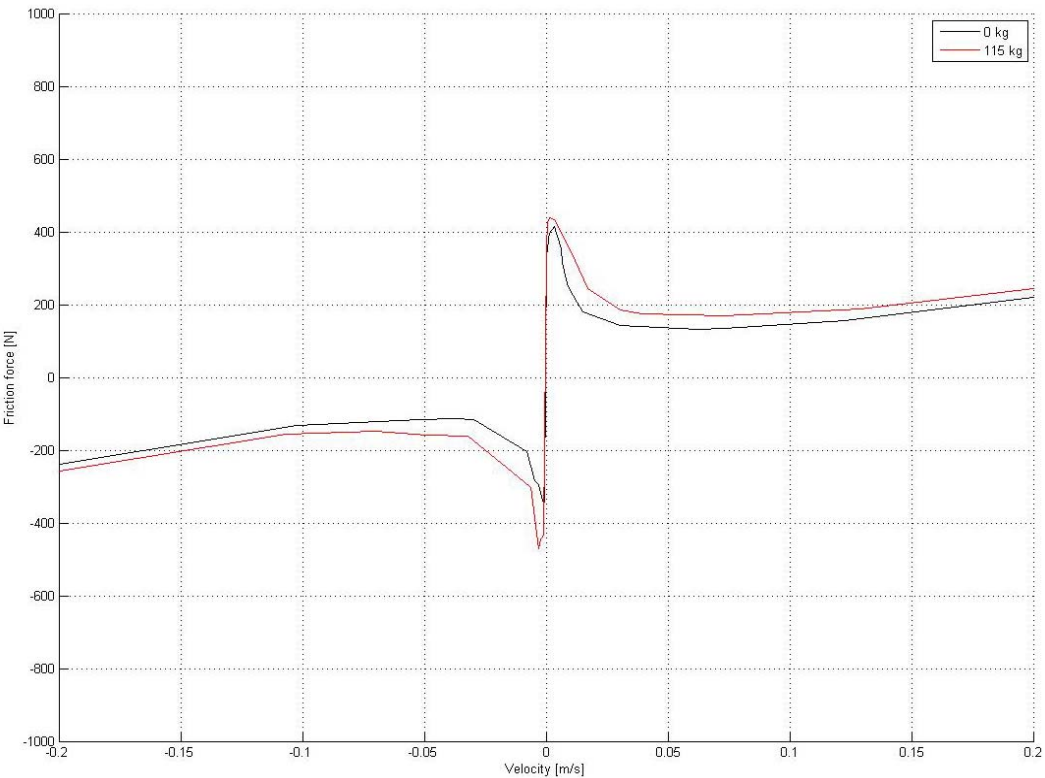


Figure 69: Static friction map of Rottne cylinder and Kalmar cylinder

From Figure 69 we basically notice two fundamental differences. On the one hand, friction force at the Rottne cylinder increases more heavily than the Kalmar cylinder does. This might probably arise from the fact that the Rottne cylinder has been used in real-world application before and consequently it consists of wear particles that have been piled up as a consequence of abrasion. Another significant disparity is given by a much higher Stribeck velocity of the friction force at the Kalmar cylinder. This is reflected in a major specification of the Stribeck effect within in the friction curve, represented by its minimum at higher velocities.

One should bear in mind that the above friction parameters have been experimentally evaluated and may further change as dependent on temperature variations, position and normal forces in contact. Nevertheless, as start to our dynamic model, the derived coefficients turn out to be suitable for the derivation of static friction maps and further parameter estimation.

5.2.3 Dynamic parameter estimation

The derived static friction model is a fundamental description of hydraulic cylinder friction. Nevertheless, there are several other important friction properties that cannot be explained solely by static models. Modelling dynamic friction is therefore crucial for the design of friction compensation schemes in order to capture the instantaneous response on internal dynamics, e.g. velocity changes.

Previous work on dynamic friction has exposed that stick-slip motions and velocity reversals are extremely sensitive to the dynamic parameters σ_0 and σ_1 . In order to capture dynamic friction effects we therefore apply different identification mechanisms representing the dynamics of the friction internal state variable z . At first we focus on the evaluation of the dynamic parameter σ_0 , that is the spring-like coefficient of the bristle deflection. For this purpose we apply a gently inclined ramp function as an input signal to the valves, beginning with the piston at rest. The second dynamic parameter will then be determined by a system response to a ramp input whereas the damping characteristics of the bristles represent σ_1 . In both cases we estimate the coefficients for extracting motions as well as for retracting motions. The results will be compared at the end of this section.

5.2.3.1 Estimation of dynamic parameter σ_0

Let us use a small ramp function as an input to the valves. The corresponding *Simulink* model is depicted in Figure 70:

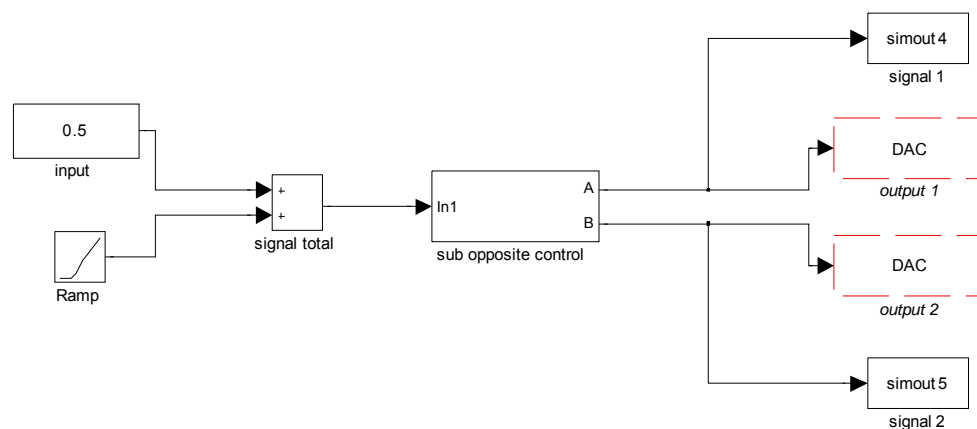


Figure 70: *Simulink* model of ramp input control

Rewriting equation 119 for ramp control allows us to neglect the damping term while assuming $v \approx 0$ and $\dot{z} \approx 0$:

$$F \approx \sigma_0 z \approx u(t), \quad (123)$$

where $u(t)$ is the input function to the valves.

The internal state z is determined by means of the following equation

$$\frac{dz}{dt} = v - \frac{\sigma_0 z}{\alpha_0 + \alpha_1} |v|, \quad (124)$$

in which $g(v \approx 0) = \alpha_0 + \alpha_1$.

When applying the input ramp function $u(t) = ct$ with small $c > 0$, equation 124 can be integrated for $v > 0$ as follows:

$$z(t) = x_p(t) - x_p(0) - \frac{c}{2(\alpha_0 + \alpha_1)} \left(x(t)t + \int_0^t x(\tau) d\tau \right) \quad (125)$$

It is most important that the experiments are performed from rest, that is $z(t_0) = 0$, which means that we initiate the ramp signal when the piston is fully retracted. In this special case we can assure that the bristles are not deflected by means of unbalanced chamber pressures. Furthermore, we have to compute z within the time interval $[0, T]$, whereas T specifies the time up to the very moment before point of break-away.

Next, the ramp responding curves are depicted together with piston position and friction force for both hydraulic cylinders.

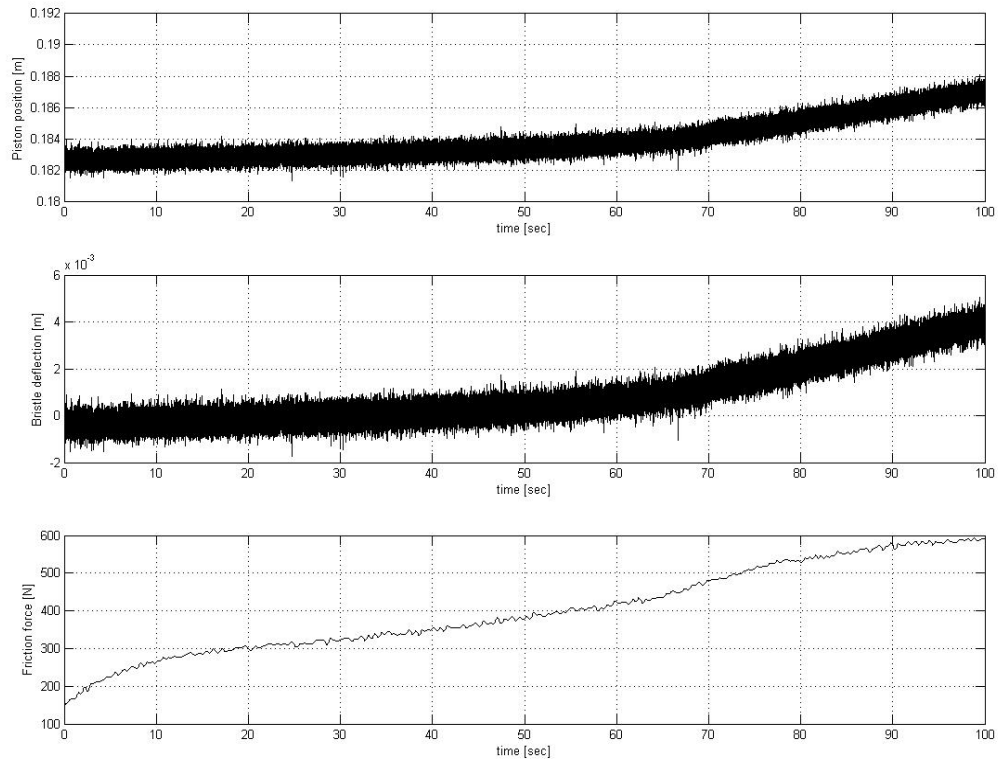
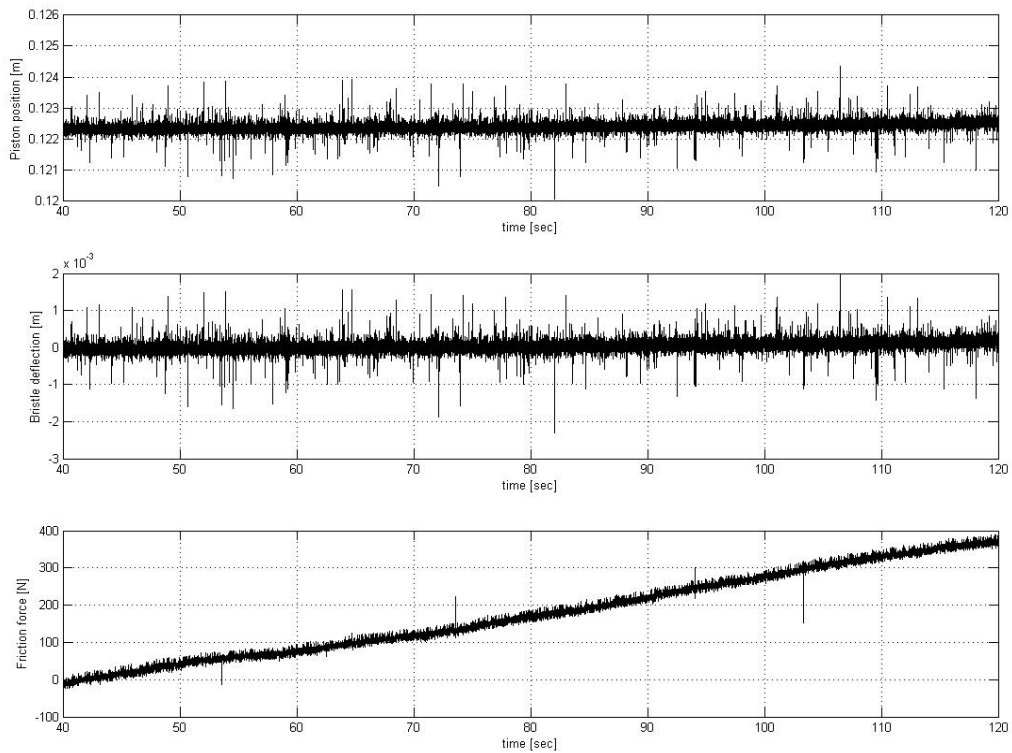
Rottne cylinder*Kalmar cylinder*

Figure 71: Ramp response of Rottne cylinder and Kalmar cylinder

When comparing both ramp responses, we consider a much stronger shearing strain at the Rottne cylinder with a maximum bristle deflection of approximately 4 mm. The deflection at the Kalmar cylinder is almost unrecognizable and only measurable by further data processing, e.g. averaging the data samples and creating a mean curve.

One should bring to mind that ramp control enhances the springing effect of bristles and though we can easily compute the bristle stiffness by solving equation 123 for σ_0 . When averaging the data vectors Z and U in the proper relation, σ_0 is then determined by

$$\sigma_0 = Z^{-1}U = \frac{Z^T U}{Z^T Z} \cdot [14] \tag{126}$$

Since point of break-away was reached very early at the Kalmar cylinder, we had to use different input ramps for both cylinders in order to log the datas for nearly the same time period.

The computed values for the first dynamic coefficient are listed below in Table 4:

Cylinder	σ_0 extending	σ_0 retracting	σ_0 averaged
Rottne (c=0.01)	1.2 x 10e5	1.0 x 10e5	1.1 x 10e5
Kalmar (c=0.0001)	1.0 x 10e6	1.2 x 10e6	1.1 x 10e6

Table 4: Estimation of dynamic parameter σ_0

According to Table 4 the bristle deflection of the Kalmar cylinder is far less than it is at the Rottne cylinder. Therefore it is evident that its bristle stiffness and consequently its averaged coefficient σ_0 are approximately higher by the power of ten.

5.2.3.2 Estimation of dynamic parameter σ_1

The estimated coefficients are now being used for computing the second dynamic parameter σ_1 . Therefore we run open-loop experiments again, but to cover the bristle's damping behaviour we use step inputs instead of a ramp control. The corresponding *Simulink* block is shown in Figure 72.

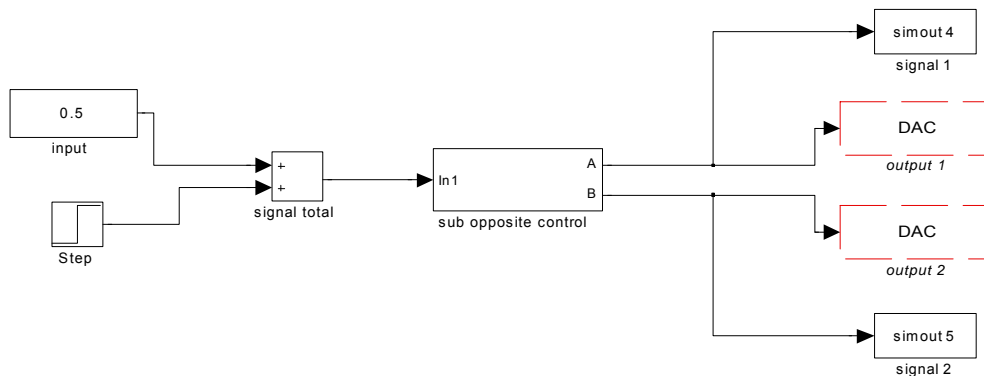


Figure 72: *Simulink* model of step input control

Within the shearing phase, a step input leads approximately to $\dot{z} \approx \dot{x}_p$ which lets us simplify equation 119 to

$$m\ddot{x}_p + \sigma_0 x + (\sigma_1 + \alpha_2)\dot{x}_p = F, \quad (127)$$

where σ_0 and α_2 are the previously predetermined coefficients and σ_1 is the 2nd dynamic parameter to solve.

Notice that due to inconstant piston velocity we have to consider Newton's second law to our friction model. In this regard, we derive the unfiltered piston position twice and multiply the result with the mass of the cylinder's loose parts that are predominantly its rod, its piston and the external load.

When running the experiment, it is most crucial to use sufficiently small step inputs in order to examine the bristle behaviour within the stiction regime. This condition turned out to be almost unmanageable because of immoderate noise that interfered with the smallish and unfiltered velocity signal. The following step responses were investigated through *MATLAB* data processing. Figure 73 shows the step input response for both cylinders whereas the estimated parameters for σ_1 are given in Table 5:

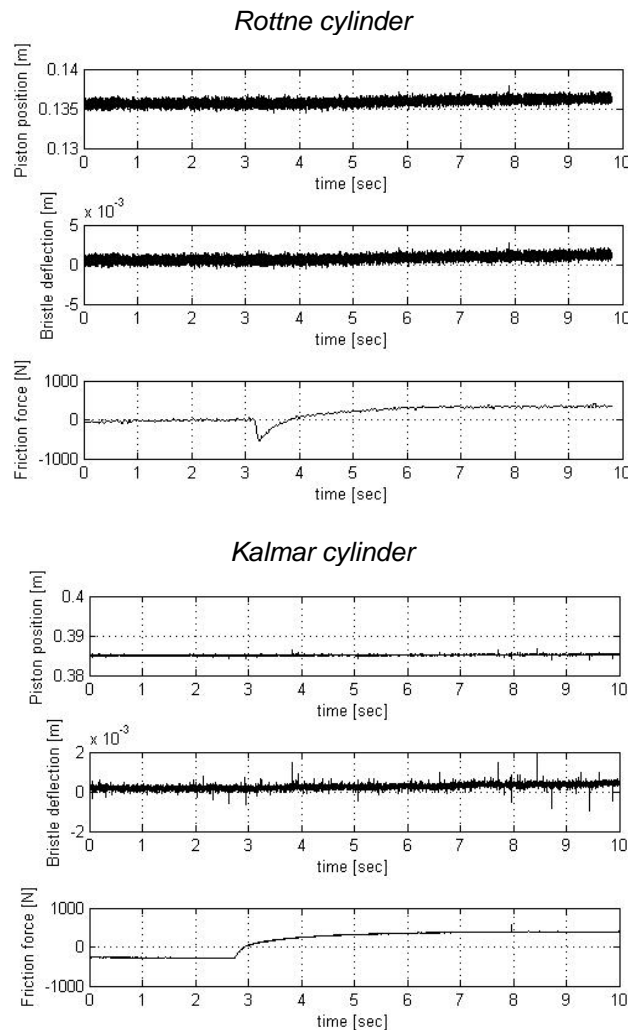


Figure 73: Step response of Rottne cylinder and Kalmar cylinder

Cylinder	$\sigma_1 \text{ ext}$	$\sigma_1 \text{ ret}$	$\sigma_1 \text{ avg}$
Rottne	-1.53×10^4	-1.55×10^4	-1.54×10^4
Kalmar	-1.74×10^5	-1.73×10^5	-1.74×10^5

Table 5: Estimation of dynamic parameter σ_1

From Table 5 we can slightly discover a bristle displacement in both cases due to the step input signal. Again, the deflection is larger at the Rottne cylinder which means that the piston is damped at a lower level. This results in a low damping coefficient σ_1 which is apparently ten times smaller than the coefficient estimated for the Kalmar cylinder.

5.2.4 Influence on friction due to variations in load and pressure

Hydraulic cylinders may show varieties in friction behaviour when performing under different circumstances. Friction force is most likely to depend on outer environmental conditions. In order to investigate this dependency and to expose the difference in friction we ran several experiments in which we varied the main control pressure and the cylinder load.

Surprisingly we found out that neither lower pressure nor increasing mass makes a significant difference in the friction force. Figure 74 shows the derived static friction curves for pressure supply of 140 bar (black curve) and 100 bar (red curve):

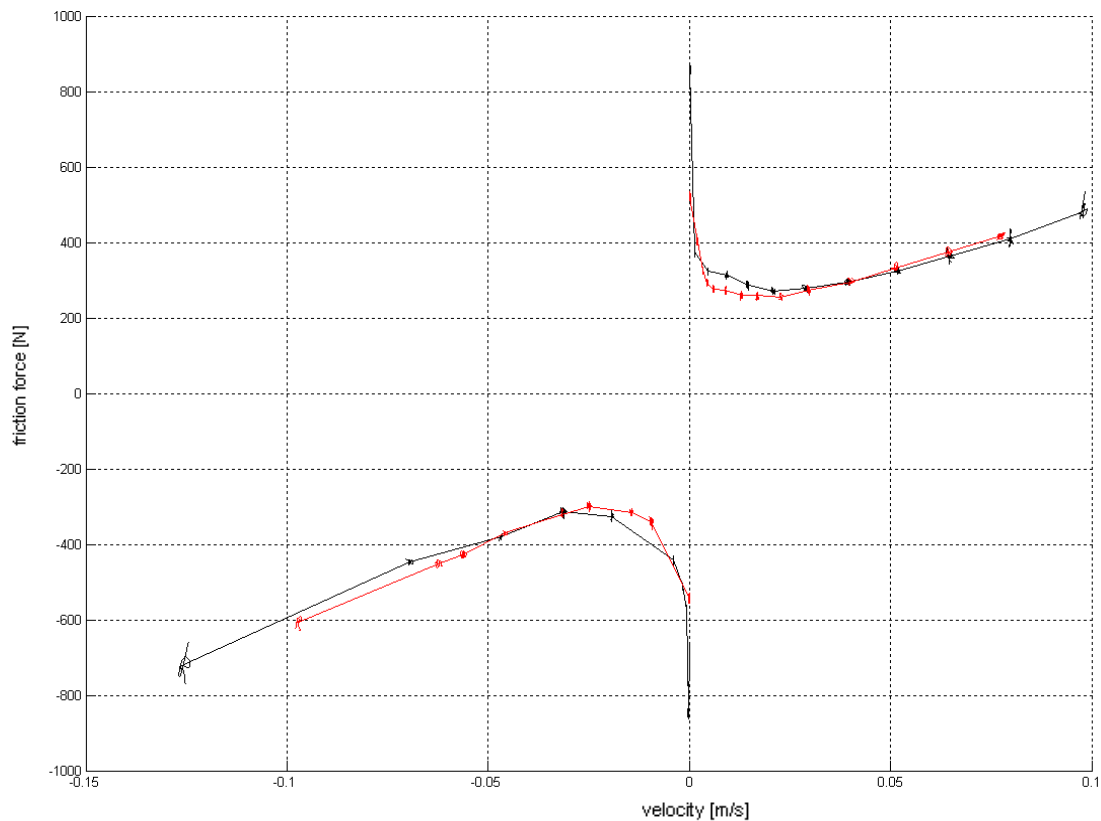


Figure 74: Comparison between friction force with variation in pressure supply

The nearly identical friction curve of varying loads is depicted in Figure 75:

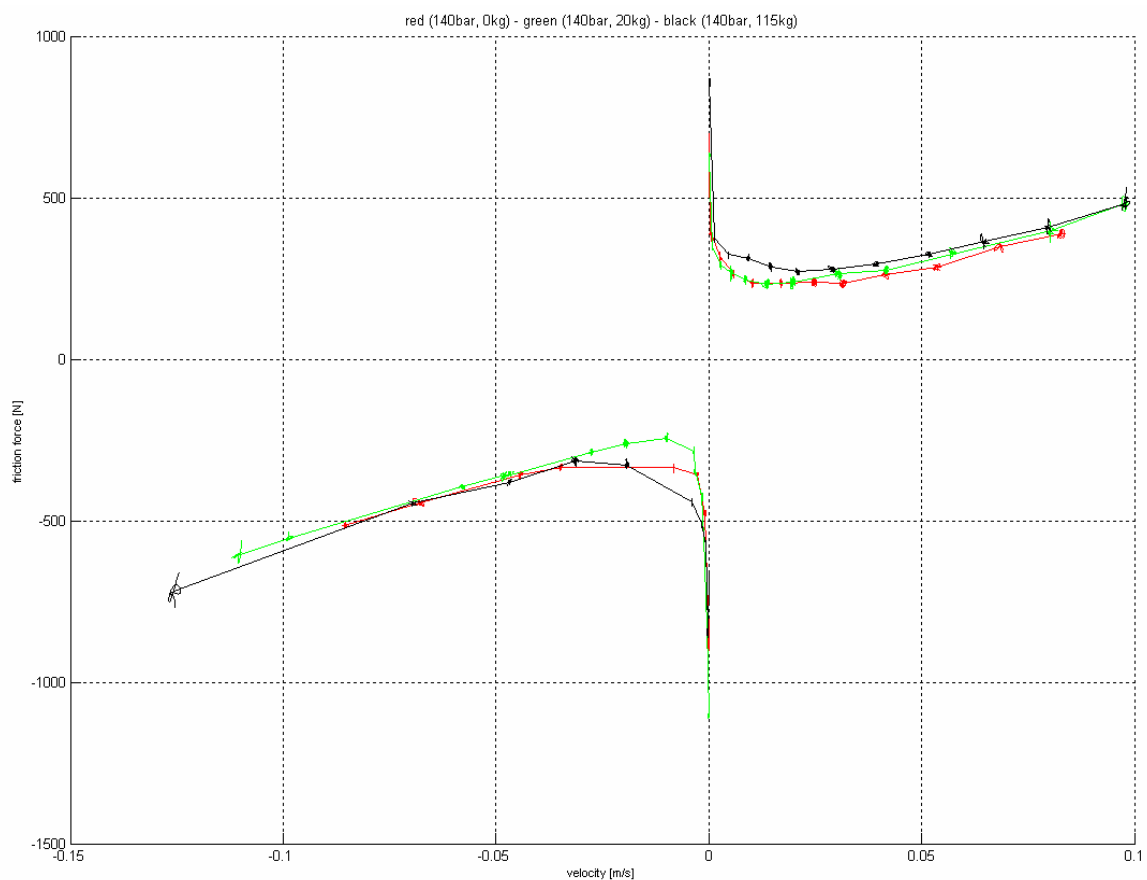


Figure 75: Comparison between friction force with variation in load

In Figure 75 the black curve indicates the friction force when carrying a load of 115 kg. The red curve represents a mass of 20 kg whereas the green curve shows the friction with no external loads. It is obvious that no load leads to the least friction force inside of the cylinders. The maximum friction appears apparently when carrying the maximum load, most notably in the region of slow velocities, but still the deviation in friction force is quite little.

The results from this chapter allow us to neglect the influence of external loads or pressure differences in real-world conditions. This assumption is very useful for our further simulations in MATLAB since we do not need to consider these environmental parameters.

6 Control of the crane

6.1 Control task

Joysticks have replaced the traditional mechanical control lever in nearly all modern hydraulic control systems. Today's forestry cranes are controlled predominantly by two joysticks that are mounted on an operating panel inside of the vehicle cab. The joysticks are two-dimensional having two axes of movement and some buttons for additional operations such as gripper control. Depending on the deflection of the joystick lever a corresponding input signal will be fed to the spools of the valve block. This generates the flow that acts on the hydraulic cylinders. Hence, the joystick movement directly controls the cylinder force and thus the velocity of the joint rotation, but the operator has to be very skilled in order to drive the crane-tip to its desired position. A possible joystick set-up of this common control principle is shown in Figure 76.

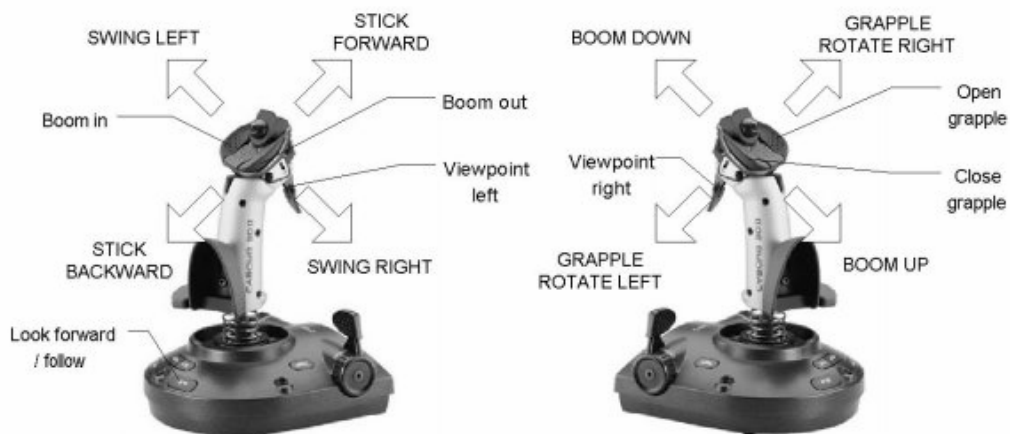


Figure 76: Possible arrangement for a two-joystick control of the crane-tip

This control method seems to be rather complicated which gives us motivation to simplify the control in order to facilitate the control operations for the driver. A more sophisticated control method might be to use a single joystick to control herewith the direction of the crane-tip in the xz -plane as illustrated in Figure 77.

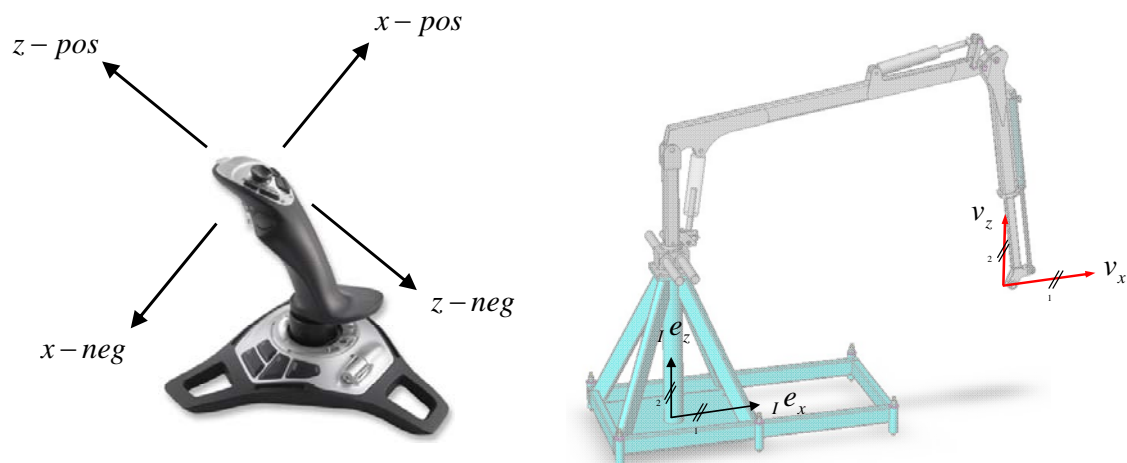


Figure 77: Possible arrangement for a single joystick control of the crane-tip

That means the direction of the speed of the end-effector (the gripper) follows the joystick command and if you release it, the crane simply stops moving. Hence, the joystick input will be used as a target-value for the desired speed of the crane-tip and not of the hydraulic cylinders. The output from the controller then feeds the corresponding current into the valves in order to keep the cylinders at a necessary speed that is required to fulfill the specified crane-tip trajectory.

During forestry work, this type of control might also require a second joystick but in comparison to control methods nowadays, it will be used only for rotational control about the 1st swivel-joint to determine the xz – plane. However, this configuration simplifies the learning task for humans, making it unnecessary to coordinate both hands in a complex pattern. Moreover this arrangement is likely to reduce strain injuries while increasing the efficiency of the main work. A first suggestion for this control is given in [9], but still there are no forestry machines in use that adapted this control principle by now.

The following chapter describes a two-dimensional control approach in the common xz – plane. Other solutions, including a full three-dimensional crane-tip control in the xyz – space will be developed in the near future within the department of Applied Physics and Electronics at Umeå University, Sweden.

6.2 Inverse joint control

In this section we will formulate an adequate control algorithm that allows us to control the crane-tip in a Cartesian xz – frame.

The essential approach to the above described control system is to emit a new target value, a so called set-point for the position of the crane-tip. The set-point calculation is done periodically at each sample, using the joystick input for the determination of the velocity of the crane-tip in x – and z – direction. The so called point-to-point calculation is a comparably simple method that enables us to calculate the new coordinates of the crane-tip position rather quick and straight-forward. A typical sequence of sample values and its effect on the corresponding velocity is given in Figure 78.

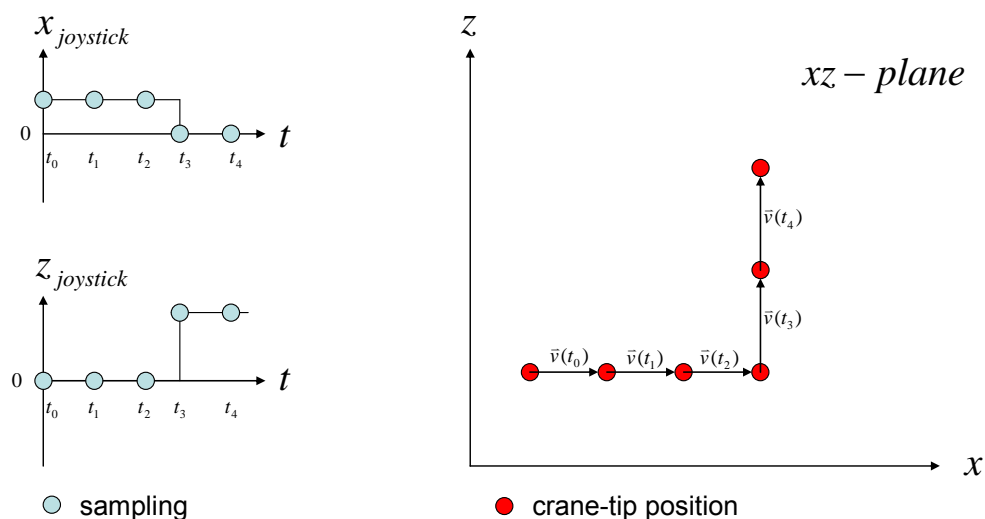


Figure 78: Sampling sequence of set-points for crane-tip velocity

One can notice that the joystick deflection directly, or rather at the next sampling, determines the desired velocity of the crane-tip. It is done as the controller permanently calculates the

relative speed between the cylinders. This is the main difference to the traditional control that uses the joystick input for controlling the hydraulic cylinders and thus moving the crane-tip circularly in proportion to the angular velocity about each joint.

We used a PID control for control purposes. It is described in the following section.

6.2.1 PID control

We approach the described control problem by applying ordinary PID-controllers to every joint. The PID-control uses the input signal from the joystick and transforms the joystick values into a corresponding crane-tip velocity predetermined by the operator. In accordance with the sampling period, the trajectory of the crane-tip can be achieved.

In chapter 3.1.2 we derived the inverse crane kinematics that describes how to calculate the joint angles for an arbitrary crane-tip position within the working area. The appropriate algorithm can now be used for the transformation of the corresponding joint angles that are necessary to reach the newly-calculated position of the crane-tip. In chapter 3.1.2.2 we have also found out that the joint angles are almost linearly proportional to the cylinder extension with a slight variation near the endpoints. For controlling the crane-tip we could make use of this linearity and just apply a simple linear equation to calculate the required cylinder length. However, we begin the programming with the non-linear relationship between the piston position and the joint angles and come back to a linear control when processing time seems to be immoderate.

For a start we know in which direction the cylinder piston has to move according to the predetermined cylinder lengths. A more accurate control regarding the exact crane-tip trajectory will be achieved by a proper adjustment of the PID-elements. The traditional PID-control is well-known as a discrete expression given by the equation

$$u = k_p e_t + k_i \sum_{j=0}^{\infty} e_{t-j} + k_d \frac{e_t - e_{t-1}}{T} \quad (128)$$

with k_p being the proportional gain, k_i the integral gain and k_d the derivative gain. The control error e_t results from the deviation between the real crane-tip coordinates given by the sensor signals and the desired coordinates that are calculated by the control system. The index in the control error denotes the sampling time, meaning that e_{t-1} is the error of the previous sampling to e_t . The length of time of a sampling period is given by T and finally the resulting control signal to trigger the valves is termed u .

This control seems to be the most common control but since we have limited control signals we probably encounter wind-up effects of the integral part, meaning that the term $\sum_{j=0}^{\infty} e_{t-j}$ continues to integrate indefinitely. This might end up in high control inputs even though the control error is low. Inevitably the discrete control will lead to inadequate results. We can avoid the wind-up problem by rewriting equation 128 into its differential form:

$$\Delta u = u_t - u_{t-1} = k_p (e_t - e_{t-1}) + k_i e_t + k_d (e_t + e_{t-2}) \quad (129)$$

where Δu is the difference of the control output between u_{t-1} and u_t .

The present control output is then defined by the sum of the previous control output and the differential output of equation 129. This allows for limiting the control output to

$$u_t = \left(u_{t-1} + \Delta u \right) \Big|_{\min}^{\max}, \quad (130)$$

where $\Big|_{\min}^{\max}$ denotes the range of possible control values within the predefined boundaries.

A possible *MATLAB*-code for the described differential PID-control of a single cylinder is given in Figure 79:

```

*****
% control cylinder 1
% *****
c1.K_p = 1; % proportional gain
c1.K_d = 0.01; % derivative gain
c1.K_i = 0.0001; % integral gain

c1.e_2 = c1.e_1; % error t_-2
c1.e_1 = c1.e; % error t_-1
c1.e = alpha_d - x(1); % error

c1.d_u = c1.K_p * (c1.e - c1.e_1) + c1.K_i * c1.e + c1.K_d * (c1.e - 2 * c1.e_1 +
c1.e_2); % differential control force
c1.u = c1.u + c1.d_u; % control force
c1.u = sign(c1.u) * min(abs([x_s_max; c1.u])); % limit control input
c1.i = 1 * c1.u; % input to spool

```

Figure 79: PID-control implementation in *MATLAB*

When operating the crane, these equations will be solved on-line in the crane's main control computer. On the basis of *MATLAB* simulations it turned out that the data processing of the control values seemed to be rather slow, probably due to limited CPU-power and lacking memory. This problem was mainly related to the floating point calculation of the inverse kinematics. It is obvious that the complex correlation of the torque link is a crucial factor for a long processing time. Future works should focus on optimizing the code to a greater extent in order to speed up the data processing of the crane control. Besides, the PID gains have to be adjusted in a proper way to suit the real-world applications of the crane. In this work the PID control was configured only to control the crane-tip in the simulation mode of *MATLAB*.

6.2.2 Control algorithm

Within this work, the main goal of a control algorithm was to simulate the behaviour of the crane in the *MATLAB* environment using a large number of variations including geometrical modifications and other parameter changes. The algorithm should be used later on for further modifying the control while running the algorithm online in a real-world environment.

The present algorithm is called within the m-file *main.m* during each integration step. Its basic steps are listed below in.

- 1) If time is below new sampling interval, leave algorithm
- 2) Measure the current joint angles α , β and the extension of the telescopic beam x_3
- 3) Read the joystick values u_x and u_z

- 4) Transform the joystick input into a corresponding crane-tip velocity $v_{x,joy} = k \cdot u_x$,
 $v_{z,joy} = k \cdot u_z$ respectively
- 5) Determine the new crane-tip coordinates by means of equations
 $x = x_{old} + \Delta x = x_{old} + v_{x,joy} T_{Sample}$
 $z = z_{old} + \Delta z = z_{old} + v_{z,joy} T_{Sample}$
- 6) Limit x and z according to working area
- 7) Do Loop of inverse kinematics with varying telescope extensions x_3
- 8) Calculate penalty function (see 6.2.3)
- 9) Apply inverse kinematics to determine desired joint angles α_d and β_d
- 10) Determine if new configuration is better than previous ones (penalty function)
- 11) End Loop of inverse kinematics
- 12) Overwrite control error e_{t2} with last error e_{t1}
- 13) Overwrite control error e_{t1} with present error e_t (e_α and e_β)
- 14) Calculate new control errors from the difference $e_\alpha = \alpha_d - \alpha$ and $e_\beta = \beta_d - \beta$
- 15) Save errors e_α and e_β in e_t
- 16) Apply equation 129 to calculate the additional control input
- 17) Apply equation 130 to calculate the new control input using control boundaries
- 18) Emit new control input to the valves
- 19) Go to Step 1

Table 6: Control algorithm

Besides the limitation of the working area (step 6) and the implementation of the penalty function (step 8), all other algorithm steps are represented in the attached m-file *main.m*. However, the missing steps are described in the next chapter for further modifications.

6.2.3 Optimization

The algorithm in Table 6 is based on the described inverse kinematics problem but also includes variations in length of the telescopic beam according to a penalty function. This function is not implemented in the attached *MATLAB* code but it should be designed in further studies to vary the extension length of the 3rd cylinder in a loop while calculating the best-angle configuration for the other two cylinders.

The overall aim of a penalty function is to determine the best cylinder configuration, aiming at limitation of crane-tip coordinates (working range) and avoidance of large changes in joint angles. This is explicitly done by testing several values of the telescopic extension x_3 and

selecting the configuration with lowest penalty p afterwards.

A suitable penalty function is given in [9]:

$$\begin{aligned}
 p(\alpha, \beta, x_3, \alpha_d, \beta_d, x_{3,d}) = & \\
 w_0 \cdot \text{outsiderange} + & \dots \\
 w_1(\alpha - \alpha_d)^2 + w_2(\beta - \beta_d)^2 + w_3(x_3 - x_{3,d})^2 + & \dots \\
 w_4(\alpha - \bar{\alpha})^2 + w_5(\beta - \bar{\beta})^2 + w_6(x_3 - \bar{x}_3)^2 &
 \end{aligned} \tag{131}$$

On the right-hand side of equation 131, the first term penalizes the crane-tip coordinates outside the accessible working range including an arbitrary factor w_0 . The factors w_1 , w_2 and w_3 of the 2nd term limit high joint angles requiring unachievable cylinder speed. Furthermore one should attempt to keep the pistons in the middle of each cylinder, avoiding the risk of new crane reconfiguration (due to maximum retraction / extension length) which might end up in large errors. For this purpose, the notations $\bar{\alpha}$, $\bar{\beta}$ and \bar{x}_3 are used as being the middle-value of the nominal working range. Hence, the terms referred to the factors w_4 , w_5 and w_6 will force the cylinder to strive into their recommended center position.

Equation 131 can be extended at will considering new optimization methods. Future works on the topic of crane control should implement this penalty function in the present *MATLAB* code.

6.3 Performance of crane model with PID-control

When running the animation of the crane in *MATLAB*, quality of the crane control has a huge influence on good performance. In order to test the implemented PID-control, we simulated several control tasks with the corresponding *MATLAB* file *animation_crane.m*.

In this special case we applied vertical control with the control parameters $joy_{ver} = 0.5$ and $joy_{hor} = 0$. Then the simulation was run five seconds in order to investigate the crane's trajectory beginning at initial conditions for the joint configuration $\alpha = 100^\circ$ and $\beta = 100^\circ$. Since we did not reset the initial control conditions within these five seconds, this type of control should force the gripper to follow a path parallel to the x -axis. Consequently it should be characterized by the same z -coordinates. From Figure 80 and Figure 81 one can clearly notice the expected upward movement of the crane tip, however we also want to figure out if the gripper has deviated from its straight vertical path. Therefore we have created a chart that represents the trajectory of the crane tip in both x - and z -axis (see Figure 82).

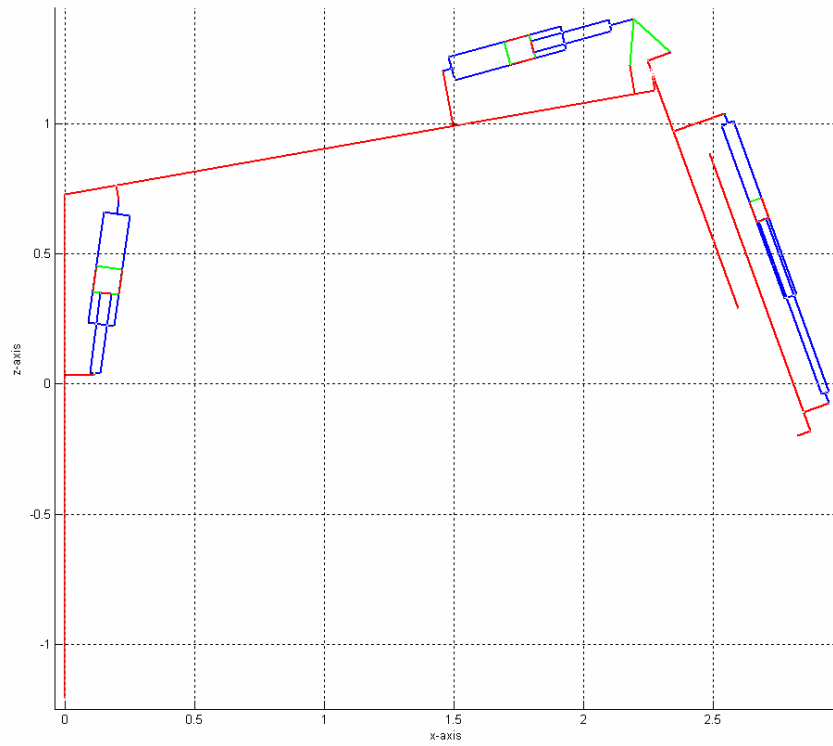


Figure 80: Vertical control – initial configuration

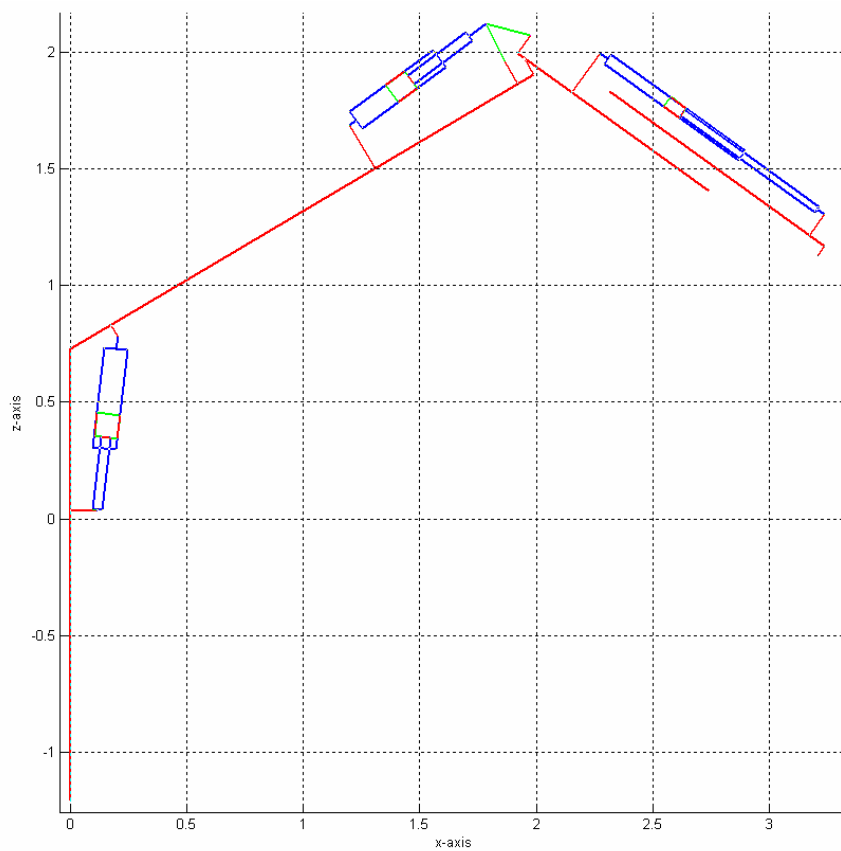


Figure 81: Vertical control – configuration after 5 seconds

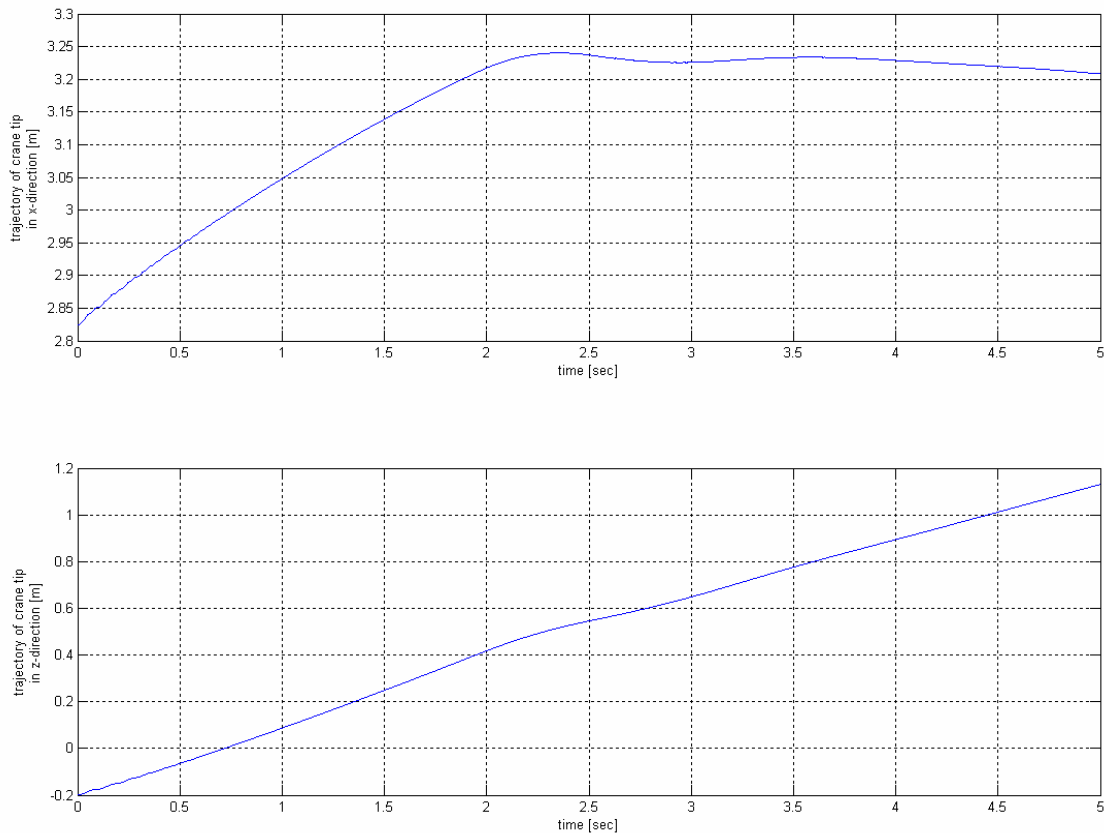


Figure 82: Trajectory path of the crane tip with vertical control

Figure 82 indicates that the crane tip almost follows a linear path in z-axis. Starting at $z = -0.2m$ the crane tip moves with a gradient of $\frac{dz}{dt} \approx 0.25 \frac{m}{s}$ and reaches $z = 1.1m$ after five seconds. However, the crane-tip also moves in x-direction, most notably in the beginning of the control task. Obviously the reason is the gravitational force of the crane referring the first joint. Here the cylinder can't build up the necessary force that quickly. This time delay should be further reduced by adjusting the control coefficients.

In our second test we ran the simulation with opposite control, namely a horizontal control task with the control parameters $joy_{ver} = 0$ and $joy_{hor} = -0.5$. The result of the animation can be seen in Figure 83 and Figure 84. The crane tip moves straight to the left (approximately with $\frac{dx}{dt} \approx -0.3 \frac{m}{s}$) and finally ends up in the same position on the z-axis.

However, if we look closer to the trajectory in z-direction, we notice that in between motion, the crane tip has deviated from its initial z-position $z = -0.2m$ to $z = -0.6m$ after three seconds. In this special case the cylinders can build up the pressure fast enough to force the crane tip almost in its initial level on the z-axis ($z = -0.3m$). In Figure 85 the motions for both x-axis and z-axis are depicted.

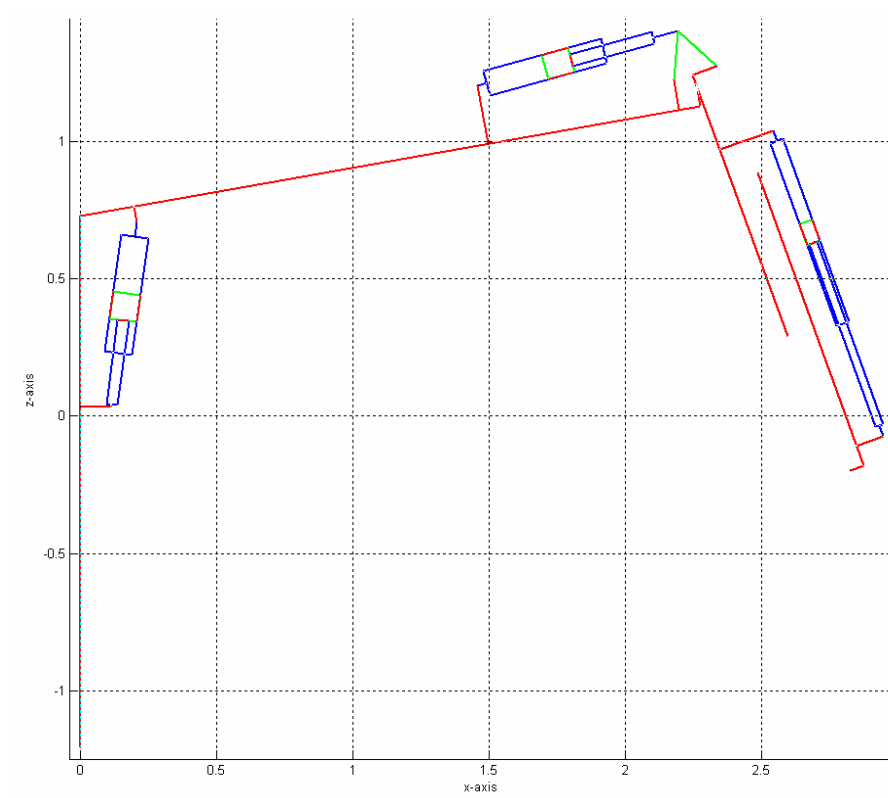


Figure 83: Horizontal control – initial configuration

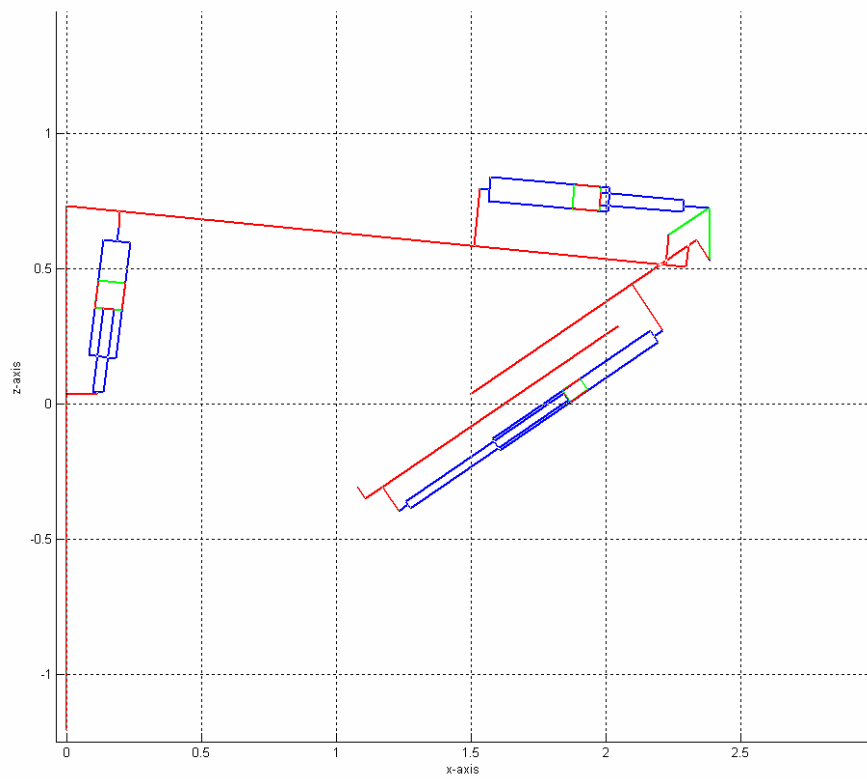


Figure 84: Horizontal control – configuration after 5 seconds

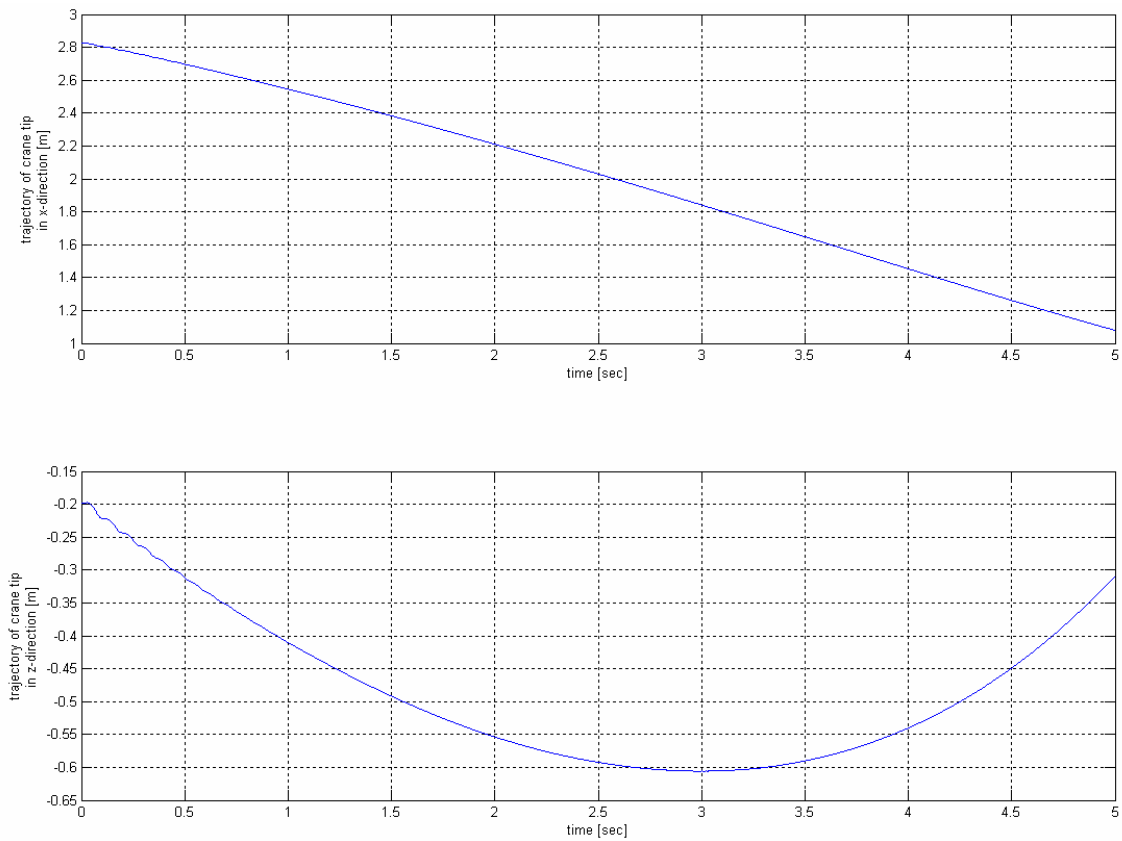


Figure 85: Trajectory path of the crane tip with horizontal control

The preceding simulations gave us a useful indication that generally the control task operates quite well. Motion control was responded by a corresponding movement in the desired direction. However we have noticed that gravity can lead to a deviation at the beginning of each motion. Once the cylinders have compensated these forces, motion control can be achieved in a good way as seen in Figure 85. In forthcoming projects one should further optimize the control parameters efficiently for its desired application.

7 Crane modelling in *MATLAB*

Crane modelling was an essential topic during the making of this thesis work. We started the work with a basic cylinder model and extended it to a hydraulic model including valve control. Simultaneously we approached the crane dynamics by creating a simple model of a two-link multi-body system and enhanced it step by step to its present degree.

In this chapter we begin with the formulism of the complete set of state space equations that have been derived earlier during this work. It is the essential part of the program codes that have been written in *MATLAB R 2007a*. The program code is divided into several sections. In 7.2 the main program is presented, including the crane kinematics and dynamics, the dynamics of the hydraulic system and the control algorithm. The crane dimensions and the complete coordinates of the *SolidWorks* model are given in chapter 7.3. The code for plotting the charts that depict the gradient of the generalized coordinates α , β and x_3 is presented in the *MATLAB* code 'PLOT CHARTS' in chapter 0. Here, one can also find the sub-elements that are needed to call the command for the crane animation.

7.1 Complete set of state space equations

We will now assembly the previously derived parts to a complete model, which means that the mechanical and the hydraulic model will be connected. In order to investigate the correlation between the different parts, one has to perform the calculations by running the corresponding *MATLAB* files from the attached CD. In this section we will not show the relationships in detail because of the many variables and large expressions in the state vector. However, for simulation purposes it is not necessary to do the entire calculation in advance.

The mechanical model was represented in chapter 3, its equation of motion was then derived in terms of the generalized coordinates q . In chapter 4 the hydraulic model was discussed in detail. From this emanates both the equation of motion for the valve spool y_{34} as well as the gradient of the cylinder pressures y_{56} . The latter expression is linked between the hydraulics and the mechanics as the piston stroke of each cylinder is directly related to the joint angles, namely the generalized coordinates. The seventh state of each cylinder part-system results from the system state of dynamic cylinder friction. This state describes the deflection of the surfaces in contact, in this work it was termed z . The set of state space equations can then be written as:

$$\begin{bmatrix} \dot{y}_1 \\ \dot{y}_2 \end{bmatrix} = \begin{bmatrix} y_2 \\ \ddot{q} \end{bmatrix}$$

$$\begin{bmatrix} \dot{y}_3 \\ \dot{y}_4 \end{bmatrix} = \begin{bmatrix} y_4 \\ -\omega_n^2 y_3 - 2\zeta\omega_n y_4 + \omega_n^2 u(t) \end{bmatrix}$$

$$\begin{bmatrix} \dot{y}_5 \\ \dot{y}_6 \end{bmatrix} = \begin{bmatrix} \frac{E_{oil}}{V_1} \left(q_1 + q_{int} - A_1 \frac{x_p}{dt} \right) \\ -\frac{E_{oil}}{V_2} \left(q_2 + q_{int} + q_{ext} - A_2 \frac{x_p}{dt} \right) \end{bmatrix}$$

$$[\dot{y}_7] = [\dot{z}]$$

We have now created the set of space state equations for a single part-model. In the same fashion we are then able to combine the three part-models to a complete crane model. This overall model is characterized by 21 states; however the following *m*-file *CRANE_MAIN* does not include the friction state as we adapted the static friction model for reasons of better performance.

7.2 MATLAB-code 'CRANE_MAIN'

This section represents the main *MATLAB*-code. It is divided into two basic parts, the main function defining the crane dynamics and the ode-function in which the hydraulic flow is defined. In turn, the hydraulic is split into several sub-sections, including valve control, hydraulic flow and cylinder friction. At the end of this *m*-file the derivative of the state vector is calculated.

```
function CRANE_MAIN()

% Mathematical model of the crane in x-z-plane
% 1st part: mechanical system (main)
% 2nd part: hydraulic system (ode)

clear all
close all
clf
clc
tic

global c1 c2 c3 l0 l1 l2 l3 l4 % cylinder and link properties
global t_step p_s p_0 C_0 k E_max p_max x_s_max C_1 C_2 F_c F_s v_s k_v w_n B p_tr
p_tr_min p_tr_max rho % general properties
global joy % control inputs

% generalized vectors
% *****
syms alph bet x3 alph_p bet_p x3_p % generalized coordinates
syms f1 f2 f3 % generalized forces (resulting cylinder forces)
q = [alph; bet; x3]; % (3)
q_p = [alph_p; bet_p; x3_p];

w_alpha = [0; alph_p; 0]; % angular velocity alpha
w_beta = [0; bet_p; 0]; % angular velocity beta
I_w_alpha = w_alpha; % angular velocity alpha in inertia frame
I_w_beta = w_alpha + w_beta; % angular velocity beta in inertia frame
% *****

% gravitation vector
% *****
g = 9.81; % gravitational acceleration [m/s^2]
I_g = [0; 0; -g];
% *****

% control input
% *****
joy.hor = 0; % horizontal axis -0.5 = left, 0 = stop, 0.5 = right [m/s]
joy.ver = 0.5; % vertical axis -0.5 = down, 0 = stop, 0.5 = up [m/s]
joy.t_samp = 5; % sampling interval [sec]
joy.t_low = 0; % initial time minimum [sec]
% *****

% crane parameters
% *****
[par] = dimension;
l0 = par{1}; % tripod
l1 = par{2}; % link 1
l2 = par{3}; % link 2
l3 = par{4}; % link 3
```

```

l4 = par{5}; % link 4
c1 = par{6}; % torque link
c1 = par{7}; % cylinder 1
c2 = par{8}; % cylinder 2
c3 = par{9}; % cylinder 3
% *****

% general properties
% *****
% fluid *****
rho = 1000; % oil density [kg/m3]
E_max = 1e9; % maximum bulk modulus of oil [Pa]
C_1 = 90; % bulk modulus coefficient 1 [-]
C_2 = 3; % bulk modulus coefficient 2 [-]
% pump
p_s = 140e5; % supply pressure of the pump [Pa]
p_0 = 0; % atmosphere pressure of the tank [Pa]
p_max = 200e5; % maximum pressure [Pa]
% cylinder *****
F_c = 100; % coulomb friction [N]
F_s = 750; % static friction (stiction) [N]
v_s = 0.005; % stribek velocity [m/s]
k_v = 3500; % viscous friction coefficient [Ns/m]
mu = 0.6; % friction coefficient of cylinder gaskets [-]
k = 5e6; % spring stiffness at cylinder floor [N/m] (limitation of cylinder stroke)
% spool *****
x_s_max = 0.05; % maximum spool stroke [m]
w_n = 2 * pi * 161.2; % natural frequency of the valve spool [1/s]
B = 0.481; % damping factor of the valve spool[-]
p_tr = 3e5; % (63) transition pressure corresponding to Reynolds transition [Pa]
p_tr_min = 2e5; % (63) lower threshold for transition region [Pa]
p_tr_max = 4e5; % (63) upper threshold for transition region [Pa]
Q_N = 0.0001; % nominal flow [m3/s] (valve characteristic)
p_n = 150e5; % nominal pressure drop [Pa] (valve characteristic)
C_0 = Q_N / (x_s_max * sqrt(0.5 * p_n)); % discharge coefficient [sqrt(m5/kg)]
% *****

% cylinder 1
% *****
c1.A_1 = power(c1.d_c,2) * pi / 4; % area chamber 1 [m2]
c1.A_2 = c1.A_1 - (power(c1.d_r,2) * pi / 4); % area chamber 2 [m2]
c1.A_0 = power(c1.d_0,2) * pi / 4; % area dead zone [m2]
c1.V_0d1 = c1.l_0 * c1.A_0; % dead volume chamber 1 [m3]
c1.V_0d2 = c1.l_0 * c1.A_0; % dead volume chamber 2 [m3]
c1.V_01 = c1.V_0d1 + c1.A_1*(c1.l_c-c1.l_p)/2; % (84) volume of oil in chamber 1 at x
= 0 [m3]
c1.V_02 = c1.V_0d2 + c1.A_2*(c1.l_c-c1.l_p)/2; % (85) volume of oil in chamber 2 at x
= 0 [m3]
c1.l_k = c1.l_c/20; % spring position from cylinder end [m]
c1.k_int = pi * (c1.d_c/2+c1.r_c) * power(c1.r_c,3) / (6*mu*c1.l_p); % (99) internal
leakage factor [m3/kg]
c1.k_ext = pi * (c1.d_r/2+c1.r_c) * power(c1.r_c,3) / (6*mu*c1.l_cw); % (99) external
leakage factor [m3/kg]
% *****

% cylinder 2
% *****
c2.A_1 = power(c2.d_c,2) * pi / 4; % area chamber 1 [m2]
c2.A_2 = c2.A_1 - (power(c2.d_r,2) * pi / 4); % area chamber 2 [m2]
c2.A_0 = power(c2.d_0,2) * pi / 4; % area dead zone [m2]
c2.V_0d1 = 0.02 * c2.A_0; % dead volume chamber 1 [m3]
c2.V_0d2 = 0.02 * c2.A_0; % dead volume chamber 2 [m3]
c2.V_01 = c2.V_0d1 + c2.A_1 * (c2.l_c - c2.l_p) / 2; % (84) volume of oil in chamber 1
at x = 0 [m3]
c2.V_02 = c2.V_0d2 + c2.A_2 * (c2.l_c - c2.l_p) / 2; % (85) volume of oil in chamber 2
at x = 0 [m3]
c2.l_k = c2.l_c/20; % spring position from floor [m]
c2.k_int = pi * (c2.d_c / 2 + c2.r_c) * power(c2.r_c,3) / (6*mu*c2.l_p); % (99)
internal leakage factor [m3/kg]
c2.k_ext = pi * (c2.d_r / 2 + c2.r_c) * power(c2.r_c,3) / (6*mu*c2.l_cw); % (99)
external leakage factor [m3/kg]
% *****

% cylinder 3

```

```

% *****
c3.A_1 = power(c3.d_c,2) * pi / 4; % area chamber 1 [m2]
c3.A_2 = c3.A_1 - (power(c3.d_r,2) * pi / 4); % area chamber 2 [m2]
c3.A_0 = power(c3.d_0,2) * pi / 4; % area dead zone [m2]
c3.V_0d1 = 0.02 * c3.A_0 * pi / 4; % dead volume chamber 1 [m3]
c3.V_0d2 = 0.02 * c3.A_0 * pi / 4; % dead volume chamber 2 [m3]
c3.V_01 = c3.V_0d1 + c3.A_1*(c3.l_c-c3.l_p)/2; % (84) volume of oil in chamber 1 at x
= 0 [m3]
c3.V_02 = c3.V_0d2 + c3.A_2*(c3.l_c-c3.l_p)/2; % (85) volume of oil in chamber 2 at x
= 0 [m3]
c3.l_k = c3.l_c/20; % spring position from floor [m]
c3.k_int = pi * (c3.d_c/2+c3.r_c) * power(c3.r_c,3) / (6*mu*c3.l_p); % (99) internal
leakage factor [m3/kg]
c3.k_ext = pi * (c3.d_r/2+c3.r_c) * power(c3.r_c,3) / (6*mu*c3.l_cw); % (99) external
leakage factor [m3/kg]
c3.l = (c3.l_c + c3.l_p) / 2 + c3.l_r + x3 + c3.o_s + c3.o_e; % (2) total lenght of
cylinder [m]
% *****

% slope angle of the torque link
% *****
cl.l1 = norm(cl.r1); % length of torque link 1 [m]
cl.l2 = norm(cl.r2); % length of torque link 2 [m]
cl.tetal = 2 * pi - bet - pi / 2 + l3.phi + l2.phi; % (17) angle lower closed loop
l2.p4_p5 and l3.p2 [rad]
cl.tl_t3 = sqrt(l2.p4_p5' * l2.p4_p5 + l3.p2' * l3.p2 - 2 * norm(l2.p4_p5) *
norm(l3.p2) * cos(cl.tetal)); % (18) distance between closed loop fix in link 2 and 3
[m]
cl.teta2 = acos((cl.l1 * cl.l1 + cl.l2 * cl.l2 - cl.tl_t3 * cl.tl_t3) / (2 * cl.l1 *
cl.l2)); % (20) angle upper closed loop cl.l1 and cl.l2 [rad]
cl.teta2 = simplify(cl.teta2);
cl.fhandle_teta2 = sym_2_fun(cl.teta2,'alpha, bet');
cl.teta31 = asin(norm(l3.p2) / cl.tl_t3 * sin(cl.tetal)); % (21) angle between torque
link 1 and cl.tl_t3 [rad]
cl.teta32 = asin(cl.l2 / cl.tl_t3 * sin(cl.teta2)); % (22) angle between cl.tl_t3 and
l2.p4_p5 [rad]
cl.eps1 = cl.teta31 + cl.teta32 + l2.phi; % (24) angle between torque link 1 and
torque link 2
cl.eps1 = simplify(cl.eps1);
cl.fhandle_eps1 = sym_2_fun(cl.eps1,'alpha, bet');
% *****

% transformation matrices
% *****
A_IK1 = eye(3); % rotation around z-axis of link 1 (==0)
A_K1K2 = A_y(pi / 2 - alpha); % (4) rotation around y-axis of link 2 ! alpha' = pi / 2
- alpha !
A_K2K3 = A_y(pi - bet); % (5) rotation around y-axis of link 3 ! beta' = pi - beta !
A_K2_CL = A_y(-cl.eps1); % (26) rotation from torque link 1 to K2

A_IK2 = A_IK1 * A_K1K2; % (7) rotation matrix of K2 associated to initial frame
A_IK3 = A_IK1 * A_K1K2 * A_K2K3; % (8) rotation matrix of K2 associated to initial
frame
A_ICL = A_IK1 * A_K1K2 * A_K2_CL; % rotation matrix of torque frame associatred to
initial frame
% *****

% k-vectors in world frame
% *****
I_r_11_12 = A_IK1 * l1.p2; % link 1
I_r_21_25 = A_IK2 * l2.p5; % link 2
I_r_41_42 = A_IK3 * l4.p2; % link 4

I_r_11_lcg = A_IK1 * l1.cg; % center of gravity - link 1
I_r_21_2cg = A_IK2 * l2.cg; % center of gravity - link 2
I_r_31_3cg = A_IK3 * l3.cg; % center of gravity - link 3
I_r_41_4cg = A_IK3 * l4.cg; % center of gravity - link 4

I_r_11_13 = A_IK1 * l1.p3; % cylinder 1 - end
I_r_21_22 = A_IK2 * l2.p2; % cylinder 1 - start
I_r_21_23 = A_IK2 * l2.p3; % cylinder 2 - start
I_r_31_33 = A_IK3 * l3.p3; % cylinder 3 - start
I_r_31_42 = I_r_31_33 + A_IK3 * [c3.l;0;0]; % cylinder 3 - end

```

```

I_r_21_24 = A_IK2 * l2.p4; % joint 2 - link 2
I_r_24_c1 = A_ICL * c1.r1; % cylinder 2 - end

I_r_42_ct = A_IK3 * (- l4.p2 + l4.p1); % cylinder 1 end - crane tip
% *****

% 0-vectors in world frame
% *****
I_r_0_1cg = I_r_11_1cg; % (30) center of gravity - link 1
I_r_0_2cg = I_r_11_12 + I_r_21_2cg; % (31) center of gravity - link 2
I_r_0_3cg = I_r_11_12 + I_r_21_25 + I_r_31_3cg; % (32) center of gravity - link 3
I_r_0_4cg = I_r_11_12 + I_r_21_25 + I_r_31_42 - I_r_41_42 + I_r_41_4cg; % (33) center
of gravity - link 4

I_r_0_13 = I_r_11_13; % cylinder 1 - end
I_r_0_22 = I_r_11_12 + I_r_21_22; % cylinder 1 - start
I_r_0_23 = I_r_11_12 + I_r_21_23; % cylinder 2 - start
I_r_0_c1 = I_r_11_12 + I_r_21_24 + I_r_24_c1; % cylinder 2 - end
I_r_0_33 = I_r_11_12 + I_r_21_25 + I_r_31_33; % cylinder 3 - start
I_r_0_42 = I_r_11_12 + I_r_21_25 + I_r_31_42; % cylinder 3 - end
I_r_0_ct = I_r_11_12 + I_r_21_25 + I_r_31_42 + I_r_42_ct; % (34) crane tip
% *****

% velocity of center of mass (r = r(q) --> i = 0)
% *****
I_v_0_1cg = jacobian(I_r_0_1cg,q)*q_p; % (36) velocity link 1
I_v_0_2cg = jacobian(I_r_0_2cg,q)*q_p; % (36) velocity link 2
I_v_0_3cg = jacobian(I_r_0_3cg,q)*q_p; % (36) velocity link 3
I_v_0_4cg = jacobian(I_r_0_4cg,q)*q_p; % (36) velocity link 4
% *****

% piston stroke 1
% *****
c1.r = A_IK1' * (I_r_0_22 - I_r_0_13); % cylinder vector in K1
c1.l = sqrt(c1.r(1) * c1.r(1) + c1.r(2) * c1.r(2) + c1.r(3) * c1.r(3)); % (1) total
length of cylinder (joint-2-joint)

c1.phi = atan(c1.r(1) / c1.r(3)); % (15) angle between cylinder and link
c1.phi = simplify(c1.phi);
c1.fhandle_phi = sym_2_fun(c1.phi, 'alph');

c1.x = c1.l - c1.l_r - c1.l_c / 2 - c1.l_p / 2 - c1.o_s - c1.o_e; % (2)/(40) extension
[m]
c1.x = simplify(c1.x);
c1.fhandle_x = sym_2_fun(c1.x, 'alph');

c1.v = jacobian(c1.x,q) * q_p; % velocity [m/s]
c1.v = simplify(c1.v);
c1.fhandle_v = sym_2_fun(c1.v, 'alph, alph_p');
% *****

% piston stroke 2
% *****
c2.r = l2.p4 + A_K2_CL * c1.r1 - l2.p3; % (41) cylinder vector in K2
c2.l = sqrt(c2.r(1) * c2.r(1) + c2.r(2) * c2.r(2) + c2.r(3) * c2.r(3)); % (1) total
length of cylinder (joint-2-joint)

c2.phi = atan(c2.r(3) / c2.r(1)); % (28) angle between cylinder and link (phi gets
negativ)
c2.phi = simplify(c2.phi);
c2.fhandle_phi = sym_2_fun(c2.phi, 'alph, bet');

c2.x = c2.l - c2.l_r - c2.l_c / 2 - c2.l_p / 2 - c2.o_s - c2.o_e; % (2)/(42) extension
[m]
c2.x = simplify(c2.x);
c2.fhandle_x = sym_2_fun(c2.x, 'alph, bet');

c2.v = jacobian(c2.x,q) * q_p; % velocity [m/s]
c2.v = simplify(c2.v);
c2.fhandle_v = sym_2_fun(c2.v, 'alph, alph_p, bet, bet_p');
% *****

```

```

% kinetic energy (translation)
% *****
T_k = (1/2) * l1.m * I_v_0_1cg.' * I_v_0_1cg +...
      (1/2) * l2.m * I_v_0_2cg.' * I_v_0_2cg +...
      (1/2) * l3.m * I_v_0_3cg.' * I_v_0_3cg +...
      (1/2) * l4.m * I_v_0_4cg.' * I_v_0_4cg; % (45/1)
% *****

% kinetic energy (rotation)
% *****
T_r = (1/2) * I_w_alpha.' * l2.I * I_w_alpha +...
      (1/2) * I_w_beta.' * l3.I * I_w_beta + ...
      (1/2) * I_w_beta.' * l4.I * I_w_beta; % (45/2)
% *****

% total kinetic energy
% *****
T = T_k + T_r; % (45)
% *****

% potential energy
% *****
V = l1.m * I_g' * I_r_0_1cg +...
    l2.m * I_g' * I_r_0_2cg +...
    l3.m * I_g' * I_r_0_3cg +...
    l4.m * I_g' * I_r_0_4cg; % (52)
% *****

% actuator forces
% *****
A_Ic1 = A_y(pi / 2 + c1.phi); % (16) rotation matrix from cylinder 1 to earth frame
A_Ic2 = A_IK2 * A_y(-c2.phi); % (29) rotation matrix from cylinder 2 to earth frame
A_Ic3 = A_IK3; % rotation matrix from cylinder 3 to earth frame

I_f_a1 = A_Ic1 * [f1;0;0]; % cylidner force vector 1
I_f_a2 = A_Ic2 * [f2;0;0]; % cylidner force vector 2
I_f_a3 = A_Ic3 * [f3;0;0]; % cylidner force vector 3
% *****

% non-potential forces
% *****
Q = jacobian(I_r_0_13,q).' * I_f_a1 - jacobian(I_r_0_22,q).' * I_f_a1 +...
    jacobian(I_r_0_c1,q).' * I_f_a2 - jacobian(I_r_0_23,q).' * I_f_a2 +...
    jacobian(I_r_0_42,q).' * I_f_a3 - jacobian(I_r_0_33,q).' * I_f_a3; % (54)
% *****

% derivation of Euler-Lagrange terms M & h
% *****
M = jacobian(jacobian(T,q_p).',q_p); % (41)
h = - jacobian(jacobian(T,q_p).',q) * q_p + jacobian(T,q).' - jacobian(V,q).' + Q; %
(53)
M = simplify(M);
h = simplify(h);
fhandle_M = sym_2_fun(M,'alph, bet, x3, f1, f2, f3');
fhandle_h = sym_2_fun(h,'alph, alph_p, bet, bet_p, x3, x3_p, f1, f2, f3');
% *****

% ode options
% *****
t_start = 0;
t_step = 0.001;
t_end = 0.5;

opt = odeset('OutputFcn',@odeplot,...
            'RelTol',1.e-1,... % Standard 1.e-3
            'AbsTol',1.e-1,... % Standard 1.e-6
            'OutputFcn',@odeplot);

```



```

x0 = [100*pi/180 0 0 0 0 0 100*pi/180 0 0 0 0 0 0 0 0 0 0]; % initial conditions
% *****

% ode call
% *****
[t,x] =
ode23(@odefunction,t_start:t_step:t_end,x0,opt,fhandle_M,fhandle_h,c1.fhandle_x,c2.fha
ndle_x,c1.fhandle_v,c2.fhandle_v);
% *****

% plot call
% *****
PLOT_CHARTS(t,x,c1,c2,c3,c1,l0,l1,l2,l3,l4,t_step,t_end)
% *****

% trajectory of the crane tip
% *****
for i = 1 : length(t)

    A_IK1 = eye(3);
    A_IK2 = A_IK1 * A_y(pi / 2 - x(i,1));
    A_IK3 = A_IK1 * A_y(pi / 2 - x(i,1)) * A_y(pi - x(i,7));

    ct(1:3,i) = A_IK1 * l1.p2 + ...
                A_IK2 * l2.p5 + ...
                A_IK3 * l3.p3 + ...
                A_IK3 * [c3.o_s + c3.l_c / 2 + x(i,13) + c3.l_p / 2 + c3.l_r +
c3.o_e;0;0] + ...
                A_IK3 * (l4.p1 - l4.p2);

end

figure
subplot(2,1,1)
plot(t',ct(1,:))
grid
xlabel('time [sec]')
ylabel({'trajectory of crane tip';'in x-direction [m]'})
subplot(2,1,2)
plot(t',ct(3,:))
grid
xlabel('time [sec]')
ylabel({'trajectory of crane tip';'in z-direction [m]'})
% *****

end

% *****
% -----END OF MAIN-----
% *****

function
dxdt=odefunction(t,x,M_function,h_function,x1_function,x2_function,v1_function,v2_func
tion)

    global c1 c2 c3 l1 l2 l3 l4 % cylinder and link properties
    global p_s p_0 C_0 k E_max p_max x_s_max C_1 C_2 F_c F_s v_s k_v w_n B p_tr p_tr_min
    p_tr_max rho % general properites
    global joy % control input
    global alpha_d beta_d x3_d % computation of generalized coordinates

% some definition of cylinder piston (x, v)
% *****
x1_real = x1_function(x(1));
v1_real = v1_function(x(1),x(2));
x2_real = x2_function(x(1),x(7));
v2_real = v2_function(x(1),x(2),x(7),x(8));
% *****

% crane control

```

```

% *****
if (t == 0) || ((t - joy.t_low) > joy.t_samp) % sampling criterion
joy.t_low = t; % reset of lower time

% position of the crane tip
A_IK1 = eye(3);
A_IK2 = A_IK1 * A_y(pi / 2 - x(1));
A_IK3 = A_IK1 * A_y(pi / 2 - x(1)) * A_y(pi - x(7));
ct = A_IK1 * l1.p2 + ... % link 1
    A_IK2 * l2.p5 + ... % link 2
    A_IK3 * l3.p3 + ... % link 3
    A_IK3 * [c3.o_s + c3.l_c / 2 + x(13) + c3.l_p / 2 + c3.l_r + c3.o_e;0;0] +
... % cylinder 3
    A_IK3 * (l4.p1 - l4.p2); % tele beam

% inverse kinematics
joy.delta = [joy.hor * joy.t_samp; 0; joy.ver * joy.t_samp]; % joystick input
ct_d = ct + joy.delta; % desired position of the crane tip [m]
x3_d = 0; % telescopic beam extension (will be varied ...)

l3.ct = l3.p3 + [c3.o_s + c3.l_c / 2 + x3_d + c3.l_p / 2 + c3.l_r + c3.o_e;0;0] +
(l4.p1 - l4.p2); % K3-vector from joint 3 to crane tip [m]
r1 = norm(l2.p5); % length of r1 [m]
r2 = norm(l3.ct); % length of r2 [m]
r_diag = ct_d - l1.p2; % (36) diagonal vector [m]

beta_d = acos((r1 * r1 + r2 * r2 - r_diag' * r_diag) / (2 * r1 * r2)); % (35)
desired angle beta related to joint axis [rad]
alpha_d = acos((l1.p2' * l1.p2 + r_diag' * r_diag - ct_d' * ct_d) / (2 *
norm(l1.p2) * norm(r_diag))) + acos((r1 * r1 + r_diag' * r_diag - r2 * r2) / (2 * r1 *
norm(r_diag))); % (37) desired angle alpha related to joint axis [rad]
alpha_d = alpha_d - atan(l2.p5(3) / l2.p5(1)); % (38) desired angle alpha related
to frame axis [rad]
beta_d = beta_d + atan(l2.p5(3) / l2.p5(1)) - atan(l3.ct(3) / l3.ct(1)); % (39)
desired angle beta related to frame axis [rad]

% text
disp(['sampling time = ',num2str(joy.t_low)])
disp(['ct (x) = ',num2str(ct(1))],[ 'ct_d (x) = ',num2str(ct_d(1))])
disp(['ct (z) = ',num2str(ct(3))],[ 'ct_d (z) = ',num2str(ct_d(3))])
disp(['alpha = ',num2str(x(1) * 180 / pi)],[ 'alpha_d = ',num2str(alpha_d * 180 /
pi)])
disp(['beta = ',num2str(x(7) * 180 / pi)],[ 'beta_d = ',num2str(beta_d * 180 /
pi)])
disp(' ')
end
% *****

% *****
% control cylinder 1
% *****
c1.K_p = 1; % proportional gain
c1.K_d = 0.01; % derivative gain
c1.K_i = 0.0001; % integral gain

c1.e_2 = c1.e_1; % error t_-2
c1.e_1 = c1.e; % error t_-1
c1.e = alpha_d - x(1); % error

c1.d_u = c1.K_p * (c1.e - c1.e_1) + c1.K_i * c1.e + c1.K_d * (c1.e - 2 * c1.e_1 +
c1.e_2); % differential control force
c1.u = c1.u + c1.d_u; % control force
c1.u = sign(c1.u) * min(abs([x_s_max; c1.u])); % limit control input
c1.i = 1 * c1.u; % input to spool
% *****
% control cylinder 2
% *****
c2.K_p = 1; % proportional gain
c2.K_d = 0.01; % derivative gain
c2.K_i = 0.005; % integral gain

c2.e_2 = c2.e_1; % error t_-2
c2.e_1 = c2.e; % error t_-1
c2.e = beta_d - x(7); % error

```

```

c2.d_u = c2.K_p * (c2.e - c2.e_1) + c2.K_i * c2.e + c2.K_d * (c2.e - 2 * c2.e_1 +
c2.e_2); % differential control force
c2.u = c2.u + c2.d_u; % control force
c2.u = sign(c2.u) * min(abs([x_s_max; c2.u])); % limit control input
c2.i = - 1 * c2.u; % input to spool
% *****
% control cylinder 3
% *****
c3.K_p = 1; % proportional gain
c3.K_d = 0.01; % derivative gain
c3.K_i = 0.005; % integral gain

c3.e_2 = c3.e_1; % error t_-2
c3.e_1 = c3.e; % error t_-1
c3.e = x3_d - x(13); % error

c3.d_u = c3.K_p * (c3.e - c3.e_1) + c3.K_i * c3.e + c3.K_d * (c3.e - 2 * c3.e_1 +
c3.e_2); % differential control force
c3.u = c3.u + c3.d_u; % control force
c3.u = sign(c3.u) * min(abs([x_s_max; c3.u])); % limit control input
c3.i = 1 * c3.u; % input to spool
% *****

% *****
% chamber flow cylinder 1
% *****
c1.dp1 = rho / 2 * (power((c1.A_1 / c1.A_0),2) - 1) * power(v1_real,2); % (104)
additional pressure chamber 1 (Bernoulli)
c1.dp2 = rho / 2 * (power((c1.A_2 / c1.A_0),2) - 1) * power(v1_real,2); % (104)
additional pressure chamber 2 (Bernoulli)
if x(5) >= 0 % positive flow x(5) = 0 redundant
    delta_p1 = p_s - (x(3) - c1.dp1);
    delta_p2 = (x(4) - c1.dp2) - p_0;
elseif x(5) < 0 % negative flow
    delta_p1 = (x(3) - c1.dp1) - p_0;
    delta_p2 = p_s - (x(4) - c1.dp2);
end
    if abs(delta_p1) >= p_tr_max % (66/67) turbulent flow
        c1.Q_1 = C_0 * x(5) * sign(delta_p1) * sqrt(abs(delta_p1)); % flow chamber 1
p_1==p_s
    elseif abs(delta_p1) < p_tr_min % (69/70) laminar flow
        c1.Q_1 = C_0 * x(5) * delta_p1 * (abs(delta_p1) / p_tr) / (2 * sqrt(p_tr)); %
factor '(3...' is between 2e-3 and 4e-3
    else % (74) transition range
        c1.Q_1 = abs((abs(delta_p1) - p_tr_min) / (p_tr_max - p_tr_min)) * ...
            C_0 * x(5) * sign(delta_p1) * sqrt(abs(delta_p1)) + ...
            (1 - abs((abs(delta_p1) - p_tr_min) / (p_tr_max - p_tr_min))) * ...
            C_0 * x(5) * delta_p1 * (abs(delta_p1) / p_tr) / (2 * sqrt(p_tr)); %
(69) transition flow
    end
    if abs(delta_p2) >= p_tr % (58/59) turbulent flow
        c1.Q_2 = C_0 * x(5) * sign(delta_p2) * sqrt(abs(delta_p2)); % flow chamber 2
p_2==p_0
    elseif abs(delta_p2) < p_tr % laminar flow
        c1.Q_2 = C_0 * x(5) * delta_p2 * (abs(delta_p2) / p_tr) / (2 * sqrt(p_tr));
    else % (74) transition range
        c1.Q_2 = abs((abs(delta_p2) - p_tr_min) / (p_tr_max - p_tr_min)) * ...
            C_0 * x(5) * sign(delta_p2) * sqrt(abs(delta_p2)) + ...
            (1 - abs((abs(delta_p2) - p_tr_min) / (p_tr_max - p_tr_min))) * ...
            C_0 * x(5) * delta_p2 * (abs(delta_p2) / p_tr) / (2 * sqrt(p_tr)); %
(69) transition flow
    end
c1.Q_int = c1.k_int * (x(3) - x(4)); % (97) internal leakage
c1.Q_ext = c1.k_ext * x(4); % (98) external leakage
% *****
% chamber flow cylinder 2
% *****
c2.dp1 = rho / 2 * (power((c2.A_1 / c2.A_0),2) - 1) * power(v2_real,2); % (104)
additional pressure chamber 1 (Bernoulli)
c2.dp2 = rho / 2 * (power((c2.A_2 / c2.A_0),2) - 1) * power(v2_real,2); % (104)
additional pressure chamber 2 (Bernoulli)
if x(11) >= 0 % positive flow x(11) = 0 redundant
    delta_p1 = p_s - (x(9) - c2.dp1);
    delta_p2 = (x(10) - c2.dp2) - p_0;
elseif x(11) < 0 % negative flow

```

```

    delta_p1 = (x(9) - c2.dp1) - p_0;
    delta_p2 = p_s - (x(10) - c2.dp2);
end
    if abs(delta_p1) >= p_tr % (66/67) turbulent flow
        c2.Q_1 = C_0 * x(11) * sign(delta_p1) * sqrt(abs(delta_p1)); % flow chamber 1
    p_1==p_s
    elseif abs(delta_p1) < p_tr % (69/70) laminar flow
        c2.Q_1 = C_0 * x(11) * delta_p1 * (abs(delta_p1) / p_tr) / (2 * sqrt(p_tr)); %
factor '(3...)' is between 2e-3 and 4e-3
    else % (74) transition range
        c2.Q_1 = abs((abs(delta_p1) - p_tr_min) / (p_tr_max - p_tr_min)) * ...
            C_0 * x(11) * sign(delta_p1) * sqrt(abs(delta_p1)) + ...
            (1 - abs((abs(delta_p1) - p_tr_min) / (p_tr_max - p_tr_min))) * ...
            C_0 * x(11) * delta_p1 * (abs(delta_p1) / p_tr) / (2 * sqrt(p_tr)); %
(69) transition flow
    end
    if abs(delta_p2) >= p_tr % (66/67) turbulent flow
        c2.Q_2 = C_0 * x(11) * sign(delta_p2) * sqrt(abs(delta_p2)); % flow chamber 2
    p_2==p_0
    elseif abs(delta_p2) < p_tr % (69/70) laminar flow
        c2.Q_2 = C_0 * x(11) * delta_p2 * (abs(delta_p2) / p_tr) / (2 * sqrt(p_tr));
    else % (74) transition range
        c2.Q_2 = abs((abs(delta_p2) - p_tr_min) / (p_tr_max - p_tr_min)) * ...
            C_0 * x(11) * sign(delta_p2) * sqrt(abs(delta_p2)) + ...
            (1 - abs((abs(delta_p2) - p_tr_min) / (p_tr_max - p_tr_min))) * ...
            C_0 * x(11) * delta_p2 * (abs(delta_p2) / p_tr) / (2 * sqrt(p_tr)); %
(69) transition flow
    end
    c2.Q_int = c2.k_int * (x(9) - x(10)); % (97) internal leakage
    c2.Q_ext = c2.k_ext * x(10); % (98) external leakage
% *****
% chamber flow cylinder 3
% *****
c3.dp1 = rho / 2 * (power((c3.A_1 / c3.A_0),2) - 1) * power(x(14),2); % (104)
additional pressure chamber 1 (Bernoulli)
c3.dp2 = rho / 2 * (power((c3.A_2 / c3.A_0),2) - 1) * power(x(14),2); % (104)
additional pressure chamber 2 (Bernoulli)
if x(17) >= 0 % positive flow x(17) = 0 redundant
    delta_p1 = p_s - (x(15) - c3.dp1);
    delta_p2 = (x(16) - c3.dp2) - p_s; % (68) regenerative valve
elseif x(17) < 0 % negative flow
    delta_p1 = (x(15) - c3.dp1) - p_0;
    delta_p2 = p_s - (x(16) - c3.dp2);
end
    if abs(delta_p1) >= p_tr % (66/67) turbulent flow
        c3.Q_1 = C_0 * x(17) * sign(delta_p1) * sqrt(abs(delta_p1)); % flow chamber 1
    p_1==p_s
    elseif abs(delta_p1) < p_tr % (69/70) laminar flow
        c3.Q_1 = C_0 * x(17) * delta_p1 * (abs(delta_p1) / p_tr) / (2 * sqrt(p_tr)); %
factor '(3...)' is between 2e-3 and 4e-3
    else % (74) transition range
        c3.Q_1 = abs((abs(delta_p1) - p_tr_min) / (p_tr_max - p_tr_min)) * ...
            C_0 * x(17) * sign(delta_p1) * sqrt(abs(delta_p1)) + ...
            (1 - abs((abs(delta_p1) - p_tr_min) / (p_tr_max - p_tr_min))) * ...
            C_0 * x(17) * delta_p1 * (abs(delta_p1) / p_tr) / (2 * sqrt(p_tr)); %
(69) transition flow
    end
    if abs(delta_p2) >= p_tr % (66/67) turbulent flow
        c3.Q_2 = C_0 * x(17) * sign(delta_p2) * sqrt(abs(delta_p2)); % flow chamber 2
    p_2==p_0
    elseif abs(delta_p2) < p_tr % (69/70) laminar flow
        c3.Q_2 = C_0 * x(17) * delta_p2 * (abs(delta_p2) / p_tr) / (2 * sqrt(p_tr));
    else % (74) transition range
        c3.Q_2 = abs((abs(delta_p2) - p_tr_min) / (p_tr_max - p_tr_min)) * ...
            C_0 * x(17) * sign(delta_p2) * sqrt(abs(delta_p2)) + ...
            (1 - abs((abs(delta_p2) - p_tr_min) / (p_tr_max - p_tr_min))) * ...
            C_0 * x(17) * delta_p2 * (abs(delta_p2) / p_tr) / (2 * sqrt(p_tr)); %
(69) transition flow
    end
    c3.Q_int = c3.k_int * (x(15) - x(16)); % (97) internal leakage
    c3.Q_ext = c3.k_ext * x(15); % (98) external leakage
% *****

% *****
% compressibility of oil cylinder 1

```

```

% *****
c1.E_1 = 0.5 * E_max * log10(C_1 * (abs(x(3)) / p_max) + C_2); % (96) bulk modulus of
oil [Pa]
c1.E_2 = 0.5 * E_max * log10(C_1 * (abs(x(4)) / p_max) + C_2); % (96) bulk modulus of
oil [Pa]
% *****
% compressibility of oil cylinder 2
% *****
c2.E_1 = 0.5 * E_max * log10(C_1 * (abs(x(9)) / p_max) + C_2); % (96) bulk modulus of
oil [Pa]
c2.E_2 = 0.5 * E_max * log10(C_1 * (abs(x(10)) / p_max) + C_2); % (96) bulk modulus of
oil [Pa]
% *****
% compressibility of oil cylinder 3
% *****
c3.E_1 = 0.5 * E_max * log10(C_1 * (abs(x(15)) / p_max) + C_2); % (96) bulk modulus
of oil [Pa]
c3.E_2 = 0.5 * E_max * log10(C_1 * (abs(x(16)) / p_max) + C_2); % (96) bulk modulus
of oil [Pa]
% *****

% *****
% chamber volumes cylinder 1
% *****
c1.V_1 = c1.V_01 + c1.A_1 * x1_real; % (86)
c1.V_2 = c1.V_02 - c1.A_2 * x1_real; % (87)
% *****
% chamber volumes cylinder 2
% *****
c2.V_1 = c2.V_01 + c2.A_1 * x2_real; % (86)
c2.V_2 = c2.V_02 - c2.A_2 * x2_real; % (87)
% *****
% chamber volumes cylinder 3
% *****
c3.V_1 = c3.V_01 + c3.A_1 * x(13); % (86)
c3.V_2 = c3.V_02 - c3.A_2 * x(13); % (87)
% *****

% *****
% friction force cylinder 1
% *****
c1.F_f = k_v * v1_real + sign(v1_real) * (F_c + F_s * exp(-abs(v1_real) / v_s)); %
friction force [N]
% *****
% friction force cylinder 2
% *****
c2.F_f = k_v * v2_real + sign(v2_real) * (F_c + F_s * exp(-abs(v2_real) / v_s)); %
friction force [N]
% *****
% friction force cylinder 3
% *****
c3.F_f = k_v * x(14) + sign(x(14)) * (F_c + F_s * exp(-abs(x(14)) / v_s)); %
friction force [N]
% *****

% *****
% spring force cylinder 1
% *****
if x1_real > (c1.l_c / 2) - c1.l_k - (c1.l_p / 2);
c1.F_k = k * ((c1.l_c / 2) - x1_real - (c1.l_p / 2) - c1.l_k);
elseif x1_real < -(c1.l_c / 2) + c1.l_k + (c1.l_p / 2);
c1.F_k = k * (-c1.l_c / 2 - x1_real + c1.l_p / 2 + c1.l_k);
else
c1.F_k = 0;
end
% *****
% spring force cylinder 2
% *****
if x2_real > (c2.l_c / 2) - c2.l_k - (c2.l_p / 2);
c2.F_k = k * ((c2.l_c / 2) - x2_real - (c2.l_p / 2) - c2.l_k);
elseif x2_real < -(c2.l_c / 2) + c2.l_k + (c2.l_p / 2);
c2.F_k = k * (-c2.l_c / 2 - x2_real + c2.l_p / 2 + c2.l_k);
else

```

```

    c2.F_k = 0;
end
% *****
% spring force cylinder 3
% *****
if x(13) > (c3.l_c / 2) - c3.l_k - (c3.l_p / 2);
    c3.F_k = k * ((c3.l_c / 2) - x(13) - (c3.l_p / 2) - c3.l_k);
elseif x(13) < -(c3.l_c / 2) + c3.l_k + (c3.l_p / 2);
    c3.F_k = k * (-c3.l_c / 2 - x(13) + c3.l_p / 2 + c3.l_k);
else
    c3.F_k = 0;
end
% *****

% resulting cylinder forces acting on crane
% *****
f1 = x(3) * c1.A_1 - x(4) * c1.A_2 + c1.F_k - c1.F_f; % (83)
f2 = x(9) * c2.A_1 - x(10) * c2.A_2 + c2.F_k - c2.F_f; % (83)
f3 = x(15) * c3.A_1 - x(16) * c3.A_2 + c3.F_k - c3.F_f; % (83)
% *****

% Lagrange formulation
% *****
M_real = M_function(x(1),x(7),x(13),f1,f2,f3);
h_real = h_function(x(1),x(2),x(7),x(8),x(13),x(14),f1,f2,f3);
q_pp = M_real\h_real; % (62)
% *****

% derivative of the state vector
% *****
dxdt = [x(2) % (63) d/alpha
        q_pp(1) % (63) d/alpha_dot
        c1.E_1 / c1.V_1 * (-c1.A_1 * v1_real + c1.Q_1 - c1.Q_int) % (105) d/p1_1
        c1.E_2 / c1.V_2 * (c1.A_2 * v1_real - c1.Q_2 + c1.Q_int - c1.Q_ext) % (106)
        d/p2_1
        x(6) % (82) d/xs_1
        power(w_n,2) * c1.i - 2 * B * w_n * x(6) - power(w_n,2) * x(5) % (82)
        /d_xs_dot_1
        x(8) % (3) d/beta
        q_pp(2) % (3) d/beta_dot
        c2.E_1 / c2.V_1 * (-c2.A_1 * v2_real + c2.Q_1 - c2.Q_int) % (105) d/p1_2
        c2.E_2 / c2.V_2 * (c2.A_2 * v2_real - c2.Q_2 + c2.Q_int - c2.Q_ext) % (106)
        d/p2_2
        x(12) % (82) d/xs_2
        power(w_n,2) * c2.i - 2 * B * w_n * x(12) - power(w_n,2) * x(11) % (82)
        d/xs_dot_2
        x(14) % (3) d/x3
        q_pp(3) % (3) d/x3_dot
        c3.E_1 / c3.V_1 * (-c3.A_1 * x(14) + c3.Q_1 - c3.Q_int) % (105) d/p1_3
        c3.E_2 / c3.V_2 * (c3.A_2 * x(14) - c3.Q_2 + c3.Q_int - c3.Q_ext) % (106)
        d/p2_3
        x(18) % (82) d/xs_3
        power(w_n,2) * c3.i - 2 * B * w_n * x(18) - power(w_n,2) * x(17)]; % (82)
d/xs_dot_3
% *****

end

% *****
% -----END OF ODE-----
% *****

```

7.3 MATLAB-code 'DIMENSION'

This section represents the dimension of the elements that are part of the laboratory crane at Växjö University, including the beam-linkage and the three double-acting cylinders. The values have been derived from the *SolidWorks* model provided by Rottne Industri AB.

```

function struct = parameter

% Definition of the crane's dimension
% l0 = tripod
% l1 = link 1
% l1 = link 2
% l1 = link 3
% l1 = link 4
% c1 = torque link (closed-loop)
% c1 = cylinder 1
% c2 = cylinder 2
% c3 = cylinder 3

% tripod
% *****
l0.p1 = [0;0;0]; % origin [m] (initial frame)
l0.p2 = [0;0;-1.21]; % floor [m]
% *****

% link 1 (rotary)
% *****
l1.p1 = [0;0;0]; % origin [m] (initial frame)
l1.p2 = [0;0;0.73]; % joint link 2 [m]
l1.p3 = [0.115;0;0.033]; % end cylinder 1 [m]
l1.cg = [0;0;0.73/2]; % center of gravity [m]
l1.m = 50; % mass [kg]
l1.I = [0 0 0;
        0 0 0;
        0 0 0]; % inertia tensor [kg m4]
% *****

% link 2 (boom)
% *****
l2.p1 = [0;0;0]; % joint link 1 [m]
l2.p2 = [0.199;0;-0.061]; % start cylinder 1 [m]
l2.p3 = [1.519;0;0.214]; % start cylinder 2 [m]
l2.p4 = [2.231;0;0.109]; % closed loop [m]
l2.p5 = [2.309;0;0.081]; % joint link 3 [m]
l2.cg = [1.085;0;0.082]; % center of gravity [m]
l2.m = 68.2; % mass [kg]
l2.I = [0.724 0 6.793;
        0 118.644 0;
        6.793 0 118.1]; % inertia tensor [kg m4]
l2.p4_p5 = l2.p5 - l2.p4; % vector between closed loop and joint link 3 [m]
l2.phi = atan(l2.p4_p5(3) / l2.p4_p5(1)); % angle between vector p4/p5 and x-axis(K2)
[rad] !negative!
% *****

% link 3 (jib)
% *****
l3.p1 = [0;0;0]; % joint link 2 [m]
l3.p2 = [-0.035;0;0.094]; % closed loop [m]
l3.p3 = [0.255;0;0.207]; % start cylinder 3 [m]
l3.p4 = [0.98;0;0]; % x-end of link 3 [m]
l3.cg = [0.403;0;0.097]; % center of gravity [m]
l3.m = 27.54; % mass [kg]
l3.I = [0.367 0 1.124;
        0 7.9 0;
        1.124 0 7.638]; % inertia tensor [kg m4]
l3.phi = atan(l3.p2(1) / l3.p2(3)); % angle between x-axis(K3) and l3_p2 [rad]
!negative!
% *****

% link 4 (extension)
% *****
l4.p1 = [1.136;0;-0.051]; % crane tip [m]
l4.p2 = [1.058;0;0.107]; % end cylinder 3 [m]
l4.cg = [0.678;0;0.004]; % center of gravity [m]
l4.m = 10.11; % mass [kg]
l4.I = [0.019 0 0.044

```

```

0      5.942 0
0.044 0      5.935]; % interia tensor [kg m4]
% *****

% torque links in K2
% *****
cl.r1 = [0.182;0;0]; % vector torque link 1 [m]
cl.r2 = [0.194;0;0]; % vector torque link 2 [m]
% *****

% specification of cylinder 1
% *****
cl.o_s = 0.05; % offset start [m]
cl.o_e = 0.01; % offset end [m]
cl.l_c = 0.43; % length cylinder [m]
cl.l_p = 0.1; % length piston [m]
cl.l_r = 0.31; % length rod [m]
cl.l_0 = 0.02; % length dead zone [m]
cl.l_cw = 0.01; % thickness of cylinder body [m]
cl.d_c = 0.1; % diameter cylinder [m]
cl.d_r = 0.04; % diameter rod [m]
cl.d_0 = 0.01; % diameter dead zone [m]
cl.r_c = 0.0001; % leakage radius [m]
cl.e = 0; % initial control error (deviation of norm)
cl.e_i = 0; % initial integral error at t
cl.e_1 = 0; % initial integral error at t_-1
cl.e_2 = 0; % initial integral error at t_-2
cl.u = 0; % initial control input
% *****

% specification of cylinder 2
% *****
c2.o_s = 0.035; % offset start [m]
c2.o_e = 0.095; % offset end [m]
c2.l_c = 0.445; % length cylinder body [m]
c2.l_p = 0.1; % length piston [m]
c2.l_r = 0.31; % length rod [m]
c2.l_cw = 0.01; % thickness of cylinder [m]
c2.d_c = 0.09; % diameter cylinder [m]
c2.d_r = 0.045; % diameter rod [m]
c2.d_0 = 0.01; % diameter dead zone [m]
c2.r_c = 0.0001; % leakage radius [m]
c2.e = 0; % initial control error (deviation of norm)
c2.e_i = 0; % initial integral error at t
c2.e_1 = 0; % initial integral error at t_-1
c2.e_2 = 0; % initial integral error at t_-2
c2.u = 0; % initial control input
% *****

% specification of cylinder 3
% *****
c3.o_s = 0.04; % offset start [m]
c3.o_e = 0.04; % offset end [m]
c3.l_c = 0.71; % length cylinder [m]
c3.l_p = 0.08; % length piston [m]
c3.l_r = 0.71; % length rod [m]
c3.l_cw = 0.01; % thickness of cylinder body [m]
c3.d_c = 0.05; % diameter cylinder [m]
c3.d_r = 0.03; % diameter rod [m]
c3.d_0 = 0.01; % diameter dead zone [m]
c3.r_c = 0.0001; % leakage radius [m]
c3.e = 0; % initial error (deviation of norm)
c3.e_i = 0; % initial integral error at t
c3.e_1 = 0; % initial integral error at t_-1
c3.e_2 = 0; % initial integral error at t_-2
c3.u = 0; % initial control input
% *****

struct = [{10 11 12 13 14 c1 c1 c2 c3}];

end

```


7.4 MATLAB-code 'PLOT_CHARTS'

This code calls all the plot functions beginning with six charts of the generalized coordinates $(\alpha \ \beta \ x_3)^T$, its derivatives $(\omega_\alpha \ \omega_\beta \ v_3)^T$, cylinder pressures p_1 and p_2 and the spool stroke x_p along with its velocity v_p . At the 3rd cylinder, x_p and v_p are obviously the same as the generalized coordinates x_3 and v_3 respectively. Finally, at the end of the plot call, the animation of motion of the crane will be simulated (

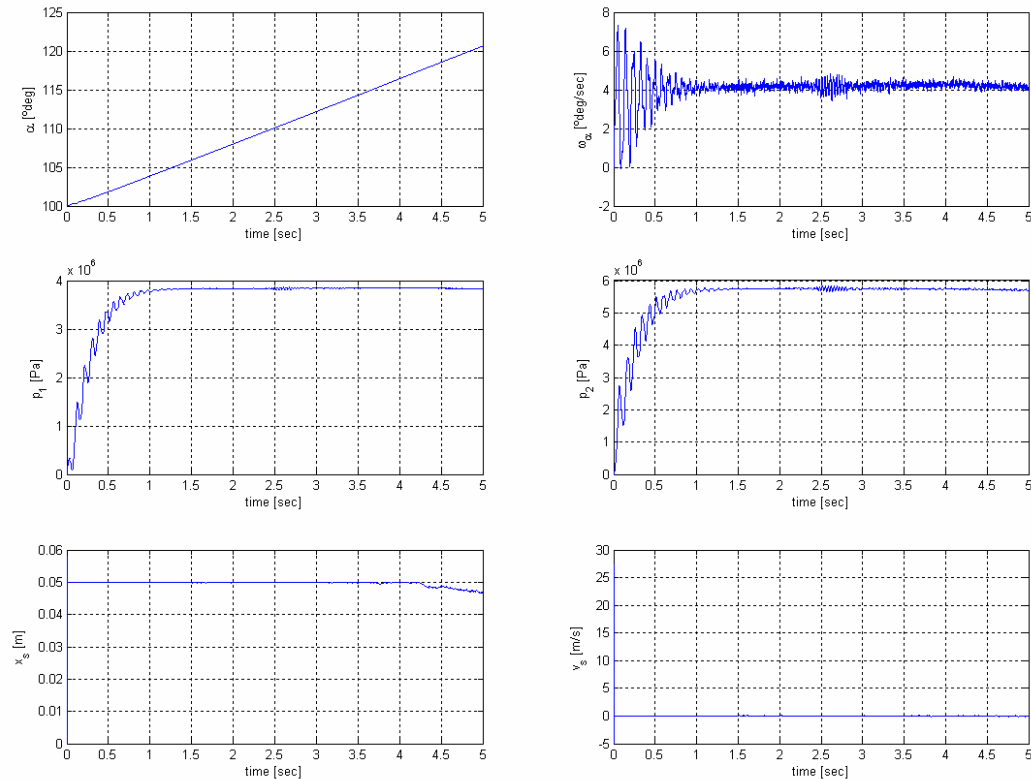


Figure 86: Characteristic charts of cylinder 1

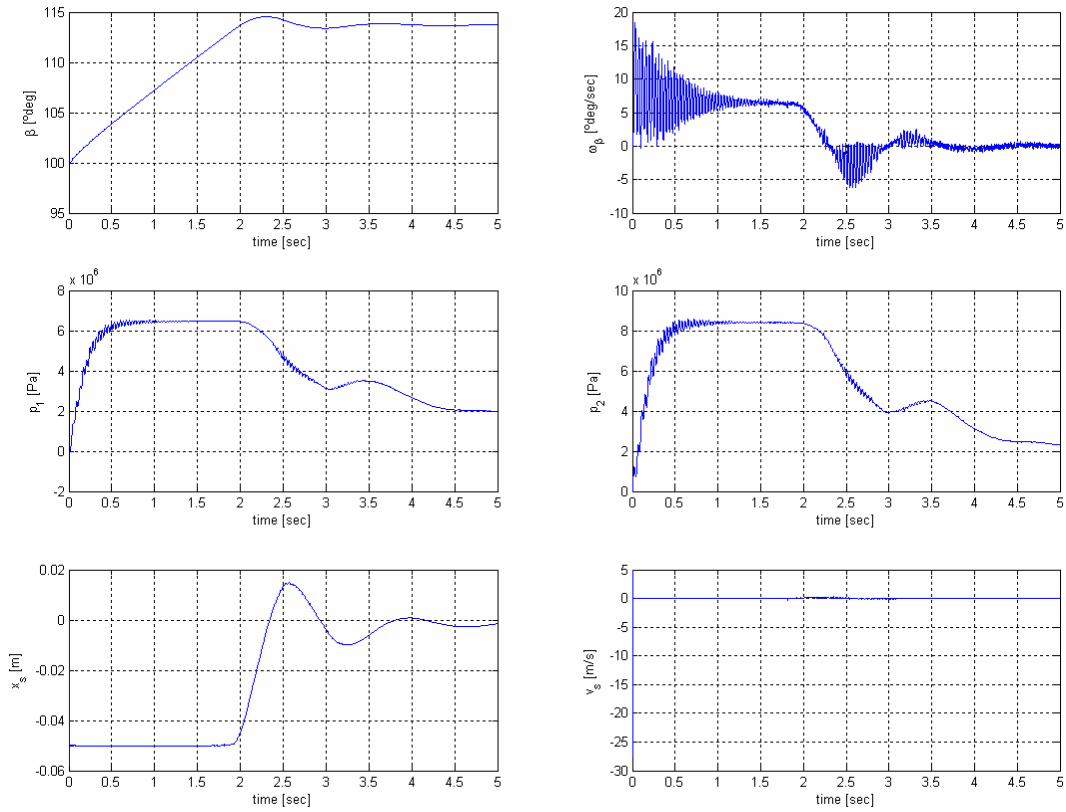


Figure 87: Characteristic charts of cylinder 2

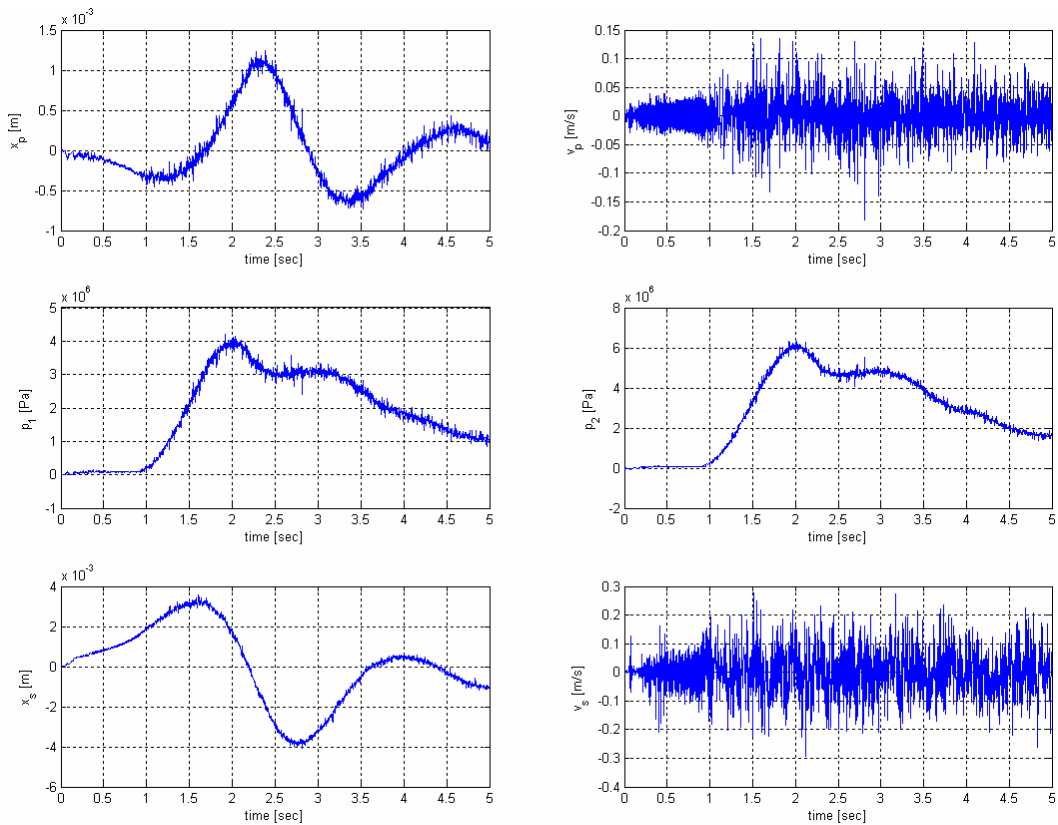


Figure 88: Characteristic charts of cylinder 3

In the second section the call command for the crane animation is listed. The entire crane is drawn by line-representation of all crane elements. Finally the vector of generalized coordinates is used to determine the position and direction of all elements for sequential processing of the animation (see Figure 89)

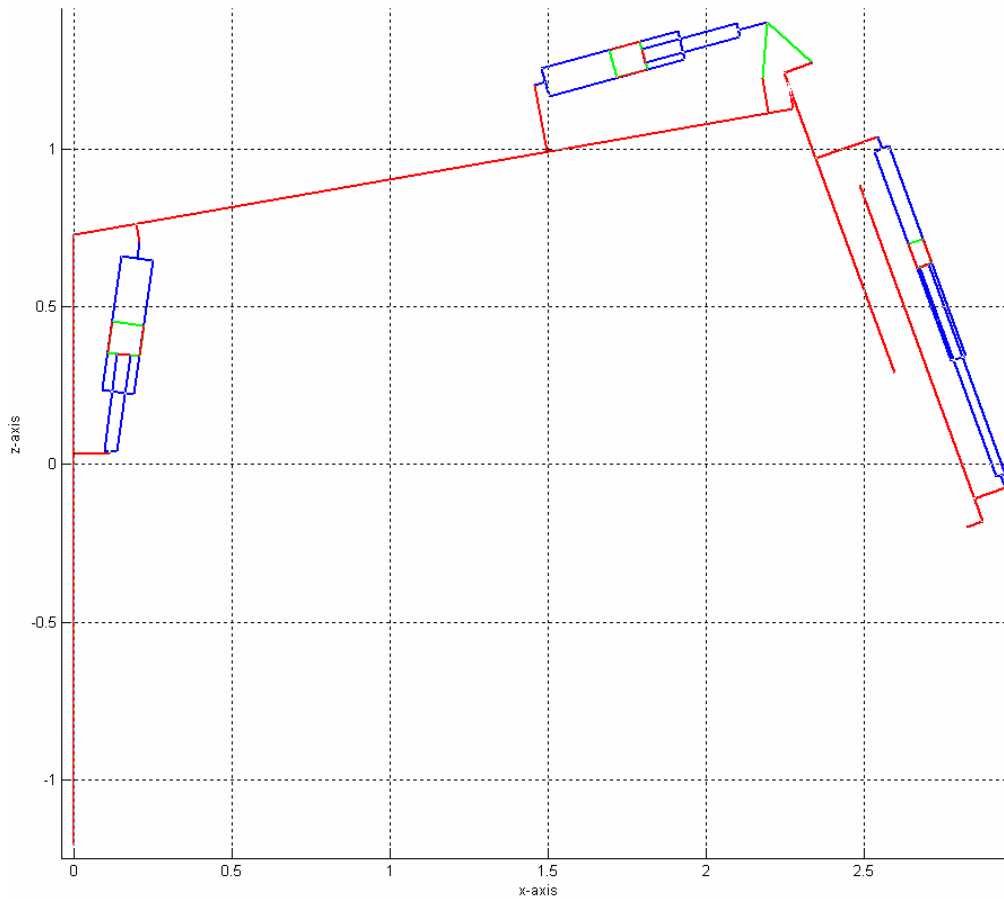


Figure 89: Animation chart

```
function PLOT_CHARTS(t,x,c1,c2,c3,c1,l0,l1,l2,l3,l4,t_step,t_end)

% cylinder 1
% *****
figure;

% chart 1 - alpha
subplot(3,2,1);
plot(t,x(:,1)*180/pi);
xlabel('time [sec]')
ylabel('\alpha [°deg]')
grid on

% chart 2 - w_alpha
subplot(3,2,2);
plot(t,x(:,2)*180/pi);
xlabel('time [sec]')
ylabel('\omega_\alpha [°deg/sec]')
grid on

% chart 3 - pressure 1
subplot(3,2,3);
```

```

plot(t,x(:,3));
xlabel('time [sec]')
ylabel('p_1 [Pa]')
grid on

% chart 4 - pressure 2
subplot(3,2,4);
plot(t,x(:,4));
xlabel('time [sec]')
ylabel('p_2 [Pa]')
grid on

% chart 5 - spool stroke
subplot(3,2,5);
plot(t,x(:,5));
xlabel('time [sec]')
ylabel('x_s [m]')
grid on

% chart 6 - spool velocity
subplot(3,2,6);
plot(t,x(:,6));
xlabel('time [sec]')
ylabel('v_s [m/s]')
grid on

% cylinder 2
% *****
figure

% chart 1 - beta
subplot(3,2,1);
plot(t,x(:,7)*180/pi);
xlabel('time [sec]')
ylabel('\beta [°deg]')
grid on

% chart 2 - beta_p
subplot(3,2,2);
plot(t,x(:,8)*180/pi);
xlabel('time [sec]')
ylabel('\omega_\beta [°deg/sec]')
grid on

% chart 3 - pressure 1
subplot(3,2,3);
plot(t,x(:,9));
xlabel('time [sec]')
ylabel('p_1 [Pa]')
grid on

% chart 4 - pressure 2
subplot(3,2,4);
plot(t,x(:,10));
xlabel('time [sec]')
ylabel('p_2 [Pa]')
grid on

% chart 5 - spool stroke
subplot(3,2,5);
plot(t,x(:,11));
xlabel('time [sec]')
ylabel('x_s [m]')
grid on

% chart 6 - spool velocity
subplot(3,2,6);
plot(t,x(:,12));
xlabel('time [sec]')
ylabel('v_s [m/s]')
grid on

% cylinder 3
% *****

```

```

figure

% chart 1 - cylinder stroke
subplot(3,2,1);
plot(t,x(:,13));
xlabel('time [sec]')
ylabel('x_p [m]')
grid on

% chart 2 - cylinder velocity
subplot(3,2,2);
plot(t,x(:,14));
xlabel('time [sec]')
ylabel('v_p [m/s]')
grid on

% chart 3 - pressure 1
subplot(3,2,3);
plot(t,x(:,15));
xlabel('time [sec]')
ylabel('p_1 [Pa]')
grid on

% chart 4 - pressure 2
subplot(3,2,4);
plot(t,x(:,16));
xlabel('time [sec]')
ylabel('p_2 [Pa]')
grid on

% chart 5 - spool stroke
subplot(3,2,5);
plot(t,x(:,17));
xlabel('time [sec]')
ylabel('x_s [m]')
grid on

% chart 6 - spool velocity
subplot(3,2,6);
plot(t,x(:,18));
xlabel('time [sec]')
ylabel('v_s [m/s]')
grid on

% *****

% animation
% *****
figure

% cylinder 1 specs
cylinder1 = drahtmodell_rechteck_xz(c1.l_c/2,c1.d_c/2);
piston1 = drahtmodell_rechteck_xz(c1.l_p/2,c1.d_c/2);
rod1 = drahtmodell_rechteck_xz(c1.l_r/2,c1.d_r/2);

% cylinder 2 specs
cylinder2 = drahtmodell_rechteck_xz(c2.l_c/2,c2.d_c/2);
piston2 = drahtmodell_rechteck_xz(c2.l_p/2,c2.d_c/2);
rod2 = drahtmodell_rechteck_xz(c2.l_r/2,c2.d_r/2);

% cylinder 3 specs
cylinder3 = drahtmodell_rechteck_xz(c3.l_c/2,c3.d_c/2);
piston3 = drahtmodell_rechteck_xz(c3.l_p/2,c3.d_c/2);
rod3 = drahtmodell_rechteck_xz(c3.l_r/2,c3.d_r/2);

% cylinder mount
c1_mount_s = {[0 0 0
               c1.o_s 0 0]};

c1_mount_e = {[0 0 0
               -c1.o_e 0 0]};

c2_mount_s = {[0 0 0
               c2.o_s 0 0]};

```

```

c2_mount_e = {[0 0 0
               -c2.o_e 0 0]};

c3_mount_s = {[0 0 0
               c3.o_s 0 0]};

c3_mount_e = {[0 0 0
               c3.o_e 0 0]};

% crane specs
link_0 = {[10.p1';
           10.p2']};

link_1 = {[11.p1';
           11.p2'];
           [0 0 11.p3(3);
           11.p3']};

link_2 = {[12.p1';
           12.p5(1) 0 0];
           [12.p2';
           12.p2(1) 0 0];
           [12.p3';
           12.p3(1) 0 0];
           [12.p4';
           12.p4(1) 0 0];
           [12.p5';
           12.p5(1) 0 0]};

link_3 = {[13.p4';
           13.p2(1) 0 0];
           [13.p2';
           13.p2(1) 0 0];
           [13.p3';
           13.p3(1) 0 0]};

link_4 = {[0 0 0;
           14.p1(1) 0 0;
           14.p1'];
           [14.p2';
           14.p2(1) 0 0]};

c1_1 = {[0 0 0;
          c1.r1']};

c1_2 = {[0 0 0;
          c1.r2']};

for i=1:length(t)

l_x1 = c1.fhandle_x(x(i,1));
l_x2 = c2.fhandle_x(x(i,1),x(i,7));

A_IK1 = eye(3);
A_IK2 = A_IK1 * A_y(pi / 2 - x(i,1));
A_IK3 = A_IK1 * A_y(pi / 2 - x(i,1)) * A_y(pi - x(i,7));

A_Ic1 = A_y(pi / 2 + c1.fhandle_phi(x(i,1))); % angle cylinder 1 related to inertia
frame
A_Ic2 = A_IK2 * A_y(-c2.fhandle_phi(x(i,1),x(i,7))); % angle cylinder 2 / link 2

A_It1 = A_IK2 * A_y(- c1.fhandle_eps1(x(i,1),x(i,7))); % angle torque 1 related to
inertia frame
A_It2 = A_IK2 * A_y(- c1.fhandle_eps1(x(i,1),x(i,7)) - c1.fhandle_teta2(x(i,1),x(i,7))
+ pi); % angle torque 2 related to inertia frame

c1.center_c = A_IK1 * l1.p2 + A_IK2 * l2.p2 + A_Ic1 * [c1.o_s + c1.l_c / 2;0;0];
c1.center_p = c1.center_c + A_Ic1 * [l_x1;0;0];
c1.center_r = c1.center_p + A_Ic1 * [(c1.l_p + c1.l_r) / 2;0;0];

c2.center_c = A_IK1 * l1.p2 + A_IK2 * l2.p3 + A_Ic2 * [c2.o_s + c2.l_c / 2;0;0];
c2.center_p = c2.center_c + A_Ic2 * [l_x2;0;0];
c2.center_r = c2.center_p + A_Ic2 * [(c2.l_p + c2.l_r) / 2;0;0];

```

```

c3.center_c = A_IK1 * l1.p2 + A_IK2 * l2.p5 + A_IK3 * l3.p3 + A_IK3 * [c3.o_s + c3.l_c
/ 2;0;0];
c3.center_p = c3.center_c + A_IK3 * [x(i,l3);0;0];
c3.center_r = c3.center_p + A_IK3 * [(c3.l_p + c3.l_r) / 2;0;0];

x_c_1(i,:) = [c1.center_c' A_Ic1(1,:) A_Ic1(2,:) A_Ic1(3,:)];
x_piston_1(i,:) = [c1.center_p' A_Ic1(1,:) A_Ic1(2,:) A_Ic1(3,:)];
x_rod_1(i,:) = [c1.center_r' A_Ic1(1,:) A_Ic1(2,:) A_Ic1(3,:)];

x_c_2(i,:) = [c2.center_c' A_Ic2(1,:) A_Ic2(2,:) A_Ic2(3,:)];
x_piston_2(i,:) = [c2.center_p' A_Ic2(1,:) A_Ic2(2,:) A_Ic2(3,:)];
x_rod_2(i,:) = [c2.center_r' A_Ic2(1,:) A_Ic2(2,:) A_Ic2(3,:)];

x_c_3(i,:) = [c3.center_c' A_IK3(1,:) A_IK3(2,:) A_IK3(3,:)];
x_piston_3(i,:) = [c3.center_p' A_IK3(1,:) A_IK3(2,:) A_IK3(3,:)];
x_rod_3(i,:) = [c3.center_r' A_IK3(1,:) A_IK3(2,:) A_IK3(3,:)];

x_00(i,:) = [0 0 0 1 0 0 0 1 0 0 0 1];
x_01(i,:) = [x_00(i,1:3) + (l1.p1)' A_IK1(1,:) A_IK1(2,:) A_IK1(3,:)];
x_02(i,:) = [x_01(i,1:3) + (A_IK1 * l1.p2)' A_IK2(1,:) A_IK2(2,:) A_IK2(3,:)];
x_03(i,:) = [x_02(i,1:3) + (A_IK2 * l2.p5)' A_IK3(1,:) A_IK3(2,:) A_IK3(3,:)];
x_04(i,:) = [x_rod_3(i,1:3) + (A_IK3 * ((c3.l_r / 2 + c3.o_e;0;0) - l4.p2))'
A_IK3(1,:) A_IK3(2,:) A_IK3(3,:)];
x_cl_1(i,:) = [x_02(i,1:3) + (A_IK2 * l2.p4)' A_It1(1,:) A_It1(2,:) A_It1(3,:)];
x_cl_2(i,:) = [x_cl_1(i,1:3) + (A_It1 * c1.r1)' A_It2(1,:) A_It2(2,:) A_It2(3,:)];

x_c_1_mount_s(i,:) = [x_02(i,1:3) + (A_IK2 * l2.p2)' A_Ic1(1,:) A_Ic1(2,:)
A_Ic1(3,:)];
x_c_1_mount_e(i,:) = [x_01(i,1:3) + (A_IK1 * l1.p3)' A_Ic1(1,:) A_Ic1(2,:)
A_Ic1(3,:)];
x_c_2_mount_s(i,:) = [x_02(i,1:3) + (A_IK2 * l2.p3)' A_Ic2(1,:) A_Ic2(2,:)
A_Ic2(3,:)];
x_c_2_mount_e(i,:) = [x_cl_2(i,1:3) A_Ic2(1,:) A_Ic2(2,:) A_Ic2(3,:)];
x_c_3_mount_s(i,:) = [x_03(i,1:3) + (A_IK3 * l3.p3)' A_IK3(1,:) A_IK3(2,:)
A_IK3(3,:)];
x_c_3_mount_e(i,:) = [x_rod_3(i,1:3) + (A_IK3 * [c3.l_r / 2;0;0])' A_IK3(1,:)
A_IK3(2,:) A_IK3(3,:)];

end

CRANE_ANIMATION({x_00 link_0 4;...
x_01 link_1 4;...
x_02 link_2 4;...
x_03 link_3 4;...
x_04 link_4 4;...
x_cl_1 cl_1 5;...
x_cl_2 cl_2 5;...
x_c_1 cylinder1 6;...
x_piston_1 piston1 5;...
x_rod_1 rod1 6;...
x_c_2 cylinder2 6;...
x_piston_2 piston2 5;...
x_rod_2 rod2 6;...
x_c_3 cylinder3 6;...
x_piston_3 piston3 5;...
x_rod_3 rod3 6;...
x_c_1_mount_s cl_mount_s 6;...
x_c_1_mount_e cl_mount_e 6;...
x_c_2_mount_s c2_mount_s 6;...
x_c_2_mount_e c2_mount_e 6;...
x_c_3_mount_s c3_mount_s 6;...
x_c_3_mount_e c3_mount_e 6},t_step,t_end,[0,0]);
% *****

End

```

8 Conclusions and outlook

The major goal of this thesis work was to develop a model of a hydraulic laboratory crane including friction estimation of the hydraulic cylinders and a new approach to a more sophisticated control of the crane's end-effector.

As a start to the crane model we initially derived the equations of motion for the mechanical model in the traditional Euler-Lagrange fashion. We tried to keep the mathematical expressions rather simple by making some smaller assumptions. Since the crane is a complex linkage and consequently its dynamic behaviour is pretty complicated to describe, the assumptions made us handle the mathematics in a convenient straightforward manner. We then modelled the hydraulic flow through the valves into each of the three actuators by using an ordinary equation of motion of 2nd order for the spool movement and a rather detailed derivation of the hydraulic flow to determine the derivative of the chamber pressures of each cylinder. Here we distinguished between laminar and turbulent flow, the Bernoulli flow phenomenon and the regenerative valve in use with the cylinder for the telescopic extension. Finally we have determined eighteen state variables including three joint angles (the generalized coordinates), its derivatives and for each cylinder two chamber pressures and the valve spool positions with their derivatives. The complete model was then transcribed in *MATLAB* where we encountered the problem of a highly complicated inverse kinematics. This was caused mainly by the complex relationship of the torque link as it builds a closed loop chain that was extremely hard to handle with the geometric approach in chapter 3. However, the movement of the crane could be visualized in terms of an animation function in *MATLAB* and although the sequences proceeded rather slowly, the crane seemed to move as expected. Future works should focus on facilitating the torque link relation in order to keep the equations as simple as possible and to run the simulation even faster.

Friction evaluation was the second main goal of this work. We put up a cylinder test rig in the laboratory hall that allowed for friction experiments of the hydraulic cylinder of the telescopic beam. First we ran experiments while keeping the piston velocity constant. We obtained velocity-friction maps tracking the friction force for several velocities, both positive and negative. These maps represented the common static friction behaviour of the cylinders and corresponded quite well with the theoretical friction model. We noticed that the cylinder from Rottne was characterised by a higher friction force than it was shown at the Kalmar cylinder. This probably arose from the fact that the Rottne cylinder was used before in real-world applications and consequently abrasion led to smaller wear particles that caused high friction. To examine the dynamic friction behaviour of the cylinders we applied the LuGre model which deals with the bristle interpretation of friction. For this purpose we ran experiments with a ramp input to investigate the spring-like behaviour of the bristles and a step input for the damping characteristics. We simplified the LuGre model by making plausible assumptions which yielded in the dynamic parameters representing the friction variables in the LuGre model. When running the experiments we were also able to do variations in pressure and loads but the results showed us that neither less system pressure nor different mass of the loads results in a significant change of friction force.

The last goal of this work was to establish a more sophisticated control algorithm in order to operate the crane in a more convenient manner. The idea was to use the joysticks not to control the actuators in a traditional way but to apply the inverse kinematics to control the crane tip in the planar $x-z$ frame. This was done by feeding the joystick input signal to a dSpace box which then was calculated into a desired velocity for horizontal and vertical movement of the crane-tip. Depending on the sampling rate, the new coordinates in terms of the velocity were determined and by means of a traditional PID control, the required input signal could be fed to the valves. This control worked quite well in the animation mode but still there was some smaller deviation of the desired trajectory. A higher accuracy could possibly be reached by using smaller sampling intervals but the major drawback here is the rising processing time for the PID control.

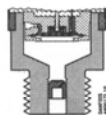
9 Appendix

9.1 Data sheets



Data Sheet		Pressure transmitter for heavy-duty applications Type MBS 2050	
Technical data			
<i>Performance (EN 60770)</i>			
Accuracy (incl. non-linearity, hysteresis and repeatability)		±0.3% FS (typ.) ±1% FS (max.)	
Non-linearity BFSL (conformity)		≤ ±0.2% FS	
Hysteresis and repeatability		≤ ±0.1% FS	
Thermal zero point shift		≤ ±0.1% FS/10K (typ.) ≤ ±0.2% FS/10K (max.)	
Thermal sensitivity (span) shift		≤ ±0.1% FS/10K (typ.) ≤ ±0.2% FS/10K (max.)	
Response time	Liquids with viscosity < 100 cSt	< 4 ms	
	Air and gases	< 35 ms	
Overload pressure (Static)		6 × FS (max. 1500 bar)	
Burst pressure		> 6 × FS (max. 2000 bar)	
Durability, P: 10-90% FS		> 10×10 ⁶ cycles	
<i>Electrical specifications</i>			
Nom. output signal		10 - 90% of V _{supply}	
Supply voltage V _{supply} (polarity protected)		4.75 to 8 V d.c. 5 V d.c. (nom.)	
Power consumption		<5mA at 5 V d.c	
Output impedance		<25 Ω	
Load resistance RL		RL > 5 kΩ at 5 V d.c.	
<i>Environmental conditions</i>			
Medium temperature range		-40 → +85°C	
Ambient temperature range (depending on electrical connection)		see page 4	
Compensated temperature range		0 → +80°C	
Transport temperature range		-50 → +85°C	
EMC - Emission		EN 61000-6-3	
EMC Immunity		EN 61000-6-2	
Insulation resistance		> 100 MΩ at 100 V	
Mains frequency test		SEN 361503	
Vibration stability	Sinusoidal	15.9 mm-pp, 5 Hz-25 Hz 20 g, 25 Hz-2 kHz	IEC 60068-2-6
	Random	7.5 g _{rms} , 5Hz-1kHz	IEC 60068-2-34, IEC 60068-2-36
Shock resistance	Shock	500 g / 1 ms	IEC 60068 - 2 - 27
	Free fall		IEC 60068 - 2 - 32
Enclosure (depending on electrical connection)		see page 4	
<i>Mechanical characteristics</i>			
Materials	Wetted parts	EN 10088-1; 1.4404 (AISI 316 L)	
	Enclosure	EN 10088-1; 1.4404 (AISI 316 L)	
	Electrical connections	see page 4	
Weight (depending on pressure connection and electrical connection)		0.2 - 0.3 kg	

Application and media conditions



Application

Cavitation, liquid hammer and pressure peaks may occur in liquid filled hydraulic systems with changes in flow velocity, e.g. fast closing of a valve or pump starts and stops. The problem may occur on the inlet and outlet side, even at rather low operating pressures.

Media condition

Clogging of the nozzle may occur in liquids containing particles. Mounting the transmitter in an upright position minimizes the risk of clogging, because the flow in the nozzle is restricted to the start-up period when the dead volume behind the nozzle fills, and furthermore because the nozzle orifice is relatively big (0.3 mm). The media viscosity has only little effect on the response time. Even at a viscosities up to 100 cSt, the response time will not exceed 4 ms.

IC.PD.P20.L2.02/520B2512

Figure 90: Data sheet of Danfoss pressure sensor MBS 2050

Hottinger Baldwin Messtechnik GmbHIm Tiefen See 45
D-64293 DarmstadtZertifiziert nach ISO 9001 und ISO 14001
ISO 9001 and ISO 14001 certified / Certification selon ISO 9001 et ISO 14001Akkreditierungen gemäß ISO 17025
Accreditations per ISO 17025 / Accréditations selon ISO 17025**Prüfprotokoll**

test certificate / protocole d'essai

Typ: type / type	U9B	Auftrag: order no / commission	801075646
Nennmessbereich: range / portée	50 kN	Prüfer: examiner / contrôleur	Mergel
IdentNr: serial no / N°-ident	100810290	Datum: test date / date d'essai	10.08.2006

Prüfergebnisse:

test results / résultats d'essai

Eingangsgröße des Messbereichs [%] input quantity / échelle d'essai	Ausgangsgröße [mV/V] output quantity / résultats
	Zug tension / traction
0	0.0000
50	-0.4990
100	-0.9994
50	-0.4993
0	-0.0001

Aus den Prüfergebnissen berechnete messtechnische Kenngrößen:Metrological characteristic quantities computed from the test results:
Grandeurs caractéristiques de mesure calculées à partir des résultats d'essai :

Kennwert C [mV/V] sensitivity / sensibilité	-0.9994
Linearitätsabweichung [%vC] linearity deviation / linearité (Abweichung von der bestpassenden Geraden durch das Nullsignal) (deviation from bestfit through zero / écart par rapport à la meilleure droite passant par le zéro)	-0.049
Relative Umkehrspanne 0,5 F _{nom} [%vI] relative hysteresis / hystérésis relatif	0.072

Alle aus den Messergebnissen ermittelten Kenngrößen entsprechen den Spezifikationen gemäß Datenblatt.
All characteristic quantities determined from the measurement results correspond to the specifications per datasheet.
Toutes les grandeurs caractéristiques déterminées à partir des résultats de mesure correspondent aux spécifications selon les caractéristiques techniques.**Allgemeine Zusatzinformationen:**

general information / informations complémentaires

Alle weiteren messtechnischen Eigenschaften des Aufnehmers sind durch Typprüfungen und laufende Produktaudits des Qualitätswesens abgesichert.
All other metrological characteristics of the transducer are verified by type testing and regular product audits of the quality department.
Toutes les autres caractéristiques techniques du capteur sont garanties par le Service Qualité, au moyen d'essais et d'audits suivis sur le produit.

Nr. 0229.003

V3.0/WS-T/02.06

Seite / Page 1 (1)

Figure 91: Data sheet of HBM load sensor U9B (50 kN)

Hottinger Baldwin Messtechnik GmbH

Im Tiefen See 45
D-64293 DarmstadtZertifiziert nach ISO 9001 und ISO 14001
ISO 9001 and ISO 14001 certified / Certification selon ISO 9001 et ISO 14001Akreditierungen gemäß ISO 17025
Accreditations per ISO 17025 / Accréditations selon ISO 17025

Prüfprotokoll

test certificate / protocole d'essai

Typ: type / type	U9B	Auftrag: order no / commission	801086901
Nennmessbereich: range / portée	10 kN	Prüfer: examiner / contrôleur	Mergel
IdentNr: serial no / N°-ident	102410066	Datum: test date / date d'essai	02.05.2007

Prüfergebnisse:

test results / résultats d'essai

Eingangsgröße des Messbereichs [%]
input quantity / échelle d'essaiAusgangsgröße [mV/V]
output quantity / résultats

	Zug tension / traction
0	0.0000
50	-0.5011
100	-1.0026
50	-0.5013
0	-0.0001

Aus den Prüfergebnissen berechnete messtechnische Kenngrößen:

Metrological characteristic quantities computed from the test results:
Grandeurs caractéristiques de mesure calculées à partir des résultats d'essai :Kennwert C [mV/V]
sensitivity / sensibilité -1.0026Linearitätsabweichung [%vC]
linearity deviation / linearité -0.012(Abweichung von der bestpassenden Geraden durch das Nullsignal)
(deviation from bestfit through zero / écart par rapport à la meilleure droite passant par le zéro)Relative Umkehrspanne 0,5 Fnom [%vI]
relative hysteresis / hystérésis relatif 0.047

Alle aus den Messergebnissen ermittelten Kenngrößen entsprechen den Spezifikationen gemäß Datenblatt.

All characteristic quantities determined from the measurement results correspond to the specifications per datasheet.
Toutes les grandeurs caractéristiques déterminées à partir des résultats de mesure correspondent aux spécifications selon les caractéristiques techniques.

Allgemeine Zusatzinformationen:

general information / informations complémentaires

Alle weiteren messtechnischen Eigenschaften des Aufnehmers sind durch Typprüfungen und laufende Produktaudits des Qualitätswesens abgesichert.
All other metrological characteristics of the transducer are verified by type testing and regular product audits of the quality department.
Toutes les autres caractéristiques techniques du capteur sont garanties par le Service Qualité, au moyen d'essais et d'audits suivis sur le produit.

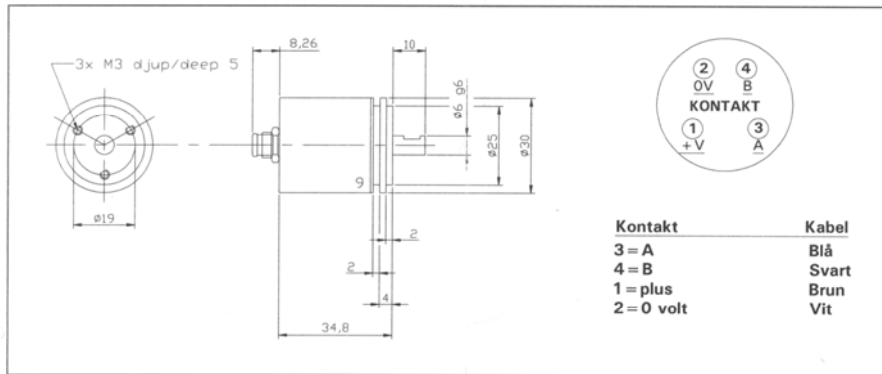
Nr. 0229.003

V3.0/WS-T/02.06

Seite / Page 1 (1)

Figure 92: Data sheet of HBM load sensor U9B (10 kN)

Inkrementell givare modell MA500-6-xxxx-9



Elektrisk specifikation

Matningsspänning	Vcc 7-35V
Strömförbrukning	max 35 mA, utan last
Utgångskrets	Linedriver RS422A kompatibel
Lågnivå utspänning	max <0,5V vid 20 mA last och 20°C
Högnivå utspänning	min >Vcc-1V vid 20 mA last och 20°C
Kortslutningssäker	Ja
Polvändningssäker	Ja
Transientskydd	Ja
Max last	70 mA

Ut signaler

Motors rotation sett från axelsidan	1	
	2	

Signaltoleranser

Delningsfel max	± 50 el°
Kanalseparation	90 ± 25 el°
Max läsfrekvens	100 KHz
Temperaturområde	-40° till + 80°C

Mekanisk specifikation

Hus	Anodiserat aluminium, elektriskt ledande för förhöjt störskydd
Tätning	IP 65dam- och spolsäker
Lager	Permanentsmorda spärkullager
Lagerbelastning vid 1 000 rpm:	
Radiell	20 N
Axiell	15 N ger 50 000 tim livslängd
Max rpm	6 000
Vibration	20g 20-2 000 Hz
Chock	200g vid 11 ms
Vikt	ca: 60 gr. (utan kabel)

Anslutning

9. Axiell 4-polig M8 kontakt för speciell kabel

Funktion

	Kabel 9
1 (A)	Blå
2 (B)	Svart
+ V	Brun
0 V	Vit

Kabel till anslutning 9

M8SR2, Snäpp Rak 2 m
M8SR5, Snäpp Rak 5 m
M8SV2, Snäpp Vinklad 2 m
M8SV5, Snäpp Vinklad 5 m

Beställningskod

Modell	MA500	6	125	9
Axel 6 mm				
Pulstal 1-1250				
Anslutning				

EMETA AB

Skogsvägen 1, 645 34 Strängnäs
Tel. 0152-33 11 90, Fax. 0152-33 11 91
e-mail: info@emeta.se, hemsida: www.emeta.se

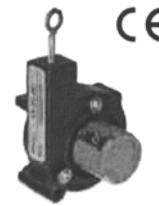
EMETA

Figure 93: Data sheet of EMETA incremental sensor

LX-PA SERIES RATIOMETRIC VOLTAGE OUTPUT

The UniMeasure LX-PA Series linear position transducer with analog output is a low cost, compact alternative for use in light to moderate duty applications in dry environments. The plastic bodied device is ideal for high volume OEM situations where cost is a major consideration and in applications where small size or low weight are of paramount importance.

Model LX-PA is available in eleven different measurement ranges with a maximum range of 50" (1250 mm). The output is voltage from a potentiometric voltage divider circuit. In standard form, the electrical connections are made directly to the contacts on the potentiometer of the unit. Optional electrical cable attached to the potentiometer is available in various lengths. Standard potentiometer value is 1K ohm with optional values of 2K, 5K and 10K ohm available.



SPECIFICATIONS

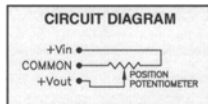
General
 Measurement Ranges..... See Table 1
 Sensing Device Precision Potentiometer
 Resolution Essentially Infinite
 Linearity
 2", 2.8", 3.8" 4.7" ranges..... ±1.0% Full Scale
 10" to 25" ranges ±0.5% Full Scale
 30" to 50" ranges ±0.25% Full Scale
 Repeatability ±0.03% Full Scale
 Construction Thermoplastic Body
 Cable Ø 0.018 (0.46 mm) Jacketed
 Stainless Steel
 Wire Rope Tension..... See Table 1
 Weight 3 oz. (85 gm)
 Connections Solder terminals
 Dimensional Information See Supplemental Data¹
 Life
 Ranges to 4.7" 1,000,000 full stroke cycles
 Ranges 10" to 25" 250,000 full stroke cycles
 Ranges 30" to 50" 125,000 full stroke cycles

Environmental
 Operating Temperature -25°C to 75°C
 Storage Temperature -50°C to 80°C
 Operating Humidity 95 R.H. max. non-condensing
 Vibration 15 G's 0.1 ms max.
 Shock 50 G's 0.1 ms max.
 Ingress Protection NEMA 1, IP-40

Electrical
 Input Impedance 1000 Ω ±15%
 Output Impedance 0 to 1000 Ω
 Excitation Voltage 25 Volts max. AC or DC

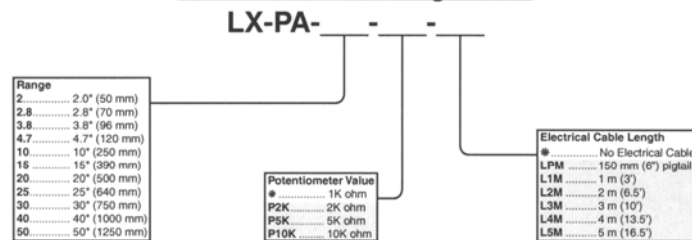
TABLE 1

MODEL	RANGE (Inch) (mm)	NOMINAL OUTPUT (mV/V/in) (mV/V/mm)	NOMINAL WIRE ROPE TENSION (oz) (N)
LX-PA-2	2 50	469 18.5	16 4.4
LX-PA-2.8	2.8 70	341 13.4	14 3.9
LX-PA-3.8	3.8 96	258 10.1	11 3.1
LX-PA-4.7	4.7 120	207 8.1	8 2.2
LX-PA-10	10 250	88 3.5	16 4.4
LX-PA-15	15 380	64 2.5	14 3.9
LX-PA-20	20 500	49 1.9	11 3.1
LX-PA-25	25 625	39 1.5	8 2.2
LX-PA-30	30 750	32 1.3	14 3.9
LX-PA-40	40 1000	24 1.0	11 3.1
LX-PA-50	50 1250	20 0.8	8 2.2



FOOTNOTES TO SPECIFICATIONS
 1. Supplemental Data section located at end of LX Series pages.

Model Number Configuration



NOTE
 1) *—Asterisk items are standard configuration. No option designator is required.
 2) Shaded options available at additional cost.

Example
LX-PA-20-L1M

Figure 94: Data sheet of UniMeasure position sensor LX-PA-50

9.2 CD-Rom

9.2.1 Content

THESIS

- *Thesis_Modelling_Simulation_And_Control_Of_A_Hydraulic_Crane.doc*: Word-document of the thesis work
- *Thesis_Modelling_Simulation_And_Control_Of_A_Hydraulic_Crane.pdf*: PDF-document of the thesis work

MATLAB

- *A_x.m / A_y.m / A_z.m*: Rotational matrix about x-/ y-/ and z-axis
- *ANGLE_LIMIT_ALPHA.m*: Correlation between joint variable alpha and piston stroke of cylinder 1
- *CRANE_ANIMATION.m*: Animation of the crane
- *CRANE_MAIN.m*: Main functionf for crane simulation
- *CYLINDER.m*: Test file for cylinder simulation
- *CYLINDER_SIMULINK.mdl*: Corresponding test model for cylinder simulation
- *DIMENSION.m*: Crane dimensions
- *PLOT_CHARTS.m*: Charts of cylinder sepcification
- *TRANSITION_FLOW.m*: Transition phase of laminar and turbulent pressure
- *WORKING_AREA.m*: Operating range of the crane

CAD

- *38652rev2.sldasm*: Solid Assembly file of the laboratory crane

FRICTION

- *CYLINDER KALMAR: MATLAB-* and *dSPACE-* files of the Kalmar cylinder
- *CYLINDER ROTTNE: MATLAB-* and *dSPACE-* files of the Rottne cylinder

9.2.2 CD-Rom attachment

10 Bibliography

- [1] U. Mettin, P.X. Miranda la Hera. *Modelling and Control Design for a Hydraulic Forestry Crane*. Department of Applied Physics and Electronics, Umeå University, Sweden, 2005.
- [2] M. Sigvardsson, T. Olsson. *Modelling and Simulation of a Hydraulic Crane*. Department of Technology, Högskolan Kalmar, Sweden, 2005.
- [3] B. Šulc, J.A. Jan. Non Linear Modelling and Control of Hydraulic Actuators. *Acta Polytechnica Vol.42 No.3/2002*, pages 41 – 47, Prague, Czech Republic, 2002.
- [4] M.W. Spong, S. Hutchinson, M. Vidyasagar. *Robot Modeling And Control*. John Wiley & Sons, Inc., New Jersey, USA, 2006.
- [5] L. Sciavicco, B. Siciliano. *Modelling and Control of Robot Manipulators*. Springer-Verlag, London, GB, 2005.
- [6] M. Lemmen, M. Bröcker, B. de Jager, H. van Essen. CACSD for hydraulic cylinders. *Proceedings of the 2000 IEEE International Symposium on Computer-Aided Control System Design Anchorage, Alaska, USA, 2000*.
- [7] T. Ekevid, M. Lennels. *Ställdon, mätgivare och deras placering för Tunga fordons laborationskran*, Institutionen för teknik och design, Växjö Universitet, Sweden, 2007.
- [8] J. Oloffson. Konstruktion av analogt gränssnitt. *Arbetsrapport*, Matematiska & Systemtekniska institutionen, Växjö Universitet, Sweden, 2007.
- [9] K. Prorok. *Crane-Tip Control of a Hydraulic Crane: A new Approach*. Department of Applied Physics and Electronics, Umeå University, Sweden, 2003.
- [10] Prof. Dr. P. Wolfsteiner. *Mehrkörpersysteme*. Fakultät 03, Fachhochschule München, Germany, 2003.
- [11] H.J. Bartsch. *Taschenbuch mathematischer Formeln*. Fachbuchverlag Leipzig, Germany, 2004.
- [12] LPA. *Kranstyrning SMST*. Rottne Industri AB, Sweden, 2006.
- [13] <http://www.physik.uni-bielefeld.de/theory/cm/research/projects/friction>
- [14] C. Canudas de Wit, P. Lischinsky. Adaptive friction compensation with partially known dynamic friction model. *International journal of adaptive control and signal processing, Vol.11*, pages 65 – 80, Grenoble, France, 1997.

- [15] <http://www.rottne.com/prod/bilder/stor-smv-rapid.jpg>
- [16] H. Olsson, K.J. Åstrom, C. Canudas de Wit, M. Gräfvvert, P. Lischinsky. Friction Models and Friction Compensation. *European Journal of Control* 1998 (4), pages 176-195, UK, 1998.
- [17] B. Armstrong-Hélouvry, P. Dupont, C. Canudas de Wit. A survey of models, analysis tools and compensation methods for the control of machines with friction. *Automatica* 1994 30(7), pages 1083 – 1138, UK, 1994.



Växjö
universitet

Institutionen för teknik och design

351 95 Växjö

tel 0470-70 80 00, fax 0470-76 85 40

www.vxu.se/td